

ABSTRACT

Title of thesis: EXPERIMENTAL INVESTIGATIONS OF
 THE EFFECTS OF SURFACTANTS ON
 DROPLET PRODUCTION BY BUBBLES
 RISING TO A FREE SURFACE

Karan Parmar, Master of Science, 2013

Thesis directed by: Professor James H Duncan
 Department of Mechanical Engineering

Air bubbles traveling upwards from within a liquid, burst at the free surface and eject droplets into the air. The liquid droplets produced from the bursting of air bubbles at the free surface of the ocean have long been considered as constituting a significant fraction of the marine aerosol production. This process plays an important role in the transfer of mass and energy between the ocean and the atmosphere. The droplets are generated by two distinct mechanisms which characterize the drops as either jet droplets or film droplets. The goal of this study is to obtain statistical data about the size of these droplets produced by air bubbles bursting on a non-quiescent free surface and study effects of surfactant on the droplet distribution. Two different surface conditions are created by using clean water and a 0.4% *v/v* aqueous solution of Triton X-100 surfactant. A bubble field is created with air injected through an array of hypodermic needles arranged in a grid pattern and five different bubble production rates are studied for each surface condition. Measurements of the bubble diameters as they approach the free surface are ob-

tained with diffuse light shadowgraph images. A laser-light high-speed cinematic shadowgraph system is employed to record and measure the diameters and motions of the droplets. The movies are processed on a custom-built MATLAB code which measures droplets as small as $100\ \mu m$ to within 7% error. Droplets with diameters between $50\ \mu m$ and $100\ \mu m$ are also measured, but with lower accuracy. The droplet diameter distributions as a function of the bubble production rate and surfactant conditions are reported. The results show a clear distinction between the droplet distributions obtained in clean water and the surfactant solution. A bimodal droplet distribution is observed for clean water with at least two dominating diameter peaks. For the surfactant solution, a single distribution peak is seen.

EXPERIMENTAL INVESTIGATIONS OF THE EFFECTS
OF SURFACTANTS ON DROPLET PRODUCTION BY
BUBBLES RISING TO A FREE SURFACE

by

Karan Dharmesh Parmar

Thesis submitted to the Faculty of the Graduate School of the
University of Maryland, College Park in partial fulfillment
of the requirements for the degree of
Master of Science
2013

Advisory Committee:
Professor James H Duncan, Chair/Advisor
Professor Marino di Marzo
Assistant Professor Johan Larsson

© Copyright by
Karan Parmar
2013

Dedication

For my father's 50th birthday on
12th of May, 2013.

Acknowledgments

I would like to begin by expressing my sincerest gratitude to my advisor, Professor James H Duncan, who provided me with this opportunity to conduct experimental research. Professor Duncan's enthusiasm for Fluid Mechanics and pursuit of scientific progress in this field has been a constant source of motivation for me. His insightful suggestions, vast technical knowledge and the ability to share that knowledge with superior teaching skills enriched my research in many ways. Working with Professor Duncan over the past two and half years has been immensely rewarding and an enjoyable experience.

I would like also to thank members of my thesis committee, Dr. Marino di Marzo and Dr. Johan Larsson for their time and contribution in evaluating this work. I would like to acknowledge Dr. Kenneth Kiger, for providing the glass water tank used in this experiment. I would like to thank all the other members of faculty who i have interacted with over the years. I would like to acknowledge the staff in the Dept. of Mechanical Engineering for supporting this thesis and my graduate studies, in particular Mr. Amarildo DaMata for his help and advising on issues throughout my graduate school career at the University of Maryland.

I also wish to acknowledge my colleagues in the Hydrodynamics lab: Dr. Xinan Liu for providing his large scale expertise in conducting hydrodynamics research and data processing, Dan Wang for her intial guidance in setting up the shadowgraph technique, Dr. Dejun Dai for helping with the processing code, Naeem Masnadi, Nathan Washuta, An Wang, Ren Liu and Dr. Christine Ikeda for their help and

co-operation in multiple areas right through this thesis. It was a joy to be part of such a talented group of people.

On a personal note, i would like to thank all my family members in USA and Canada, in particular my aunt Zankhna Motiram and my uncle Nilesh Motiram for ensuring that i was never home-sick! I would also like to acknowledge my friends and house-mates Nakul Sharma, Amalesh Murali, Arya Rohan and Yash Solanki for their support, friendship and playing no small part in creating a rocking graduate school experience!

Finally and very importantly, i would like to thank my family back home in India, beginning with my grand-parents Kantilal Parmar and Nirmala Parmar for their countless blessings. Words cannot describe how thankful i am to my mother Neela Parmar and my sister Trishala Parmar (*Bubbles!*) for their unwavering love, support and bearing my occasional tantrums! Perhaps, the most important thank you goes to my father, Dharmesh Parmar for his vision and infinite sacrifices spanning two decades without which all this would not be possible.

Of course, if i have inadvertently left out anybody for their contribution to this work, i would like to offer my gratitude to them and all the other people who made this thesis possible.

Table of Contents

List of Tables	vi
List of Figures	vii
1 Introduction	1
2 Literature Review	5
2.1 Overview	5
2.2 Jet drops	6
2.3 Film drops	11
2.4 Bubble bursting and surface life	14
2.5 Current work	15
3 Experimental Setup and Technique	16
3.1 Experimental Setup	16
3.1.1 Tank Construction	16
3.1.2 Bubble-maker Construction	20
3.1.3 Camera and Lens	21
3.1.4 Laser	23
3.1.5 Water Quality	23
3.1.6 Air Quality	24
3.1.7 Needle Size Selection	26
3.2 Experimental Technique	29
3.2.1 Bubble Size Estimation	29
3.2.2 Cinematic Shadowgraph System	32
4 Measurement Techniques	37
4.1 Bubble measurement	37
4.2 Shadowgraph instrument calibration	48
4.3 Shadowgraph droplet measurement	55
4.4 Experimental test matrix	60
5 Results	62
5.1 Drop distributions	62
6 Conclusion and Future work	81
A Estimation of bubble size for Case 5 with clean water	84
Bibliography	86

List of Tables

4.1	Bubble production data for clean water	42
4.2	Bubble production data for surfactant solution	46
4.3	Experimental test matrix indicating the bubbles production rates and bubble sizes for clean water and surfactant solution.	61

List of Figures

1.1	Schematic of drop production mechanisms in the ocean	1
1.2	Film drop generation	2
1.3	Schematic evolution of drop generation	2
2.1	Bubble size versus top jet drop	7
2.2	Bubble size versus top jet drop ejection height	7
2.3	Histograms of jet drops by <i>Spiel</i> [21]	9
2.4	Bimodal nature of jet drops by <i>Spiel</i> [21]	10
2.5	Film drop distributions for seawater by <i>Spiel</i> [19]	12
2.6	Number of drops produced per bubble versus theoretical prediction by <i>Lhuissier et al.</i> [14]	13
2.7	Distribution of drop diameters by <i>Lhuissier et al.</i> [14]	13
3.1	Drawing of the water tank and bubblemaker assembly	16
3.2	Drawing of the water tank with dimensions in meters	17
3.3	Photograph of the experimental setup	18
3.4	Schematic drawing of the bubble-maker	19
3.5	Hypodermic needle & Luer lock	19
3.6	Needle Pattern	20
3.7	Photograph of the bubble-maker	22
3.8	Time evolution of surface tension for clean and Triton X-100 surfac- tant solution	25
3.9	Bubble shapes at needle tip for clean water for 1 inch and 5 inches of air heights in the bubble-maker	27
3.10	Bubble size estimation setup	28
3.11	Bubble rise sequence	30
3.12	Cinematic shadowgraph system	33
3.13	Laser optical system	34
3.14	Drop splatter	35
3.15	Sample shadowgraph image of droplets	36
4.1	Bubble size calibration	37
4.2	Oblate spheroid and bubble	38
4.3	Pixel position of the ellipse fit to bubble perimeter on the image	39
4.4	Bubble in surfactant solution	40
4.5	Bubble diameter variation for clean water with change in air heights in the bubble-maker	41
4.6	Bubble diameter versus volumetric air flow rate for clean water cases	43
4.7	Bubble diameter variation for surfactant solution with change in air heights in the bubble-maker	44
4.8	Bubble diameter versus volumetric air flow rate for surfactant solution cases	45
4.9	Shadowgraph instrument calibration	49

4.10	Calibration images of reticle at various distances from focal plane . . .	50
4.11	Average background intensity	51
4.12	Average intensity of the images of the various dots on a Patterson globe reticle as a function of distance of the reticle from the focal plane of the lens.	52
4.13	Normalized diameter of the images of the dots on the Patterson globe reticle as a function of the distance of the reticle from the focal plane.	53
4.14	Depth of field (DOF) versus drop diameter	54
4.15	Intensity versus Drop Diameter	56
4.16	Sample image used for drop processing	56
4.17	Intensity graph of a sample drop close to the focal plane	57
4.18	Intensity graph of a sample drop positioned away from the focal plane	58
4.19	Measurement Volume	59
5.1	Drop distribution for Case 1 for clean water	63
5.2	Drop distribution for Case 2 for clean water	64
5.3	Drop distribution for Case 3 for clean water	65
5.4	Drop distribution for Case 4 for clean water	66
5.5	Drop distribution for Case 5 for clean water	67
5.6	Bubble rafts for surfactant condition	68
5.7	Drop distribution for Case 1 for surfactant solution	71
5.8	Drop distribution for Case 2 for surfactant solution	72
5.9	Drop distribution for Case 3 for surfactant solution	73
5.10	Drop distribution for Case 4 for surfactant solution	74
5.11	Drop distribution for Case 5 for surfactant solution	75
5.12	Spectral peaks versus bubble diameter for clean water cases	76
5.13	Spectral peaks versus bubble diameter for surfactant solution cases .	77
5.14	Sauter mean drop diameter versus bubble diameter for clean water cases	78
5.15	Sauter mean drop diameter versus bubble diameter for surfactant solution cases	79
A.1	Bubble production rate versus bubble diameter for clean water Case 5	85

Chapter 1

Introduction

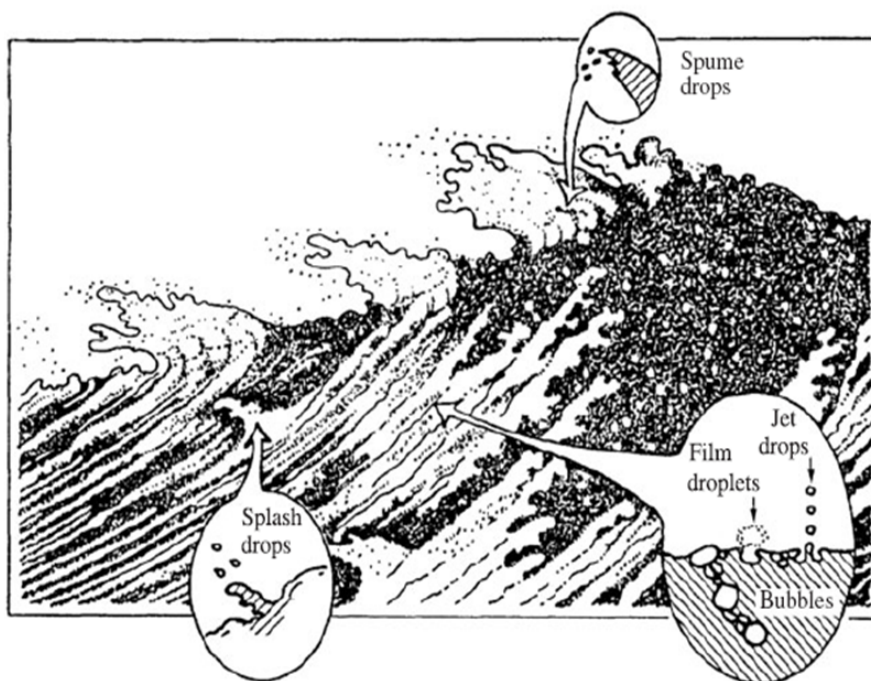


Figure 1.1: Schematic of drop production mechanisms in the ocean. Image from *Lhuissier et al.* [14]

The formation of large droplet aerosols as result of bursting bubbles has been an area of interest for a long time with studies dating back to 1954 [12]. The marine sea-salt aerosol plays an important role in the transfer of heat, mass and various contaminants between the oceans and the atmosphere [10]. It is a well-known fact that breaking waves entrain air bubbles beneath the water surface. Most of the material ejected into the atmosphere from the sea is thought to come from the bursting of these entrained air bubbles. [1]. The efficiency of the transfer of mass

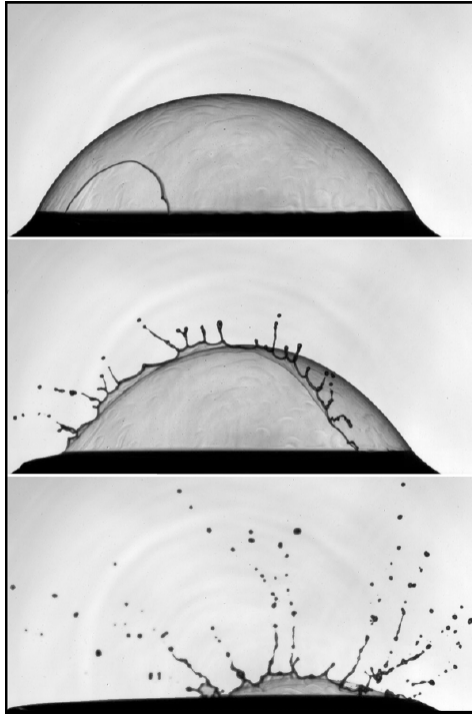


Figure 1.2: Film drops created by rupturing of the bubble. Time between images is 1ms.

Images from *Lhuissier et al.* [14]

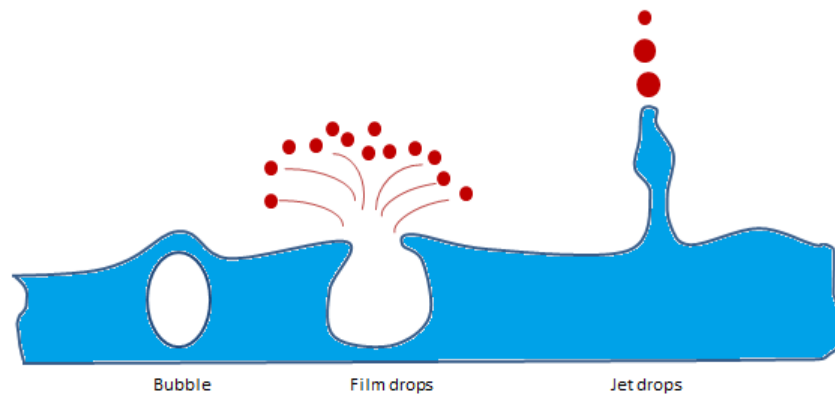


Figure 1.3: Schematic of the evolution of the drop generation process. Film drops are detected after the onset of film breaking and jet drops are detected after the bubble cap rupture is complete.

and CO_2 in this process, is a function of the size and ejection velocity of the drops produced by the bursting of the entrained bubbles [10]. Another, interesting aspect of this process is the transport of salt to the sea surface by bubbles. Studies in this area have also been motivated by damages occurring to mammalian cell structure due to bursting bubbles and droplet ejection at the cellular boundary.

The generation of aerosols is due to at least two distinct consecutive mechanisms. The first droplets to emerge are created by the rupture of the bubble film which separates the bubble's interior from the air above. The rupture in the film causes rapid acceleration of the puncture boundaries which create tiny droplets. These are known as 'film drops' (Figure 1.2) The second mechanism takes place at a somewhat later time as a consequence of the sudden reduction in pressure due to the escape of the bubble gas. An upward unstable jet of liquid is formed at the base of the busting bubble due to surface tension accelerating the surface in radially opposing directions towards each other. This jet usually breaks up to produce what are known as 'jet drops'. A chronology of the drop generation events can be seen in Figure 1.3.

In this study, the interest is in measuring an overall droplet distribution from both jet and film drop processes. Previous studies have been focused on single bubble bursting events which are isolated and take place on a quiescent surface. This study is conducted on non-quiescent surface where a bubble field is created continuously with air injected through an array of hypodermic needles. This system can mimic a real world scenario with random bursting events. The bubble residence time at surface is influenced by the surrounding bubbles and the drops are produced more

randomly ensuring data independence from the plane of recording. The experiments are carried out in a glass tank with a bubble-maker at the bottom. The tank design allows the water surface to be cleaned by skimming. The drop measurements are made 10mm above the free surface.

This thesis is organized in six chapters. Chapter 2 contains a review of previous studies. Experimental setup and data collection techniques are described in detail in Chapter 3. Chapter 4 discusses the instrument calibration and data processing methodologies. Chapter 5 and 6 summarize the results and provides some conclusions respectively.

Chapter 2

Literature Review

2.1 Overview

The formation of jet drops was first identified by *Jacobs* [11]. *Kientzler et. al.* studied the jet drops ejected from bubbles of sizes $200\mu m$ to $1800\mu m$ in diameter bursting at a water surface. Their observations led them to conclude that the jet drop diameter is roughly one-tenth of the bursting bubble diameter [12]. This has been known in the literature as the “1-to-10 rule.” It was also reported that bubbles diameters that are of a micron scale, never produces more than ten jet drops per bubble [1]. Film drops concerning bubbles of the millimeter scale were identified by *Knelman et. al.*. The disintegration of the thin bubble cap, produces hundreds of film drops per bubble and this process has been studied in some detail by *Blanchard & Sysdek* [4], *Resch & Afeti* [16] and *Spiel* [19]. Some of key literature is discussed in detail in the next few sections.

2.2 Jet drops

The size distribution of the sea salt aerosol requires understanding of the size and ejection height of both jet and film drops as a function of bubble diameter. *Blanchard* [3] presented some data about the top (*highest ejected*) jet drop size as a function of the bubble diameter from scattered sources. It was observed that the 1-to-10 rule which was put forward by *Kientzler et. al.* [12] holds in sea water for bubbles with diameters less than $500\ \mu\text{m}$. As seen in the Figure 2.1, the data for this study was obtained from 11 different bubble sizes that ranged from $100\ \mu\text{m}$ to over $2000\ \mu\text{m}$ in diameter. The temperature of the seawater was between $22^{\circ}\text{C} - 26^{\circ}\text{C}$. Also shown in the graph are data for the top jet drop diameter from seawater at 4°C . The height to which the top jet drop is ejected increases with bubble size and decreases with decreasing water temperature (Figure 2.2). The data suggests that the slight differences in surface tension and viscosity between seawater and distilled water at the same temperature are not enough to change the dynamics of jet drop ejection. [3]

Spiel [21] presented the jet drop size distribution as a function of bubble diameter ranging from $700 - 3000\ \mu\text{m}$ for fresh and sea water. It was reported that from the second jet drop onward, the diameter results are bimodal, although it wasn't clear why this is so. This can be seen in Figure 2.4. The plots show bimodality for the first four jet drops after the top drop which doesn't show a bimodal nature in fresh water for different radii of bubbles. All of the results discussed here are for fresh water at a temperature of $20 \pm 3^{\circ}\text{C}$. In Figure 2.3, histograms show the

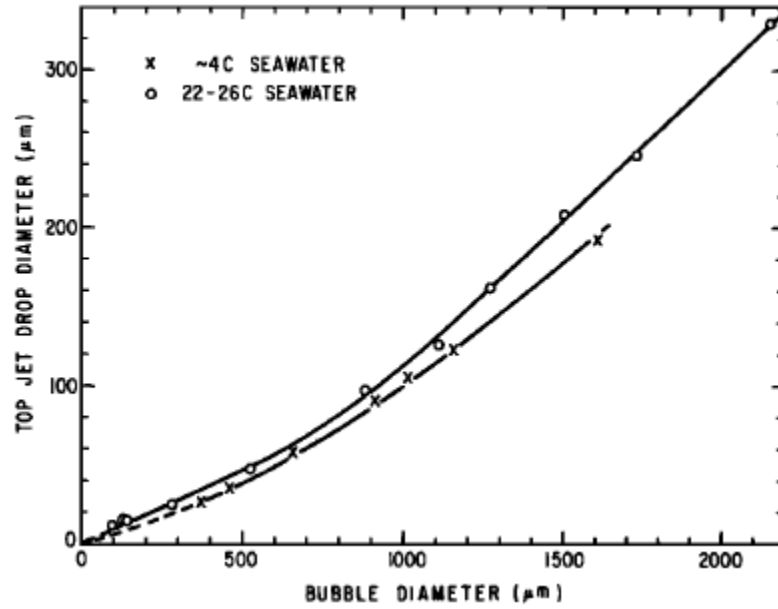


Figure 2.1: Relationship between bubble diameter and the top jet drop diameter from bubbles bursting in seawater at temperatures of $40^{\circ}C$ and $22^{\circ} - 26^{\circ}C$. [3]

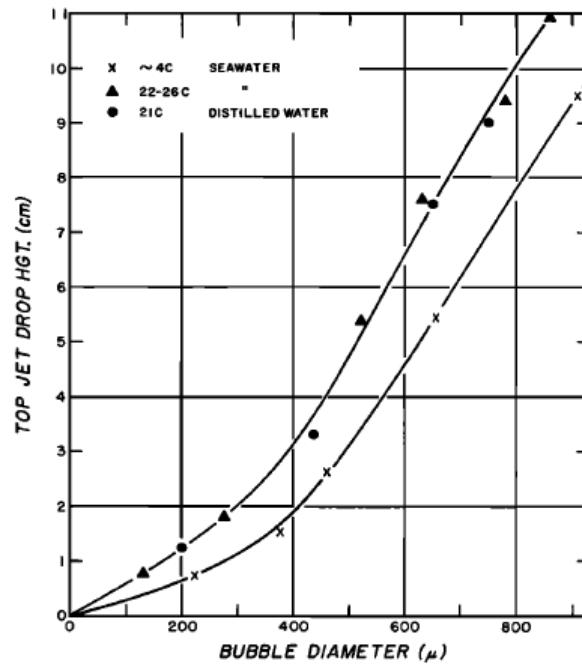


Figure 2.2: Relationship between bubble diameter and height to which the top jet drop is ejected from bubbles bursting in distilled water and seawater at various temperatures [3]

number of the jet drops and radius in relation to the radius of the collapsing bubbles. The numbers 1 to 6 in these plots represent the drops observed sequentially after the bubble popping with 1 representing the first drop (top drop) seen. In this thesis, results of similar nature are seen for “clean” water conditions with a similar temperature of the water but with continuous bubble production unlike *Spiel’s* work where bubbles were made one at a time on demand. [21]

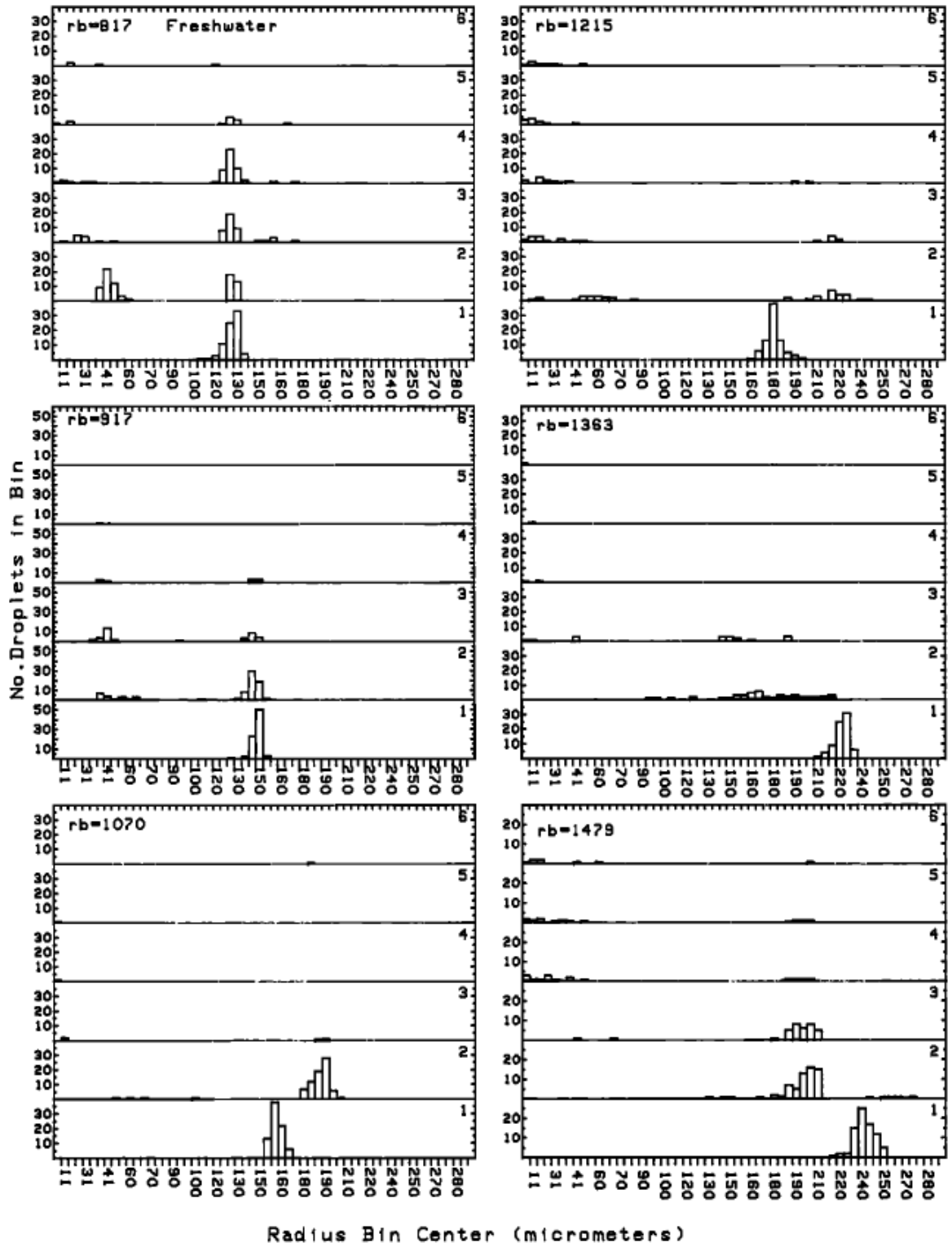


Figure 2.3: Histograms of jet drops by. r_b = Bubble radius. The numbers 1 to 6 in these plots represent the drop observed sequentially after the bubble collapse with 1 representing the first

drop (top drop) seen. [21]

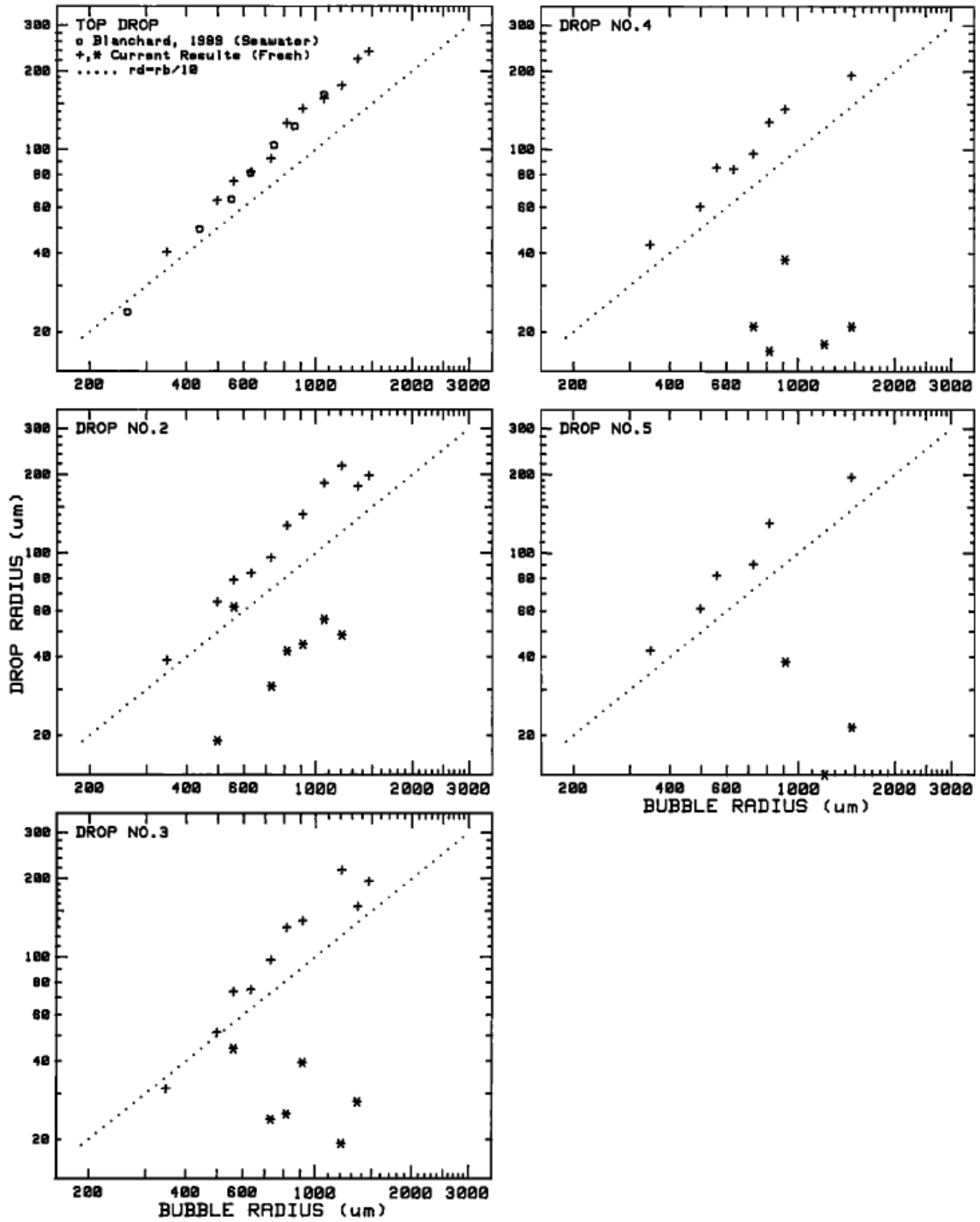


Figure 2.4: Plots of the average jet drops in fresh water as a function of bubble radius for drop numbers up to five. The dotted line is the curve $r_d = r_b/10$, where $r_d =$ Drop radius and $r_b =$ Bubble radius. Drops 2 to 5 are the drops observed sequentially after the top jet drop and are bimodal. The circles in the plot for the top drop are from *Blanchard* [3]. [21]

2.3 Film drops

Spiel [19] presented a study on film drop production and the upper limit on the film drop diameter for a given bubble diameter for seawater. The author suggests that the film drops are of two kinds, ‘primary’ and ‘secondary.’ The primary film drops are those that are produced from the direct rupture of the bubble cap. Secondary drops are created when the surface tension is insufficient to keep bits of the rapidly advancing toroid(bubble cap) from tearing loose and horizontal droplets impact the water’s surface with sufficient force, to create the vertical cloud of droplets. Results presented by the author include the drop size, speed of launch and spatial distribution of the bubbles. The bubbles diameters ranged from from 2.94 mm to 12.57 mm. Film drops recorded were 10 μm to 400 μm in diameter keeping in mind that 10 μm was the precision limit of the setup. The author observed no film drops for bubbles less than 2400 μm in diameter. In Figure 2.5, the film drop size distribution is given for eight bubble diameters ranging from 2.94 mm to 12.57 mm.

From this data, the author proposed an equation for predicating the diameter of film drops for a given bubbles radius.

$$D_d = 2 \times 3.57 \{ 2\gamma R_o (1 - \cos(31.3)) / (S_f^2 \rho \pi \sin(31.3)) \} \quad (2.1)$$

D_d : Initial drop diameter γ : Surface tension R_o : Bubble cap radius of curvature

S_f : Film speed [19]

Lhuissier et al. [14] presented a detailed paper on bubble bursting aerosols. The authors present theoretical expression for bubbles deflation time. They measured film drop size distribution and compare it with a theoretical expression for number of drops

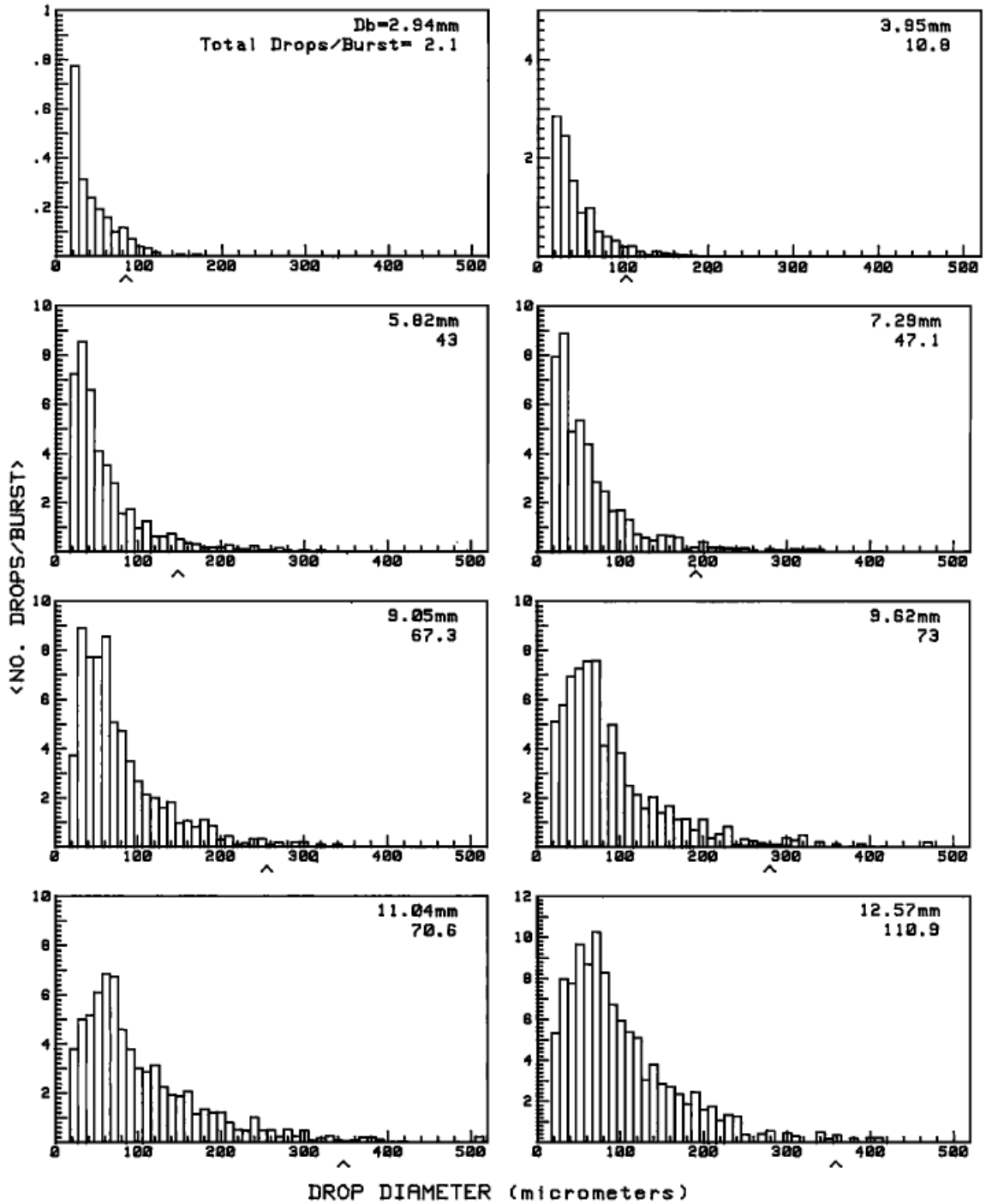


Figure 2.5: Distributions of film drop diameters for eight bubble diameters for seawater. The

smallest bin width was $10 \pm 5 \mu\text{m}$. [19]

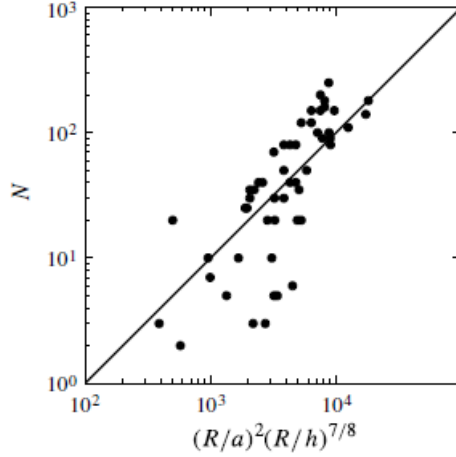


Figure 2.6: Number N of drops produced per bubble versus prediction of equation given by [14]. The line is $y = 10^2 x$.

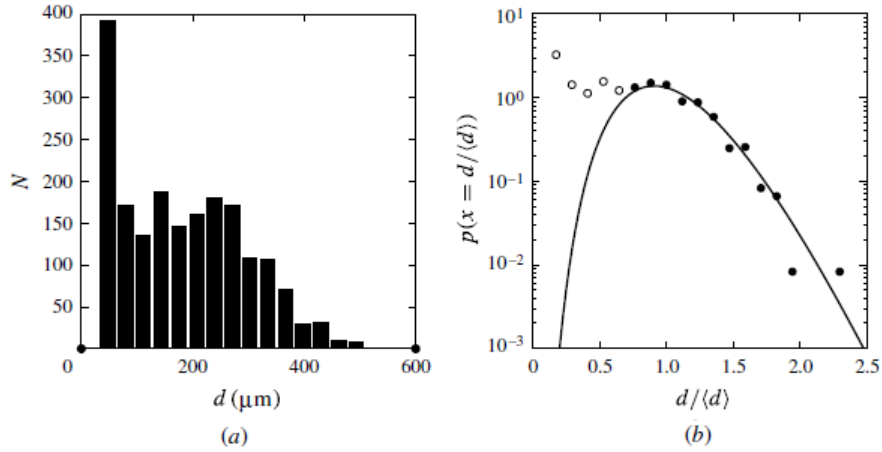


Figure 2.7: (a) Original data and (b) Normalized drop diameter distribution (dots) and fit by a Gamma distribution [14]

$N \sim (R/a)^2(R/h_b)^{7/8}$ where R is the cap radius of the bubble, a is the capillary length and h_b is the film thickness. [14] The performance of this expression in comparison to the experimental data is shown in Figure 2.6. Bubbles 12 mm in radius were burst using a hydrophobic sand-coated needle to ensure the same bubble size every time and the film drop distribution data is represented with a gamma distribution shown in Figure 2.7. The data represents almost 2000 drops.

2.4 Bubble bursting and surface life

Research has also been conducted in studying the surface residence time for bubbles prior to bursting. This residence time becomes important when dealing with surfactants. *Struthwolf et. al.* [22] studied the surface residence time of air bubbles from 50 μm to 400 μm in diameter. The authors observed that for distilled water, air bubbles greater than 200 μm in diameter, the bubble surface life is less than 0.05s while for air bubbles less than 200 μm in diameter, the bubble surface life is greater than 0.05s. The results were opposite for sea water.

Dey et. al. [9] presented a study of surfactant effects on the bubble bursting phenomenon. The study was motivated by the bubble bursting at a cellular boundary and investigating the role of surfactant in possibly reducing cellular damage. The authors presented the change in height with time of the liquid jet created after bubbles of 200 μm in diameter are burst at the free surface. The liquid jet breaks up to produce jet drops. The authors measured surface tension and viscosity effects on bursting bubbles. The experimental technique had continuous bubble production from a single needle with no interaction between subsequent bubbles. A numerical model is also put forward and the results of this model show some discrepancy with the experimental results.

2.5 Current work

In this thesis, data is presented towards understanding the role of surfactant in droplet production on *non-quiescent* surface conditions which has not yet been reported in published material in detail. Measurements are made for drops ranging from 100 μm to 3000 μm in diameter to within 7% error in diameter. The drops smaller than 100 μm are also observed and noted although the error in measurement is higher than 7%. High speed (1000 fps) cinematic shadowgraphs are recorded and discrete frames containing the drops of interest are processed with a custom built MATLAB code. Initial conclusions are drawn on the data for clean water and surfactant solution cases with five bubble diameters for both cases.

Chapter 3

Experimental Setup and Technique

3.1 Experimental Setup

3.1.1 Tank Construction

The experiments are performed in a glass water tank equipped with an acrylic bubble-maker at its bottom (Figure 3.1).

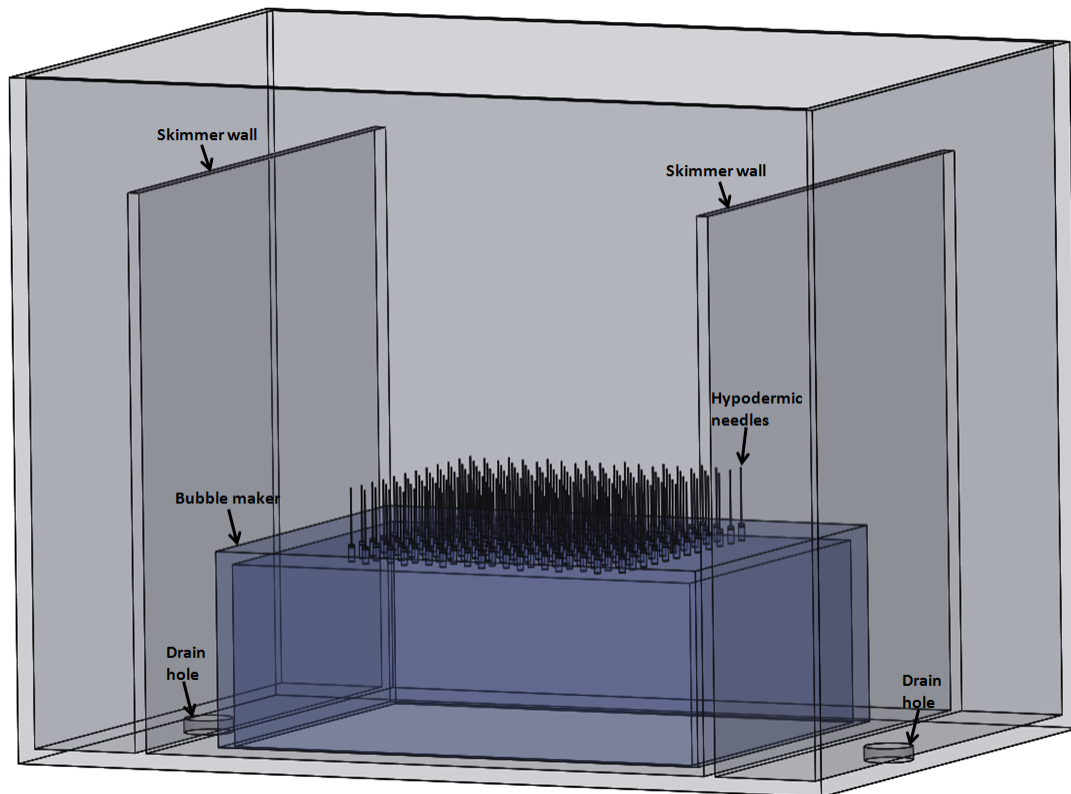


Figure 3.1: Drawing of the water tank and bubblemaker assembly.

The glass water tank is 0.91 meters(m) in length, 0.61 m high and 0.46 m wide. The thickness of the glass is 0.01 m. The tank has 2 vertical partitions which run parallel to

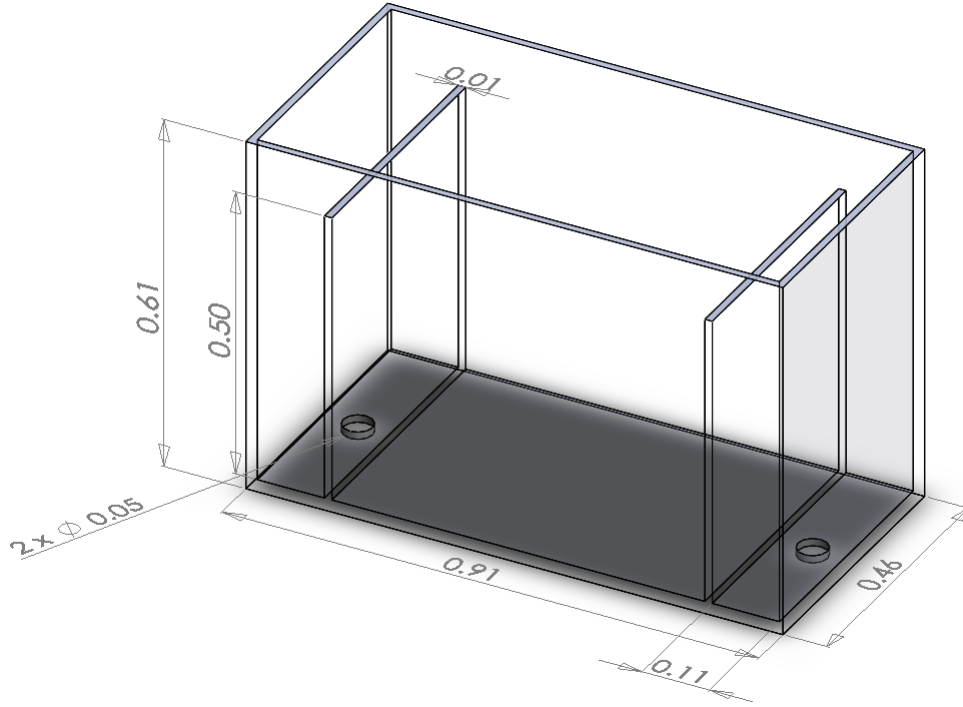


Figure 3.2: Drawing of the water tank with dimensions in meters.

the width and are 0.5 m high and located 0.11 m from the either edge along the length (Figure 3.2). These are referred to as skimmer walls. Since their height is less than the tank edges, water flows over them and the surface can be skimmed when desired. A 0.05 m diameter hole is provided at the bottom, in-between either skimmer wall and the edges of the tank. These holes have bulkhead fittings on them and the skimmed water is taken out of the tank from here via PVC pipes. The tank sits on a wooden base which is atop a 0.91 m high metal table from the ground. The wooden base rests on four adjustable legs which are used to level the tank to keep similar flow rates over both skimmer walls. A Styrofoam sheet is placed between the tank the base for cushioning. A tank-frame is constructed out of 80/20® modular aluminium framing, around the glass tank. The frame is attached on to the metal table with C-clamps. This frame is used to mount various peripherals and optics as needed. A separate frame is built to mount the camera and is clamped on the table. A photograph of the setup can be seen in Figure 3.3.

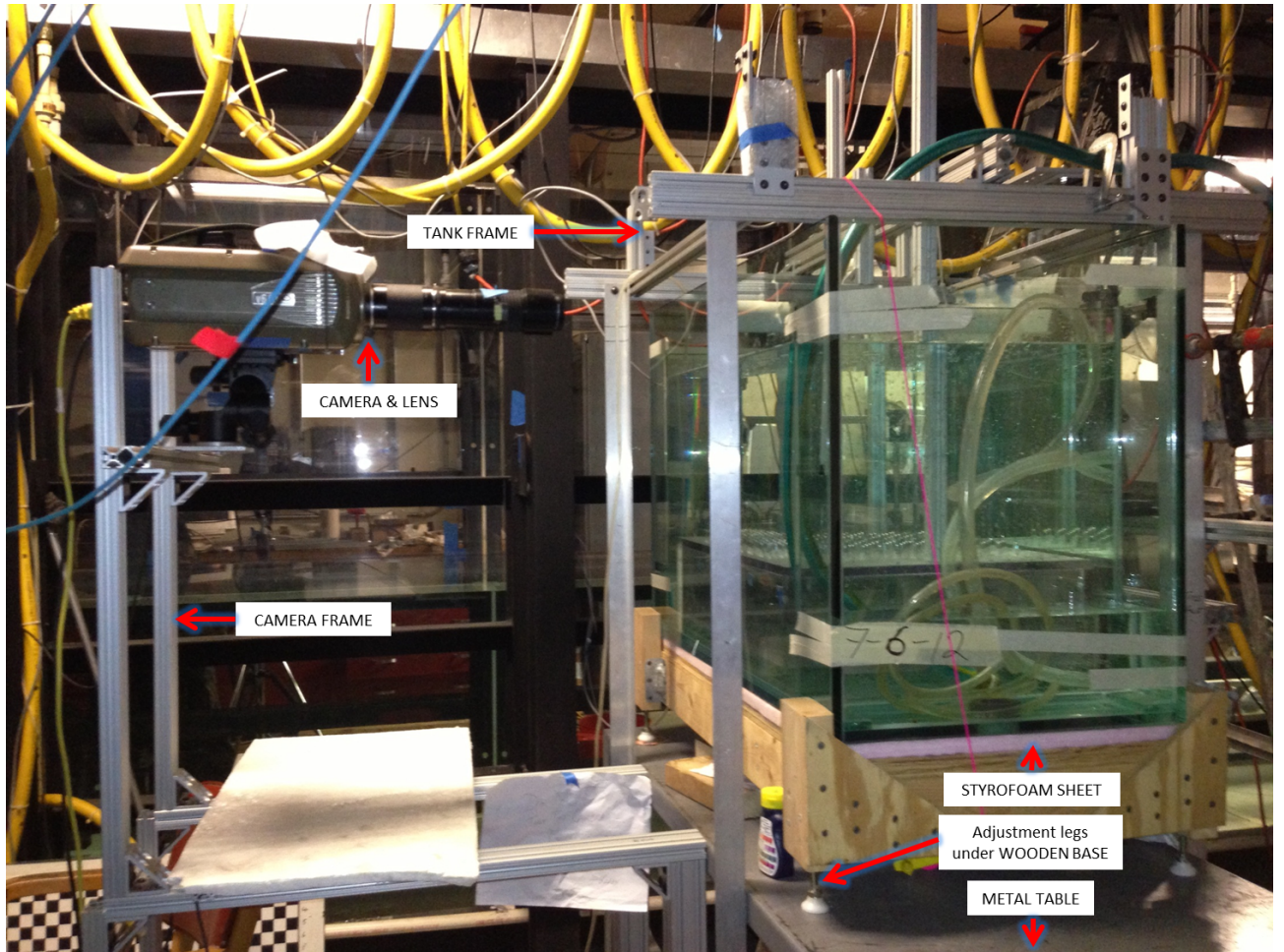


Figure 3.3: Photograph of the experimental setup.

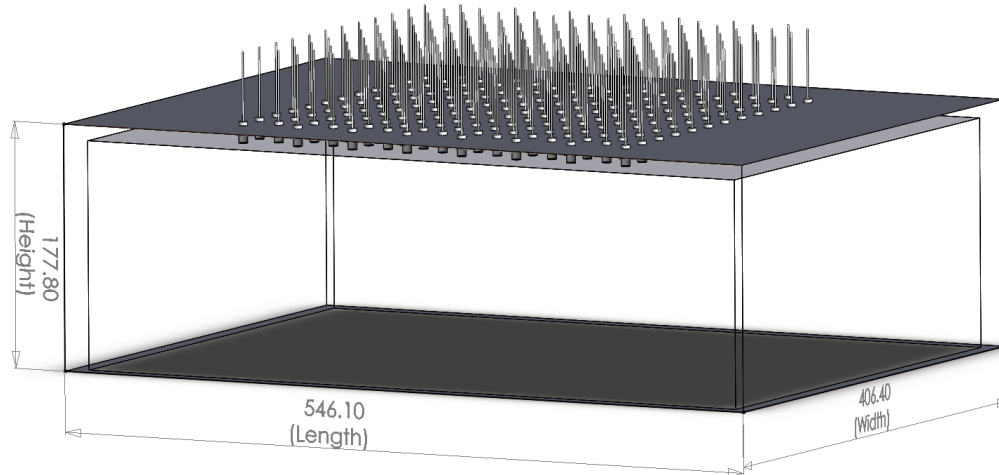


Figure 3.4: Schematic drawing of the bubble-maker (Dimensions in mm).

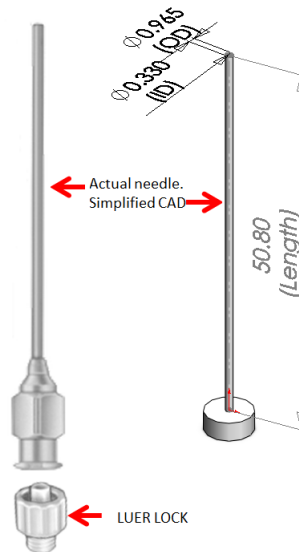


Figure 3.5: Hypodermic needle & Luer lock (Dimensions in mm).

3.1.2 Bubble-maker Construction

The bubble-maker is a 5 sided open rectangular box made by fusing 12.7 mm thick acrylic plates with Methylene Chloride (Figure 3.4). It is placed at the bottom of the glass tank and is held in position by two vertical aluminium pieces attached to the tank-frame and in contact with the top surface of the box.¹ These two pieces exert a downward force on the box preventing it from rising due to buoyancy when the water tank is full. The box is 546.1 mm in length, 177.80 mm high and 406.40 mm wide.

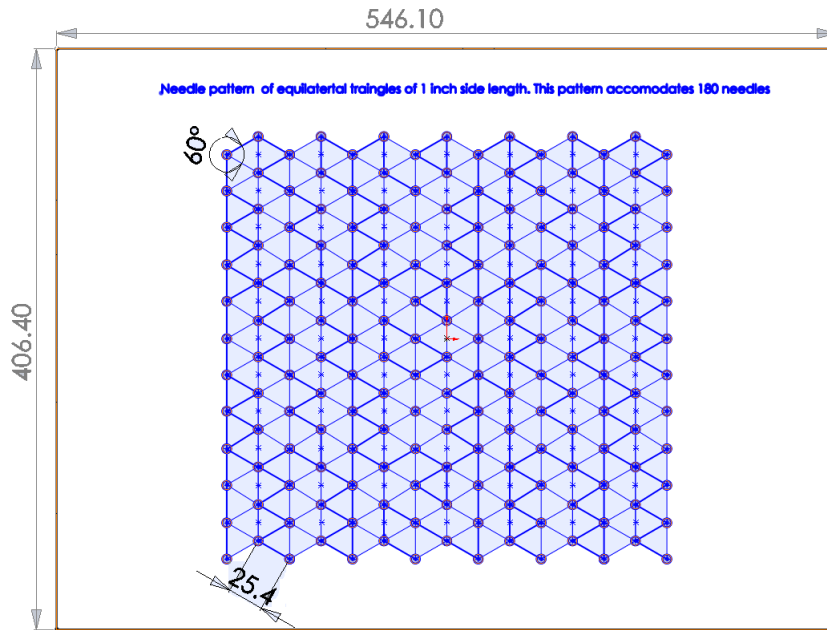


Figure 3.6: Needle pattern: The needle locations are shown by blue circles (Dimensions in mm).

On the top surface of the box, 180 needles are mounted vertically on an array of holes to allow air to allow air in the acrylic box to escape through the needles. The needles have unbeveled blunt tips and are made out of stainless steel with nickel-plated brass luer lock hubs. The hub locks on to the top of a polypropylene quick-turn luer lock coupling which has a male thread $1/4'' - 28$ at its bottom (Figure 3.5). These threaded section are then screwed on to the top of the box and sealed with a temporary silicone sealant. The

¹The words 'box' and 'bubble-maker' are used interchangeably

needles are organized in an equilateral triangle pattern with side length 25.4 mm. The length 25.4 mm is chosen such that there is intermingling of the bubbles as they rise to the free surface. The pattern can be seen in Figure 3.6. The arrangement occupies an area just under $304.8 \text{ mm} \times 304.8 \text{ mm}$ on the box. One end of a 6.35 mm diameter air hose is taped on to the underside of the bubble-maker and the other end is connected to a compressor. A vertically oriented 6" ² ruler is glued on one side of the box to note the height of the air-water interface in the box. As the air flow rate from the compressor is increased, the height increases, the air-water interface moves down and the bubbles produced per unit time increase. In this experiment, droplet production is studied for 5 different positions of the air-water interface. (i.e. 5 different rates of bubble production) (Figure 3.7). The change in the bubble production rate is also accompanied with a change in the bubble diameter.

3.1.3 Camera and Lens

In all the experiments conducted, the data is collected in the form of high speed movies and the primary recording device is a Phantom v640 high-speed camera from Vision Research. The camera is capable of a frame rate up to 1500 frames per second with a full resolution of 2560×1600 pixels. The minimum exposure time is rated at $1\mu s$. The camera is used with a Nikon 200 mm microfocal lens with magnification of one to one at the minimum focal distance.

²This height of the meniscus will always be expressed in English units (inches for convenience)

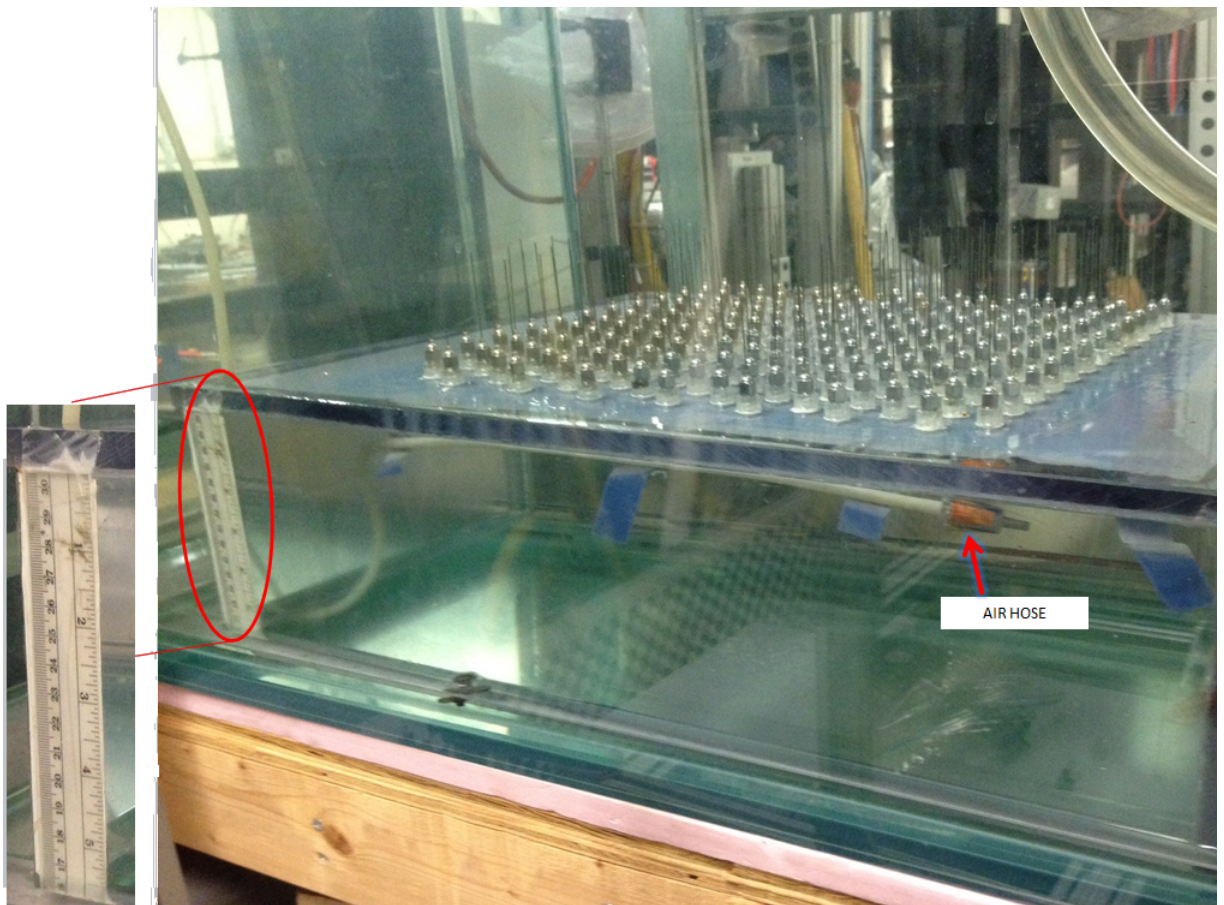


Figure 3.7: Photograph of the bubble-maker inside the tank.

3.1.4 Laser

A 75W pulsed Nd:YLF laser from Photonics Industries is used to create a narrow beam of light roughly 31.75 mm in diameter which illuminates the sensor of the v640 camera. The laser is rated for pulse energy of 50 *mJ*@ 1 *kHz* with a pulse width of 130 *ns*@ 1 *kHz*. The laser output wavelength is 527 nm(Green).

3.1.5 Water Quality

In order to ensure repeatability, it is very important to have good control on the surfactant concentration. In the following sub-sections, water treatment is discussed for two surfactant cases. The evolution of surface tension with time can be seen in Figure 3.8.

Clean Water

The start of each experiment begins with an empty tank which is filled with tap water passed through a 0.5 μm filter. As the tank fills up, water flows over the skimmer walls. The filling flow-rate is then slowed down and the surface is skimmed for half an hour. Skimming is stopped and to neutralize the organic matter in the water, hypochlorite is added at a concentration of 10 p.p.m. The water is now ready for the first run of experiments and the bubble-maker is turned on. A 'run' constitutes five different air bubble production rates corresponding to air heights starting at 1" and going up to 5" of air in increments of 1". During a run, the water gets skimmed over the skimmer walls as the amount of air in the bubble-maker is increased which displaces the water. After the completion of the run, tap water is added through the same filtration unit, the hypochlorite concentration is restored to 10 p.p.m and next run is made.

Prior to starting the first run, the temperature of the water is recorded and the static surface tension is measured with a Wilhelmy plate tensiometer from NIMA. The temperature of the water is in the range $16^{\circ}C - 20^{\circ}C$. The surface tension settles to 72.8 mN/m for the clean water condition.

Water with surfactant

The preparation for surfactant laden water is similar to clean water in terms of skimming and chlorination. After the initial treatment, 80 ml of a 0.4% *v/v* solution of Triton X-100 surfactant is added to the tank. This drops the surface tension to 59.9 mN/m. At the end of the day, the surface tension is measured again for verification. The surface tension of the Triton X-100 solution at the critical micelle concentration (CMC) is 30.5 mN/m. [15]

3.1.6 Air Quality

Air is supplied to the bubble-maker from a Craftsman (6 hp, 33 gallons) compressor which gives upto about 243.5 liters/min at 275.80 kPa. It is connected to a two-stage fine particle and oil removal air filter. Stage one removes particles down to 1 micron and oil droplets down to 0.5 ppm; stage two removes particles down to 0.01 microns and oil droplets down to 0.01 ppm. the filter is coupled straight to an inline flow meter with a regulator valve which is rated for a max flow 5 lpm. The air is supplied to the bubble maker from here with a quarter inch diameter air hose.

Surface tension evolution for Clean & Triton X-100-laden water

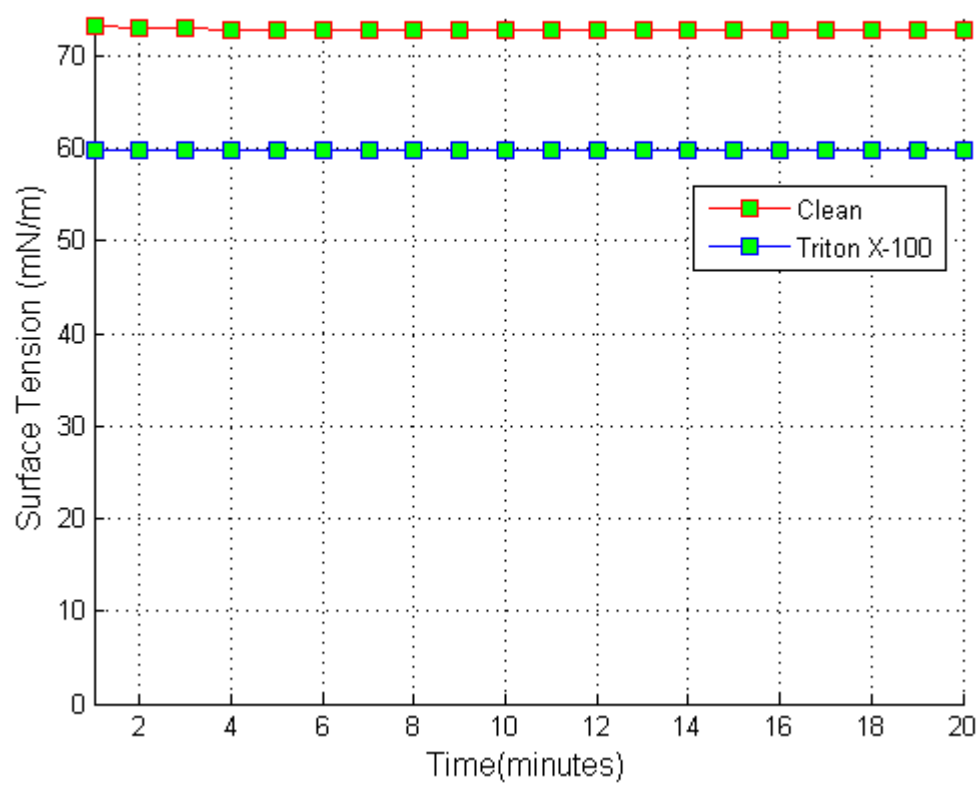


Figure 3.8: Time evolution of surface tension for clean and Triton X-100 surfactant solution.

3.1.7 Needle Size Selection

A fixed size needle is used for all the experiments. The size of the needle was decided after making trials with different sizes with inner diameters (I.D) ranging from 1.19 mm (16 gauge) to 0.254 mm (26 gauge). The I.D for the needles increases with decreasing gauge size. The criteria for needle selection was the bubble size at the free surface. In order to estimate the bubble size, the bubble-maker was fitted with one needle only and the high speed movies were recorded with the lens focused at the tip of the needle. In Figure 3.9, we can see the air bubbles as they leave the tip of the different size needles for 1" and 5" of air heights in the bubble-maker. The behavior of the air flow at the tip of the needle was examined for the presence of bubble-like structures which are released in a discrete fashion. A few candidate needle sizes were chosen for a more detailed analysis. Measurements of the bubble size just below the free surface were made and the size 23 gauge with I.D. 0.33 mm and length 50.8 mm is chosen (Figure 3.5). This size provided the most consistent bubble-like structures for all air flow-rates and was not prone to clogging. The bubble size estimation set-up is discussed in detail section 3.2.1 and the image processing technique in section 4.1.

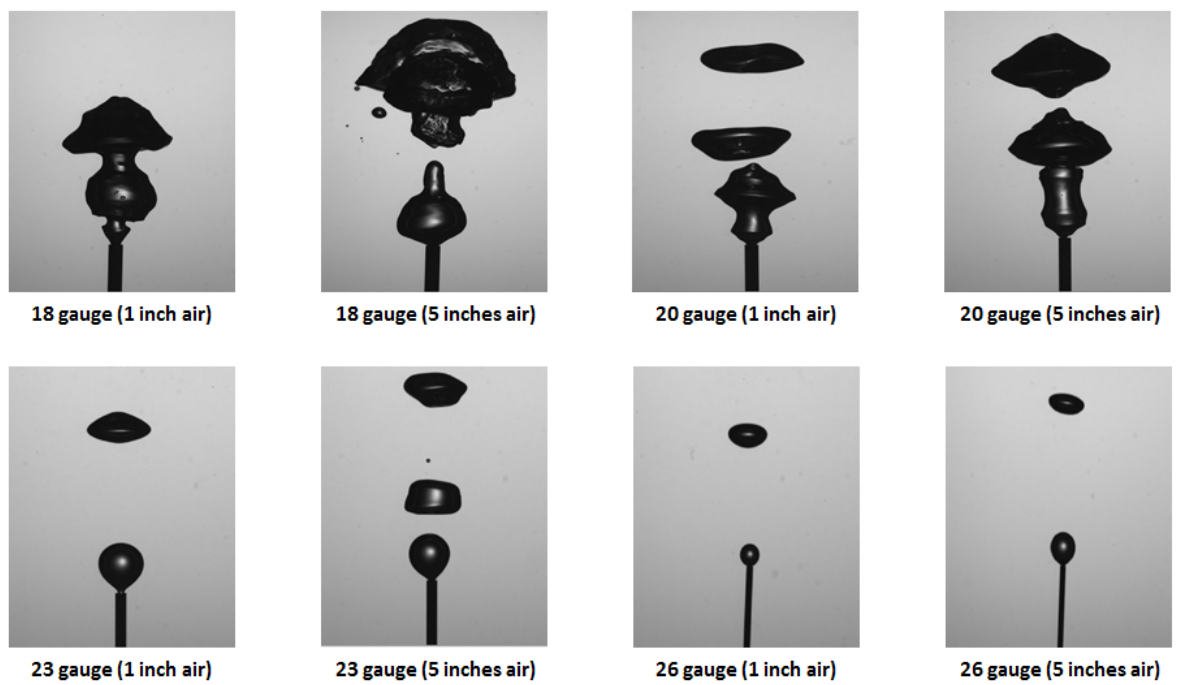


Figure 3.9: Bubble shapes at needle tip for clean water for 1 inch and 5 inches of air heights in the bubble-maker

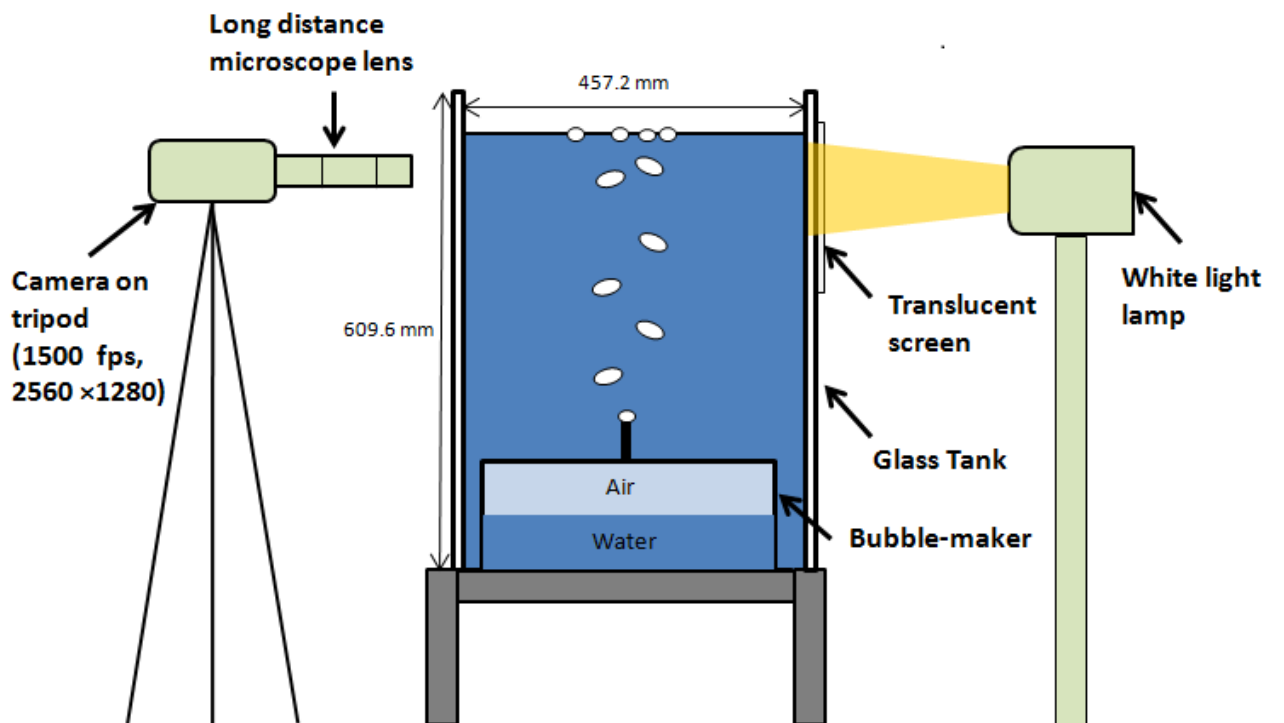


Figure 3.10: Bubble size estimation setup: A schematic showing an end view of the tank with camera and white light lamp. Single needle is used in this setup.

3.2 Experimental Technique

3.2.1 Bubble Size Estimation

In order to have a quantitative estimate of the bubble size near the free surface, high speed movies of the rising bubbles are recorded just underneath the free surface. This portion of the study was conducted prior to assembling the needle array on the bubble-maker. At this stage, only one needle is assembled on to the bubble-maker. This helps in finding out the number of bubbles per unit time from a single needle and the size of the bubbles for different heights of the air-water interface in the bubble-maker. The experiment is conducted for both clean and surfactant-laden water. A schematic diagram of the setup can be seen in Figure 3.10. The camera is mounted on a tripod and it is focused on to the bubbles just underneath the free surface. The resolution for the camera is set to 2560×1280 . The field of view of the camera is $62.7 \text{ mm} \times 31.3 \text{ mm}$. The movies are shot at 1500 fps. A translucent sheet is stuck on the side of the glass tank close to a light source. White back-light illumination is used for this experiment. The sequence of bubbles coming to the free surface can be seen in Figure 3.11. The bubbles are darker in comparison to the background and are visualized very clearly in the focal plane.

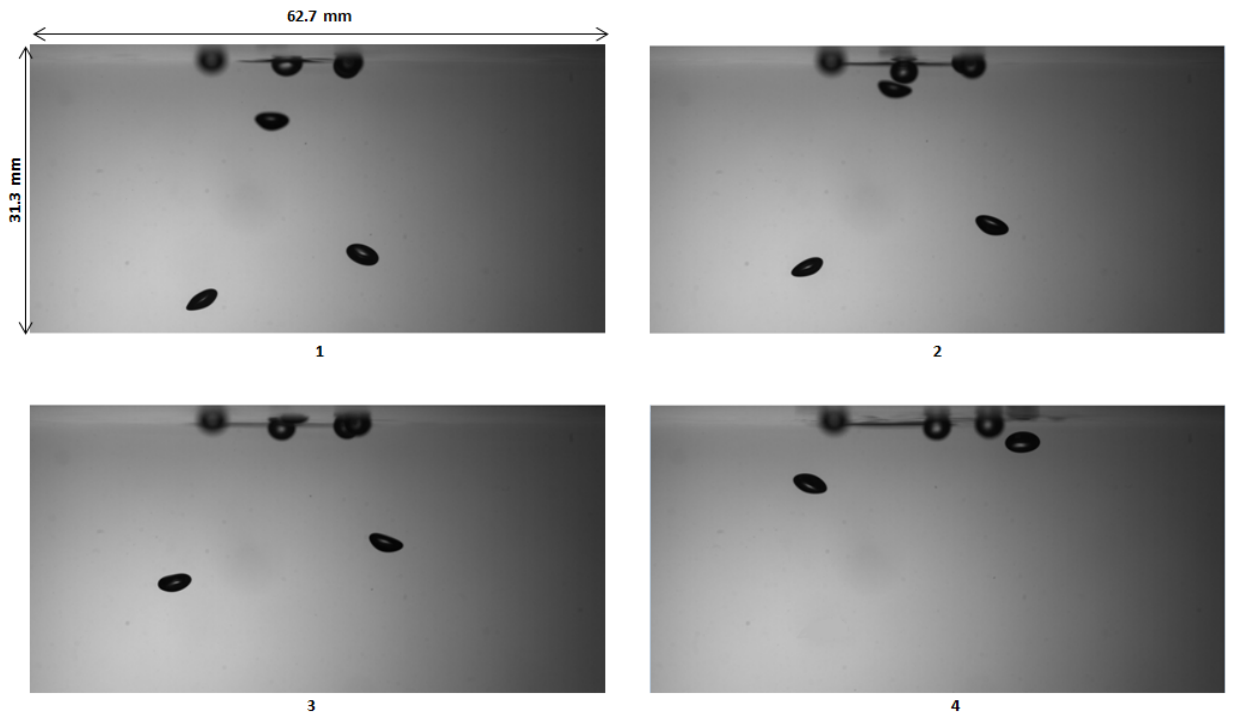


Figure 3.11: Bubble rise sequence: Two bubbles in clean water rising to the free surface location where previously accumulated bubbles can be seen. Time increases sequentially from image 1 to 4 clockwise. The time interval between image 1 and image 4 is 63.32 ms.

The experiment is started by opening the valve on the compressor which allows air to flow in to the bubble-maker and turn on the bubble production. The water in the bubble-maker will start getting displaced with the air. This will result in the free surface of the water rising and causing a flow over the skimmer walls. The air flow rate is adjusted to push the meniscus of the air-water interface in the bubble-maker down at a steady rate. The position of the meniscus is monitored with the ruler on the bubble-maker. As the meniscus reaches the 1" mark on the ruler, the air flow is slowed down considerably and the camera is triggered. The recording length of the movie is about 1 second. This duration is very small compared to the time it takes for the meniscus to move a small distance of $1/16''$. The free surface is hence considered stationary while the data is collected. This is also verified by the stopping of water overflow past the skimmer walls. Once the recording is complete, the air flow is increased which causes the meniscus to move down past the 1" mark and skimming more water from the top. The process is then repeated for meniscus position from 2" to 5". Using this technique, it is ensured that the water surface is skimmed for every air flow condition and a consistent surface condition is maintained. It is interesting to note that the bubbles appear to be ellipsoidal in shape. They rise to the free surface by following a helical path. The calibration and measurement technique is discussed in Chapter 4.

3.2.2 Cinematic Shadowgraph System

The cinematic shadowgraph system is used to measure the droplet distribution. The schematic diagram of the experimental setup can be seen in Figure 3.12. The system uses an expanded laser beam (38.1 mm diameter) from a pulsed Nd:YLF laser (50 mJ/pulse). The laser sits on an optical table which is on top of the instrument carriage of a wave tank, 2.4 m from the ground. The wave tank is located beside the droplet experiment. The arrangement is so because the laser is shared with another experimental setup. The laser optical system is shown in Figure 3.13. Light emitted from the laser cavity is passed through a half wave plate and a polarizing beam splitter and once more through another set of the same arrangement. This is done to control the beam intensity. The light is then passed through a set of spherical lenses which focus the beam on to a pin hole with a 200 μm diameter. The pin hole serves as a spatial filter. After the pinhole, the light goes through a concave lens and thereafter a convex lens which expands the beam to the required diameter. The beam is turned by high energy mirrors (M1-M5) as and when needed. The beam is parallel and 10 mm above the free surface of the water in the tank. The beam alignment is fine tuned and it is projected on to the sensor of the Phantom v640 high speed camera equipped with a Nikon 200 mm microscope lens. The lens has magnification of one to one at minimum focal distance. The dimensions of the frame built to mount the camera is governed by the need to have this minimum focal distance in the middle of the tank. This gives a symmetric depth of field which will be discussed in more detail in the section 4.2. The aperture of the lens is fully open with f -stop at minimum ($f/4$).

The operation of the bubble-maker and the surface skimming system is identical to the process described in section 3.2.1 but with all the 180 needles attached. Once the

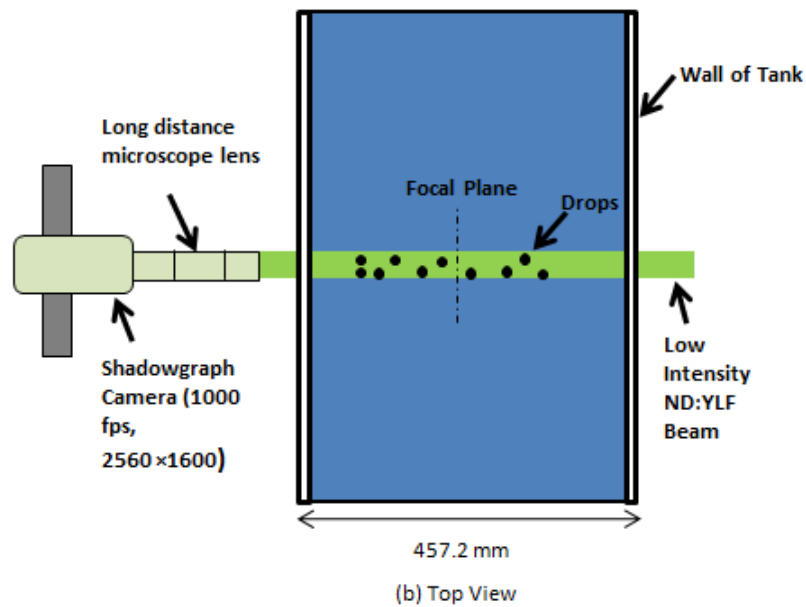
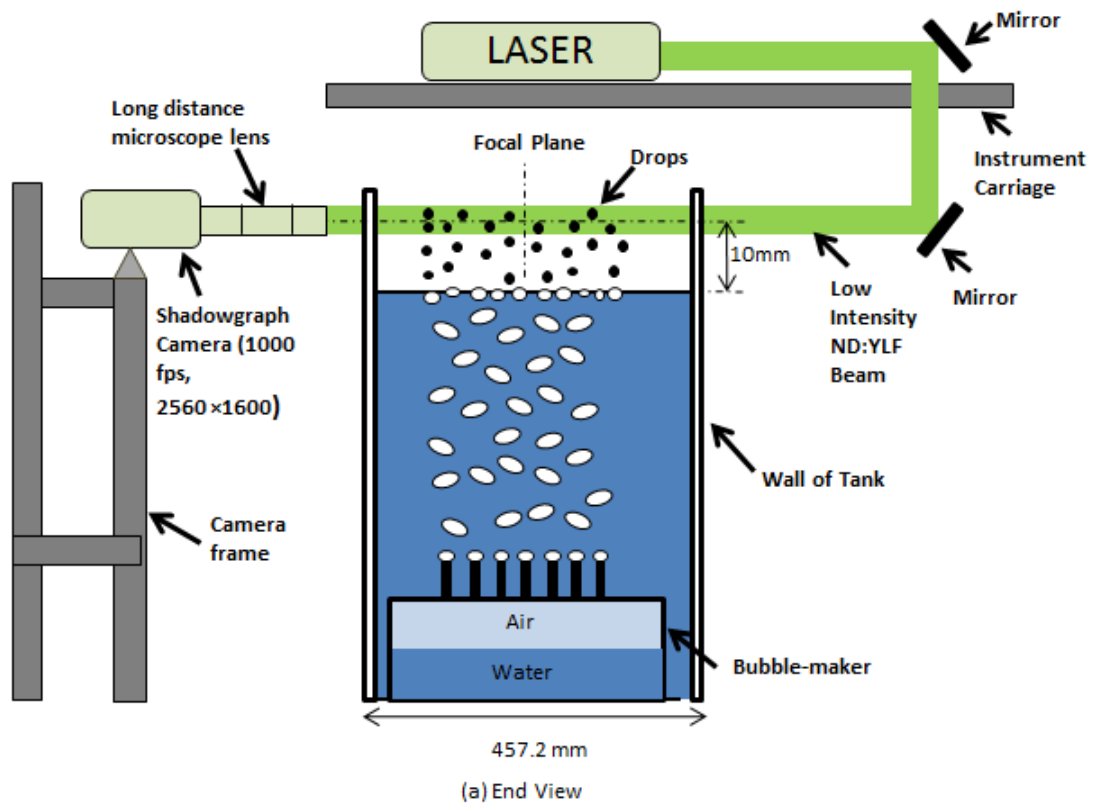


Figure 3.12: Cinematic shadowgraph system: (a) End view of the tank. (b) Top view of the tank.

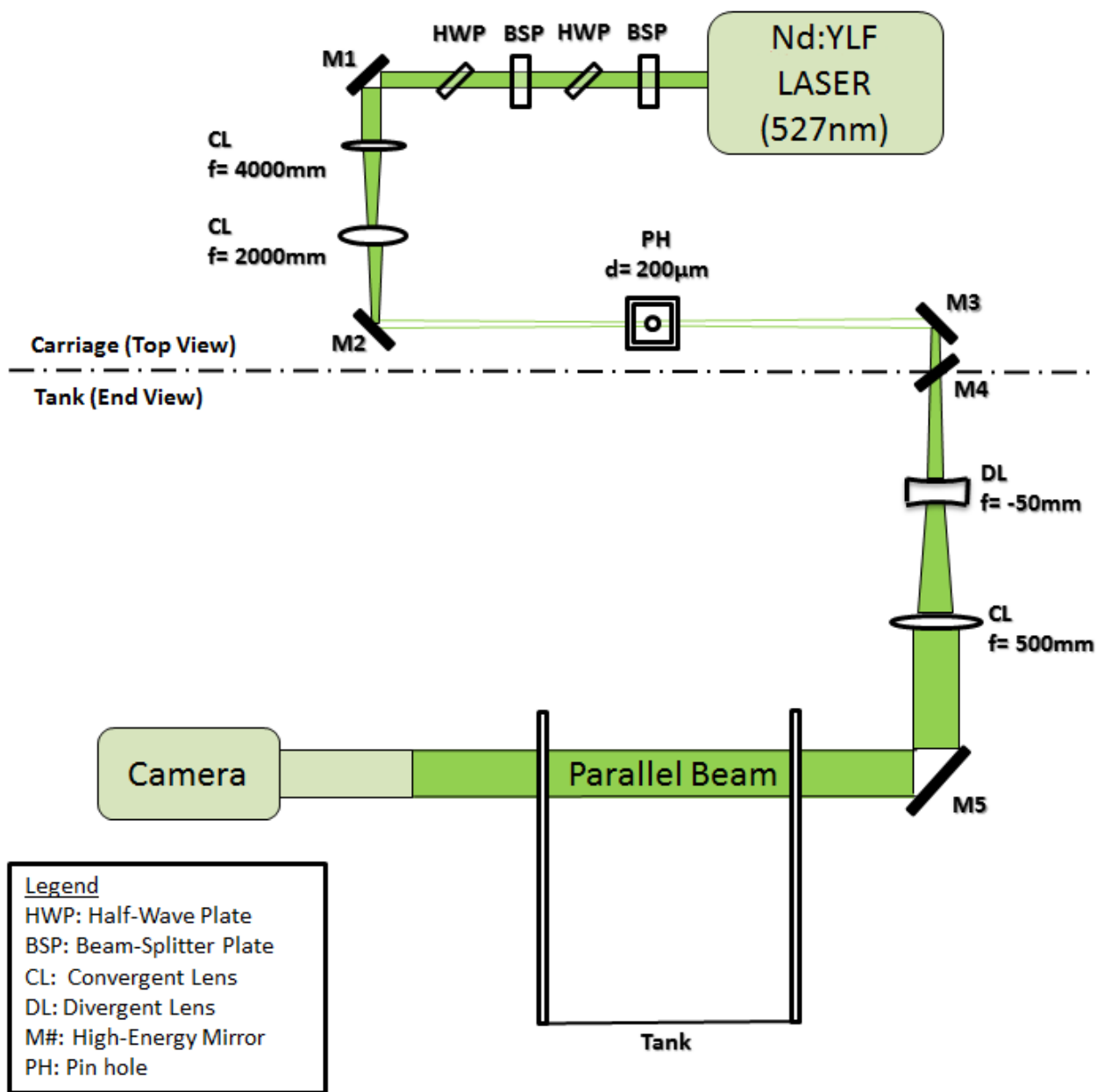


Figure 3.13: Laser optical system: Devices used to create the expanded parallel beam of light.

bubble-maker is turned on, the drops ejected at the free surface in all directions tend to be deposited on the inside glass surface of the tank. This splatter adds noise to the measurements. The issue is overcome using the arrangement shown in Figure 3.14. Two 127 mm long sections of 38.1 mm inner diameter PVC pipes are mounted just above the free surface. The laser beam passes through the pipes. The pipes are in contact with the glass surface and hence keep the recording area of the glass clean.

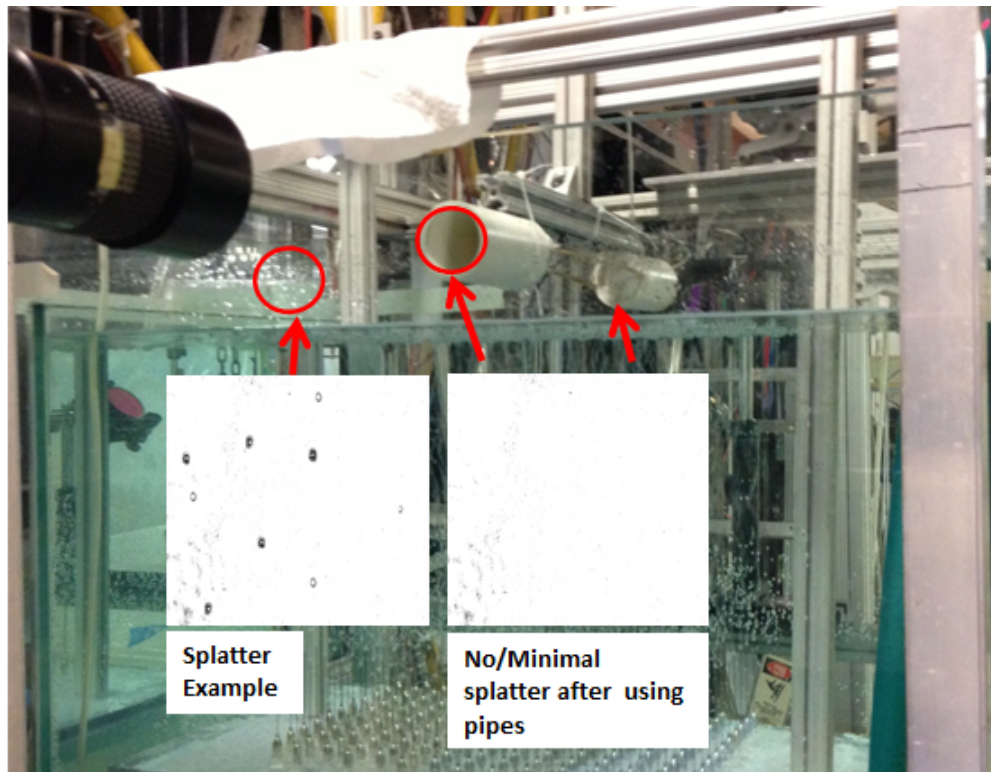


Figure 3.14: Drop splatter: Shadowgraph images showing splattered and clean regions.

To operate the measurement system, the camera and the laser need to be synced and triggered simultaneously. A triggering signal (TTL pulse) is sent by a function generator to a delay box using BNC cables. The delay box has two output signals, one goes to the external trigger of the camera while the other to the trigger input of the laser. This allows to time delay, the pulse from the function generator so that the light pulse occurs in each image when the aperture is open. The time delay between the two pulses is typically 5

ms. The camera is setup to record at 1000 *fps*. The frame rate is chosen to be as fast as possible, so that the tiny fast moving film drops may be seen. The camera memory hold 1282 frames and this restricts the recording time to 1.282 seconds. The need for a high spatial resolution (2560×1600) for data processing also restricts a higher frame rate.

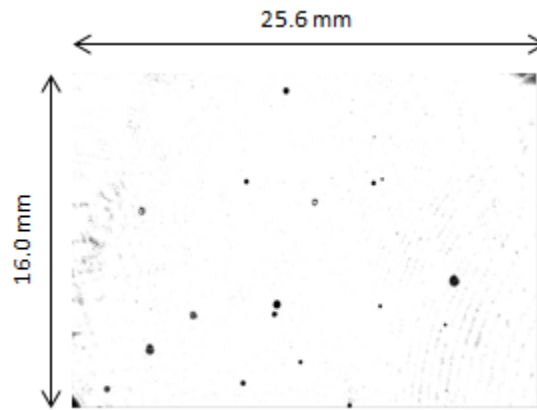


Figure 3.15: Sample shadowgraph image of droplets: 2560×1600 pixels.

The field of view of the shadowgraph image is $25.6 \text{ mm} \times 16 \text{ mm}$, which is the same as the size of the camera sensor. Since a 1:1 magnification is used, a resolution of $10 \mu\text{m}/\text{pixel}$ is achieved at the focal plane, at a distance of 482.6 mm from the lens (Figure 3.15). This is an important number when it comes to data processing as it restricts the size of the smallest drop that can be accurately measured using this system.

Chapter 4

Measurement Techniques

4.1 Bubble measurement

In this section, the image processing technique for estimating the bubble size is discussed. Measurements for the bubble are made when it is just below the free surface. In order to measure the bubbles, a calibration image is required (Figure 4.1). The field of view for the images is $62.7 \text{ mm} \times 31.3 \text{ mm}$. This corresponds to a magnification of $4.79 : 1$. The plane of recording is approximately 1.21 m from the lens. The apparent change in size of the bubble due to this magnification is not a concern since the calibration image of ruler is also at the same magnification. Hence, the true size of the bubble can be measured using this system. The calculated resolution is $24.5 \mu\text{m}/\text{pixel}$. The data is collected in the form of high speed movies. Discrete frames from these movies are selected and stored in a 8-bit .bmp file format. These images are then imported in to MATLAB.

The processing code fits an ellipse to the bubble in the least square sense. The

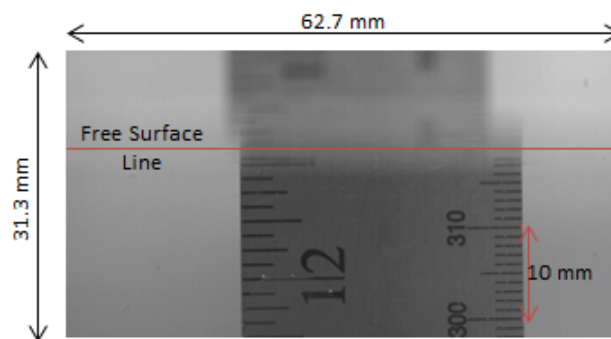


Figure 4.1: Bubble size calibration: Image of the ruler with the free surface meniscus indicated by the horizontal line. The camera resolution is 2560×1280 .

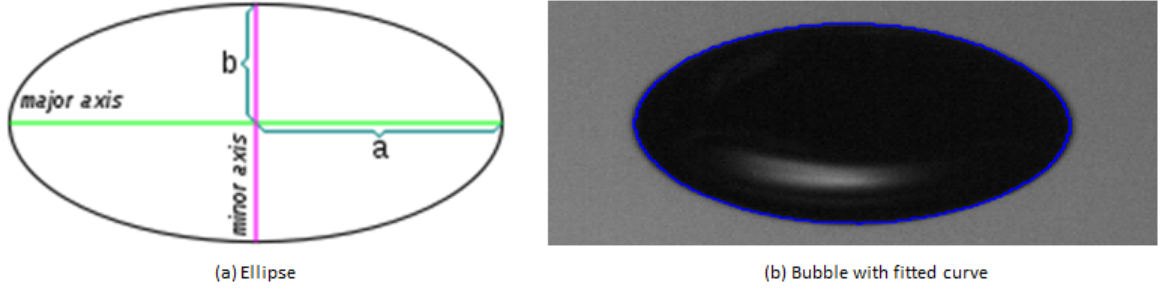


Figure 4.2: Oblate spheroid and bubble: Oblate spheroid is formed by rotating the ellipse about its minor axis.

bubble is basically assumed to be an oblate spheroid formed by rotating the ellipse about its minor axis (Figure 4.2). The code uses a boundary tracing function to detect the edge (perimeter) of the ellipse by using a set threshold for the gray level to distinguish between the background and the bubble. This is done more efficiently by inverting the black and white pixels (Figure 4.3). The general quadratic form of a curve is given by

$$\begin{aligned}
 ax^2 + 2bxy + cy^2 + 2dx + 2fy + g &= 0 \\
 2b'xy + c'y^2 + 2d'x + 2f'y + g' &= -x^2
 \end{aligned}
 \tag{4.1}$$

where $b' = b/a$, $c' = c/a$, $d' = d/a$, $f' = f/a$, $g' = g/a$.

This equation is then solved for the coefficients in a matrix form by passing the perimeter values for x & y as inputs. The measurements for the ellipse, semi-major axis and semi-minor axis are extracted. Based on these measurements, the volume of the oblate spheroid is calculated and converted to an equivalent spherical bubble volume with a diameter (d_{bubble}).

$$V_{oblate} = \frac{4}{3}\pi a^2 b = \frac{4}{3}\pi \left(\frac{d_{bubble}}{2}\right)^3 = V_{bubble}
 \tag{4.2}$$

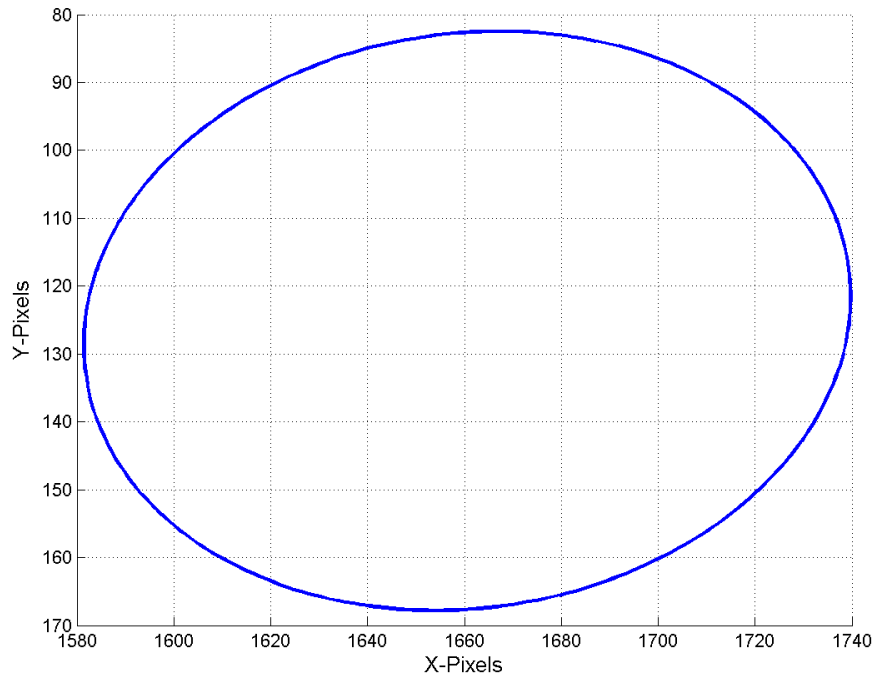


Figure 4.3: Pixel position of the ellipse fit to bubble perimeter on the image.

where $a = \text{semi-major axis}$, $b = \text{semi-minor axis}$ &

$d_{\text{bubble}} = \text{equivalent bubble diameter}$.

The measured bubble diameters for clean water at various air flow conditions can be seen in Figure 4.7. For the surfactant laden water, the bubbles are more spherical in shape (Figure 4.4). A least squares linear polynomial robust fit is applied to the data. The outliers are removed from the data-set by using standard deviation as a benchmark. It is important to note that the bubble diameters calculated are considered estimates because

the technique doesn't take in to account the sharpness(focus) of the bubbles based on the intensity. The only measure of focus is by human eye which results in the noisy nature of the data observed on the plots. The focusing issue also causes reduction in usable data which results in the fit not being very close to the data-set. Nevertheless, this technique does help in calculating a mean bubble diameter for an amount of air in the bubble-maker and the corresponding bubble production rate. It may be concluded that the bubbles diameters for surfactant solution is on an average smaller than that for clean water at the same bubble production rate. The results for the average diameter values and the bubble rate and the volumetric air flow-rate can be seen in Table 4.1 and Table4.2. The total bubble rate is calculated by studying the single needle and then multiplying the results with the number of needles on the bubble-maker.

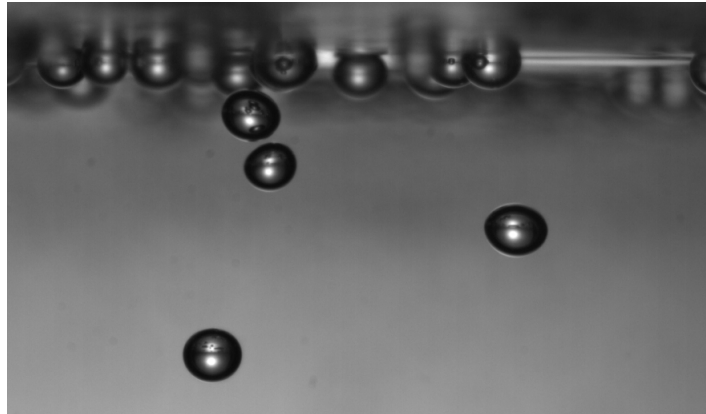


Figure 4.4: Bubble in surfactant solution: The bubbles appear to be more spherical in shape compared to clean water.

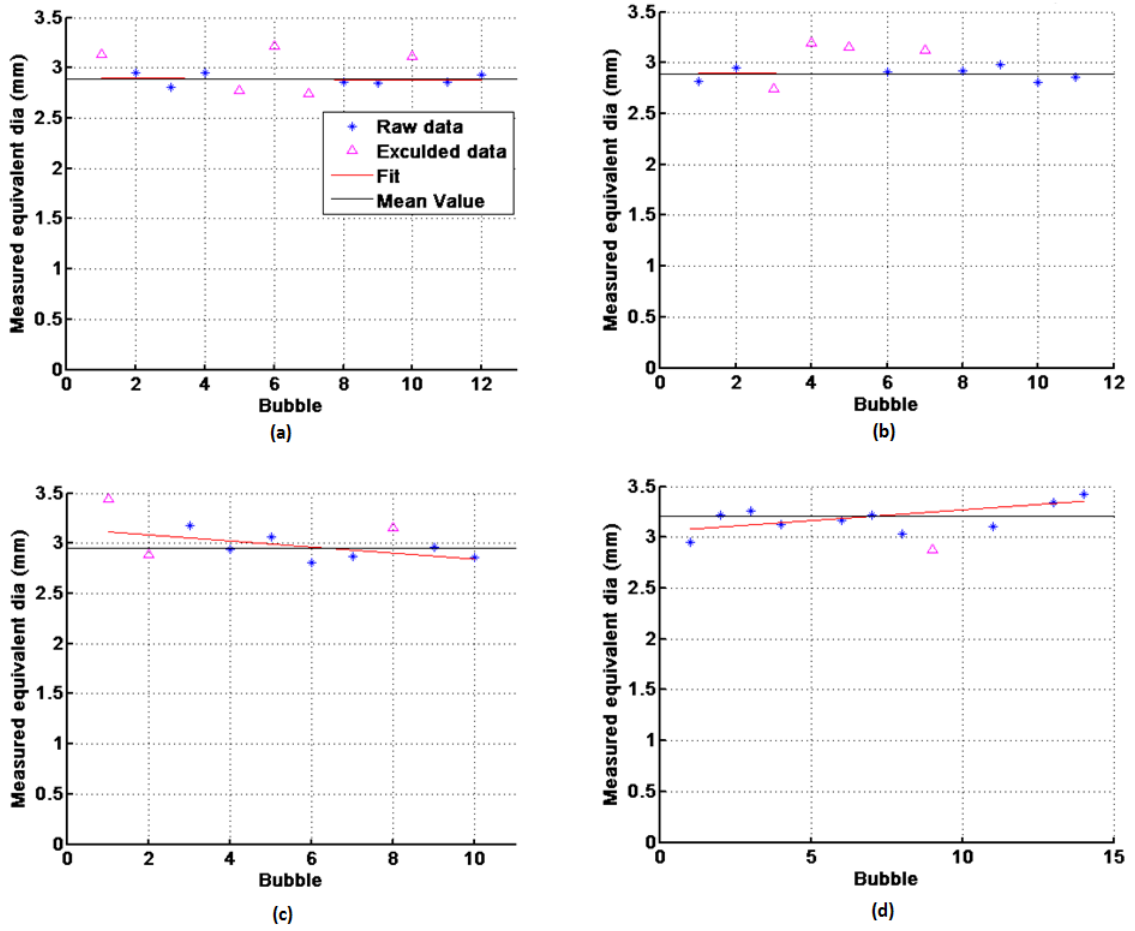


Figure 4.5: Bubble diameter variation for clean water: The mean value is indicated by the black line and the red line represents the fit for (a) 1 inch, (b) 2 inches, (c) 3 inches, (d) 4 inches of air heights in the bubble-maker. The noisy nature is attributed to the lack of focus(sharpness)

Air Height (inches) ^a	Clean Water					
	Bubbles/second(1 needle)	Bubbles/second(180 needles)	Equivalent spherical diameter (mm)	Major-axis (mm)	Minor-axis (mm)	Volumetric air flowrate (Liters/min)
1	24	4320	2.885	3.594	1.861	3.260
2	30	5400	2.891	3.593	1.875	4.099
3	30	5400	2.955	3.672	1.926	4.376
4	40	7200	3.210	4.050	2.049	7.483
5	42	7560	3.301 ^b	-	-	8.543

Table 4.1: Bubble production data for clean water

^aThe air height is reported in English units (inches) for simplicity

^bEstimation: Refer Appendix A

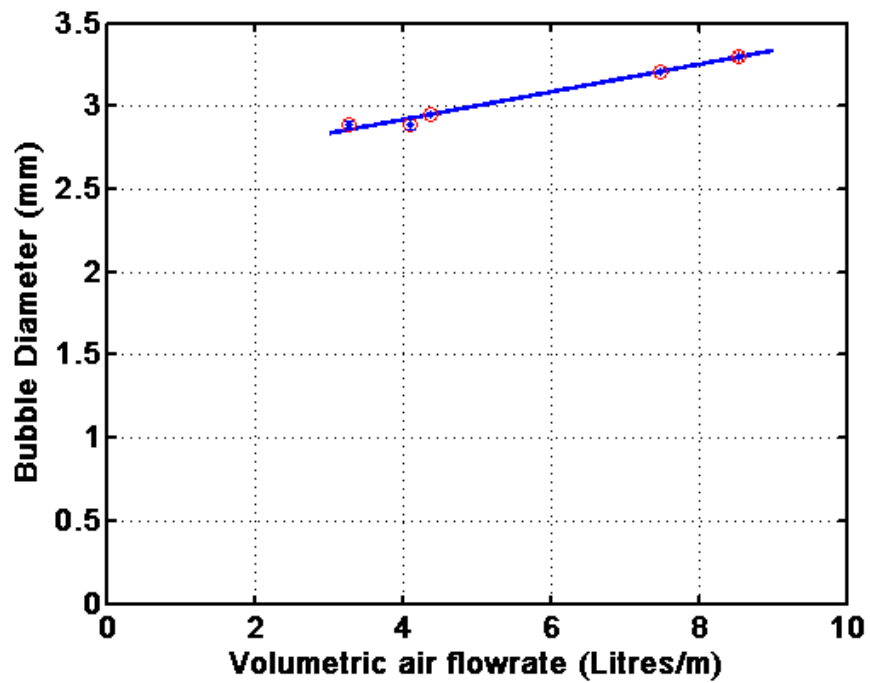


Figure 4.6: Bubble diameter versus volumetric air flow rate for clean water cases: Data points are indicated by the red circles and blue line is the linear fit.

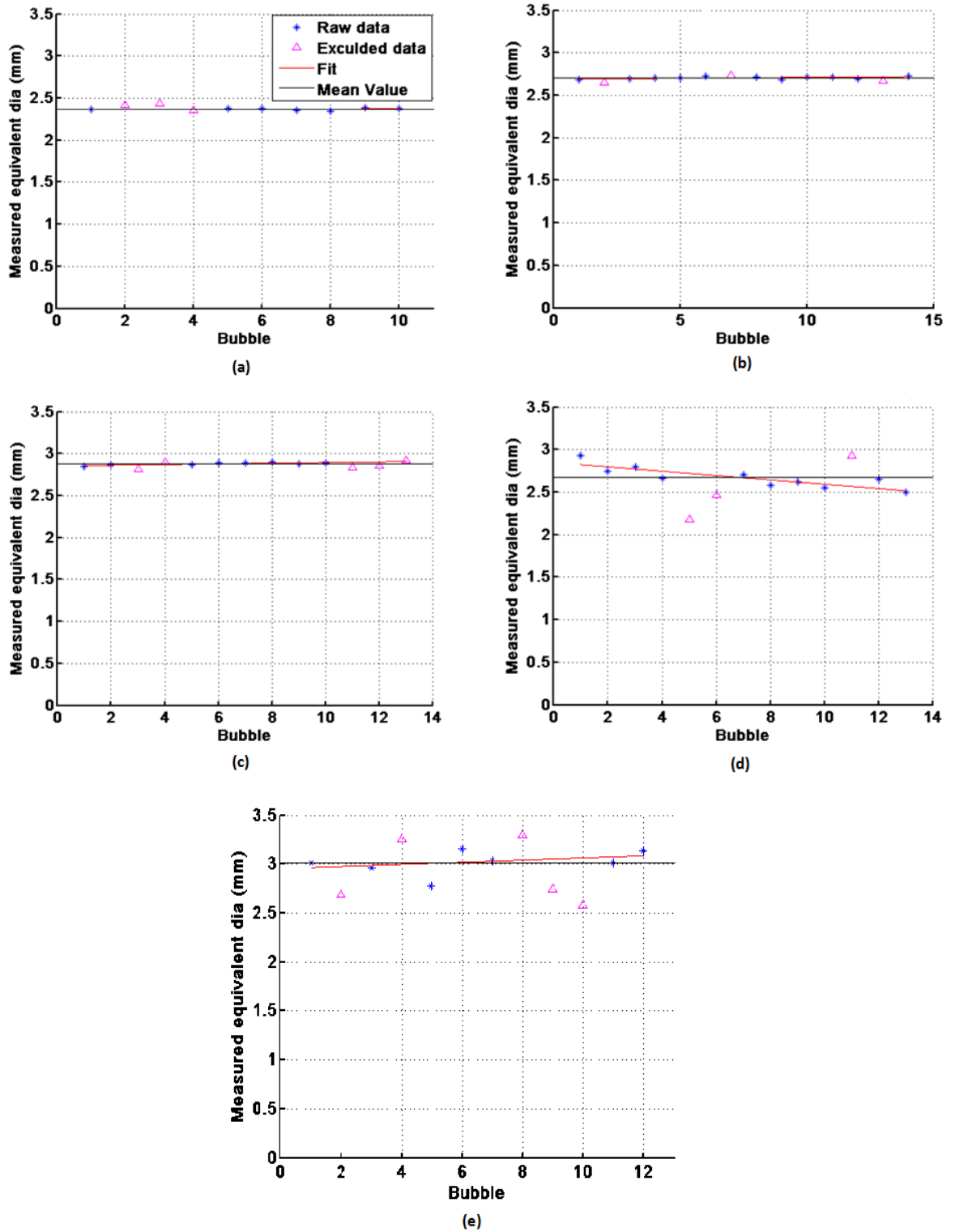


Figure 4.7: Bubble diameter variation for surfactant solution: The mean value is indicated by the black line and red line represents the fit for (a) 1 inch, (b) 2 inches, (c) 3 inches, (d) 4 inches, (e) 5 inches of air heights in the bubble-maker

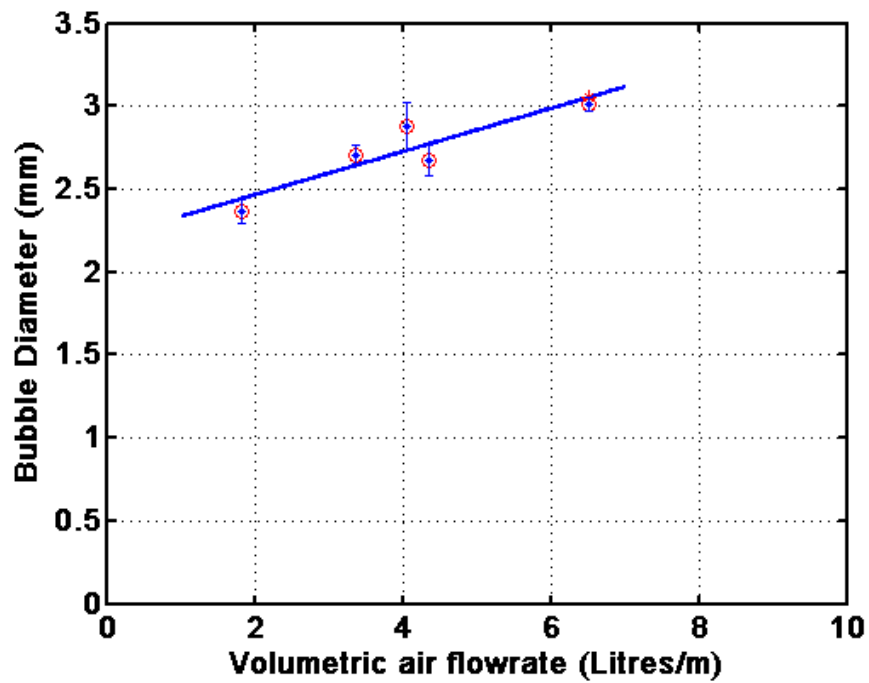


Figure 4.8: Bubble diameter versus volumetric air flow rate for surfactant solution cases: Data points are indicated by the red circles and blue line is the linear fit.

Air Height (inches) ^a	Bubbles/second(1 needle)	Bubbles/second(180 needles)	Clean Water				
			Equivalent spherical diameter (mm)	Major-axis (mm)	Minor-axis (mm)	Volumetric air flowrate (Liters/min)	
1	24	4320	2.369	2.502	2.125	1.804	
2	30	5400	2.706	2.878	2.393	3.363	
3	30	5400	2.879	3.045	2.575	4.049	
4	40	7200	2.676	2.833	2.389	4.333	
5	42	7560	3.014	3.220	2.642	6.502	

Table 4.2: Bubble production data for surfactant solution

^aThe air height is reported in English units (inches) for simplicity

From the data shown in Tables 4.1 and 4.2 and plots in Figure 4.6 and Figure 4.8, it is inferred that the volumetric air flow rate increases linearly as the height of air in the bubble-maker is increased. The assumption made in this experiment is that the clean and surfactant solution have the same bubble production rate (Bubbles/sec column in the Tables). Two anomalies are observed. Firstly, the bubble production rate is the same (5400 bubbles/sec) for 2 and 3 inches of air heights in the bubble-maker. This is most likely due to the bubble-structures coalescing (observed in the high speed movies) at the tip of the needle right after they come out. As a result, there is no change in the bubbles/sec data but there is a change in the bubble diameter. The second anomaly is the measured equivalent spherical diameter of 2.676 mm for the surfactant condition case with 4 inch air height in the bubble-maker 4.2, which is less than the diameter measured for the 3 inch case. The reason could be a combination of two things; first, the measured bubbles could be marginally outside the focal plane of camera which causes a error in the detection of the edges of the bubble by the Matlab code and second, the bubble flow behavior near the needle maybe affecting the size of the bubble.

4.2 Shadowgraph instrument calibration

To accurately measure the droplets, it is important to be able to quantify the measure of focus of the drop. When a drop is outside of the focal plane, its measured diameter will be different from the actual because the edges will be fuzzy. In this section, we discuss a calibration technique to correct this fuzziness and also discuss the processing routine and the determination of the measurement volume.

The idea behind calibration is imaging circular targets of known diameter in and out-of-focal plane. The apparent diameter in the image is computed at known distances from the focal plane and the results are compared with the actual diameter. The calibration setup can be seen in Figure 4.9. The target used is a Patterson Globe Microscope Reticle. It is basically a transparent glass slide with 14 opaque black dots etched on it. The dot diameters vary from 30 μm to 3000 μm . The target is attached to a motorized linear traverser system (NEAT 310M Programmable Stepping Motor Controller) and placed in the span-wise center of the tank in the camera's field of view.¹ The target is moved until it is sharply in focus. This position of the target on the traverser is noted as the focal plane. The target is then moved in finite steps both, towards and away from the camera using the traverser, which is controlled by a Labview code. At each step, an image of the target is taken (Figure 4.10). The initial step-size is as small as 0.005 mm to get a large data set for the smallest dots which are in focus only for a very short distance from the focal plane. As the target moves out of the focal plane, the sharp black dots fade to more of a grayish color with fuzzy edges. The step-size is increased when the smallest dots can no longer be imaged. Fresnel intensity patterns are also observed in the images. Sample calibration images of the target in and out of the focal plane can be seen in Figure 4.10.

¹The words 'reticle' and 'target' are used interchangeably.

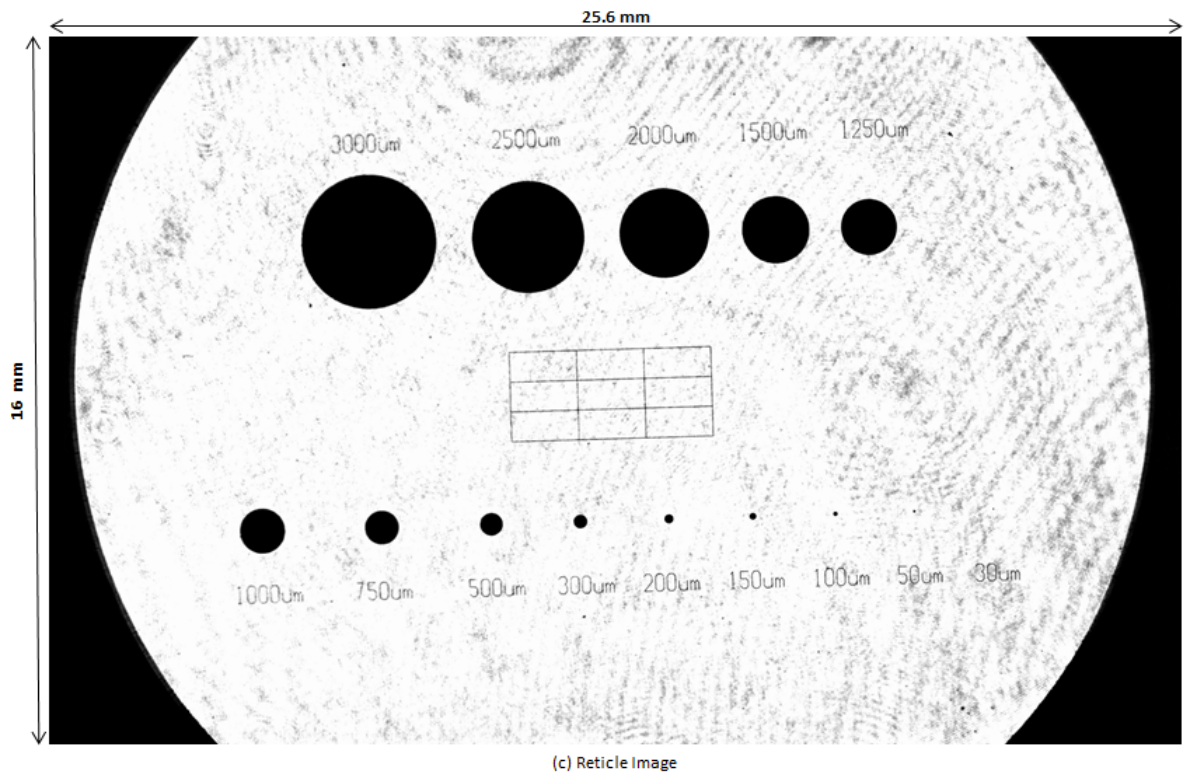
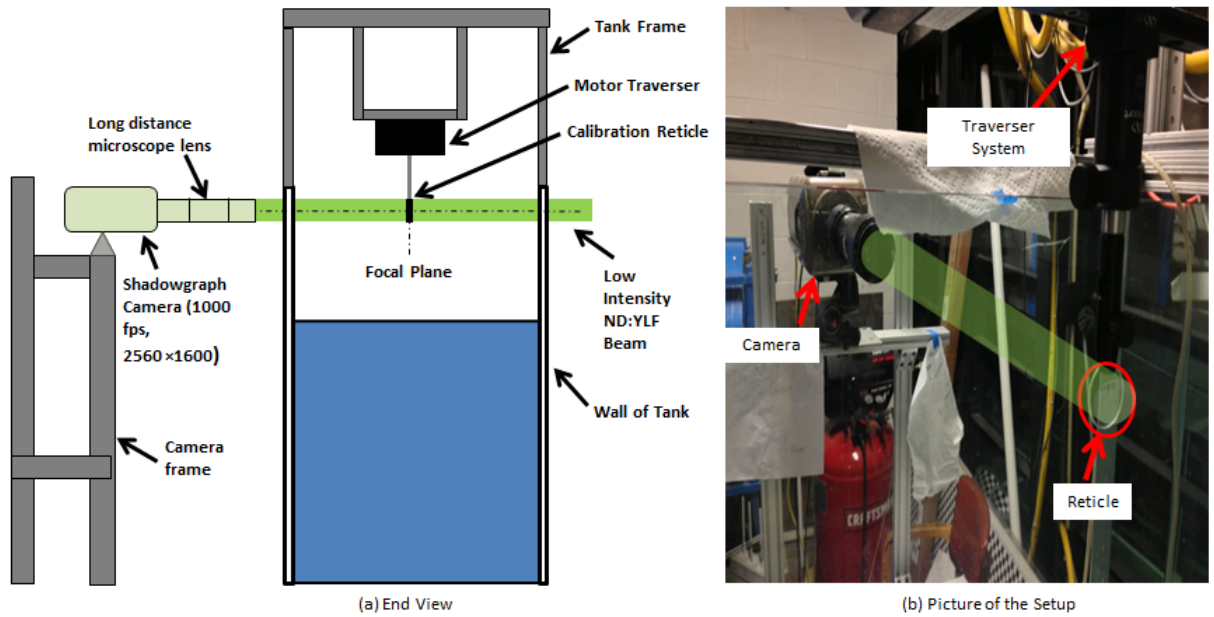


Figure 4.9: Shadowgraph instrument calibration: (a) Schematic for depth of field calibration, (b) Picture of the setup, (c) Image of the reticle at focal plane with resolution 2560×1600 . Dot diameter range from $3000 \mu\text{m}$ to $30 \mu\text{m}$.

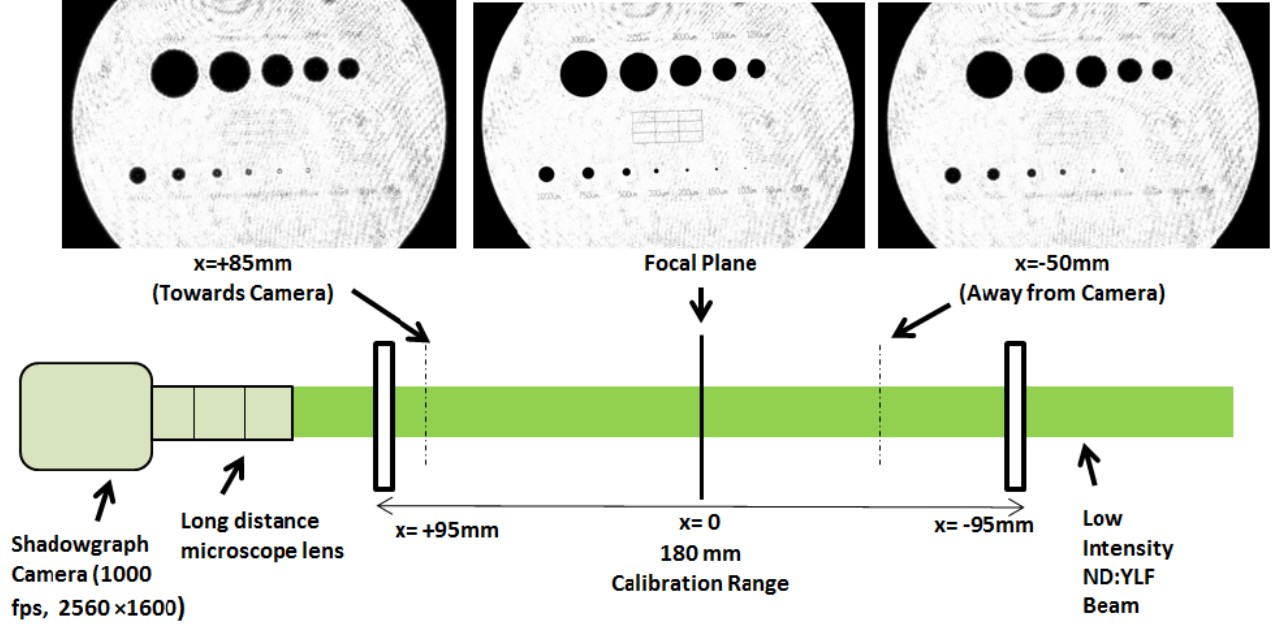


Figure 4.10: Calibration images of reticle at various distances from focal plane: Notice the fuzzy edges as the distance from focal plane increases.

The diameter and the intensity of the dots are determined using an axisymmetric two-dimensional hyperbolic tangent function fit to the image intensity pattern. The function is of the form

$$F = A_0(1 - \tanh(A_1 (\sqrt{(x - x_0)^2 + (y - y_0)^2}) - A_2)) + A_3 \quad (4.3)$$

The position parameters x_0 , y_0 and parameters A_n are determined by a non-linear least squares method to fit the image intensity data. The fitting error minimization technique is used to obtain a best fit to the image data. The A_n parameters are:

$$A_0 = \text{Intensity of the dot} \quad A_1 = \text{Sharpness} \quad A_2 = \text{Radius}$$

$$A_3 = \text{Intensity of the background}$$

The average intensity of the background (A_3) is calculated by excluding the black areas in the image. A sample image showing the areas used to determine the background

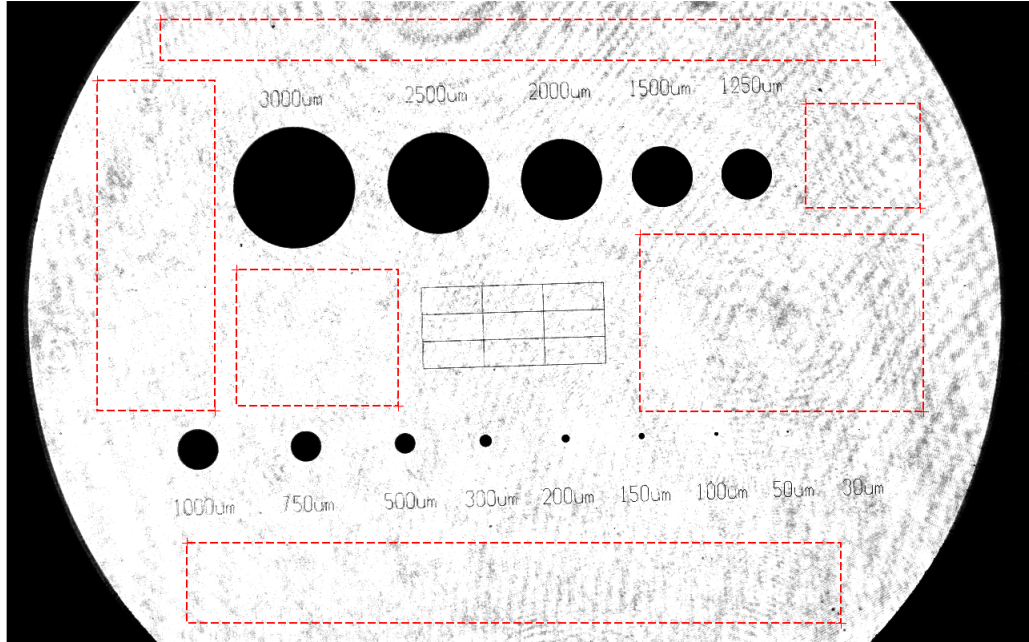


Figure 4.11: Average background intensity calculated from the areas enclosed by the rectangles. intensity can be seen in Figure 4.11. This average value varies marginally from shot to shot and it lies in a range of 3850 to 4000 which is considered stable. These image intensity values are the non-inverted values, hence the larger values represent a whiter background. Later on, for processing, the image intensity is inverted.

The plot for the average inverted intensity of each dot versus the distance from the focal plane is shown in Figure 4.12. The average intensity is given by $4095 - \tilde{I}$ where \tilde{I} is the gray level (intensity) ranging from 0 to 4095 for a 12-bit depth .TIFF image. The average flipped intensities for all the dots decrease as the reticle is moved out of the focal plane in either direction. The slope is steeper for smaller dots. This means that that smaller dots become blurred faster than the bigger dots. Figure 4.13 shows the computed normalized diameters $\frac{D_m}{D_f}$ versus distance from the focal plane, where D_m is the computed diameter at a distance from the focal plane and D_f is the computed diameter at the focal plane. Hence at the focal plane, this ratio is 1. Its is observed that as the reticle is moved

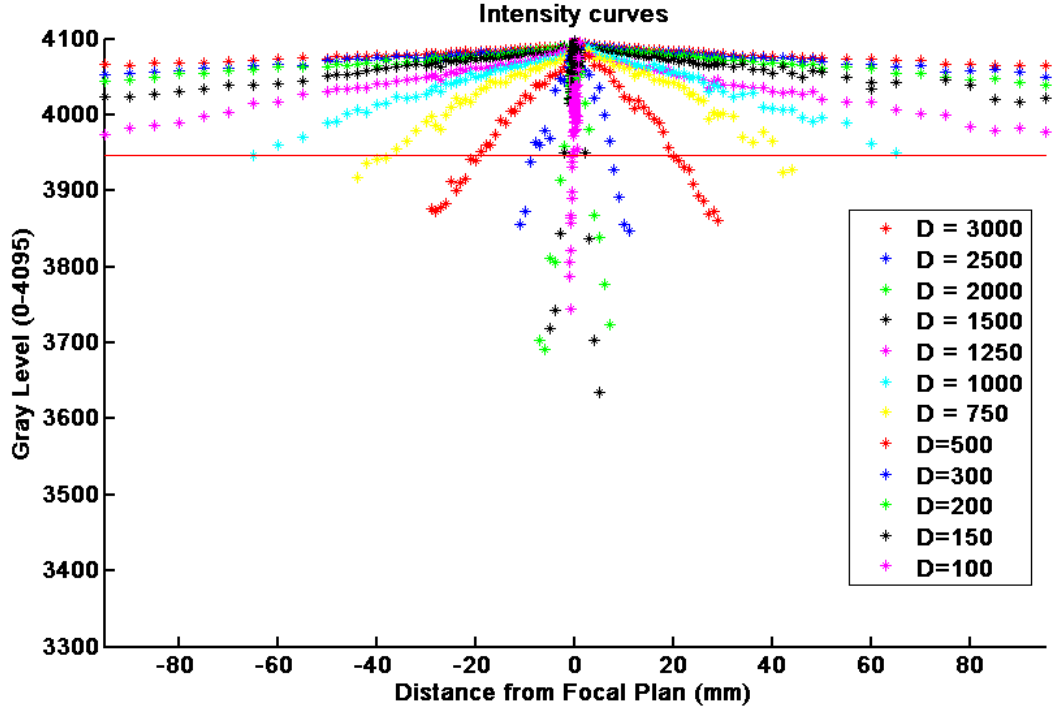


Figure 4.12: Average intensity of the images of the various dots on a Patterson globe reticle as a function of distance of the reticle from the focal plane of the lens. The horizontal red line represents an average intensity cutoff threshold of 3946 which restricts the diameter measurement error to 7%.

out of focal plane, $\frac{D_m}{D_f}$ increases for all except the $100\mu m$ dot. This is most likely due to skewness of the reticle relative to the line of sight of the camera. For the smaller dots, the ratio increases more rapidly than the bigger dots.

From the two plots, it is inferred that the maximum error increases with decreasing intensity threshold. After careful analysis of the intensity plots, the limiting value of 3946 is chosen for the average intensity. This average intensity cutoff value restricts the maximum error in diameter measurement to 7%. All the drops images with average intensity less than 3946 are rejected as the error will be greater than 7%. The horizontal lines in the Figure 4.13 and Figure 4.12 represent the cutoff threshold for the diameter (7% error) and average intensity (3946) respectively.

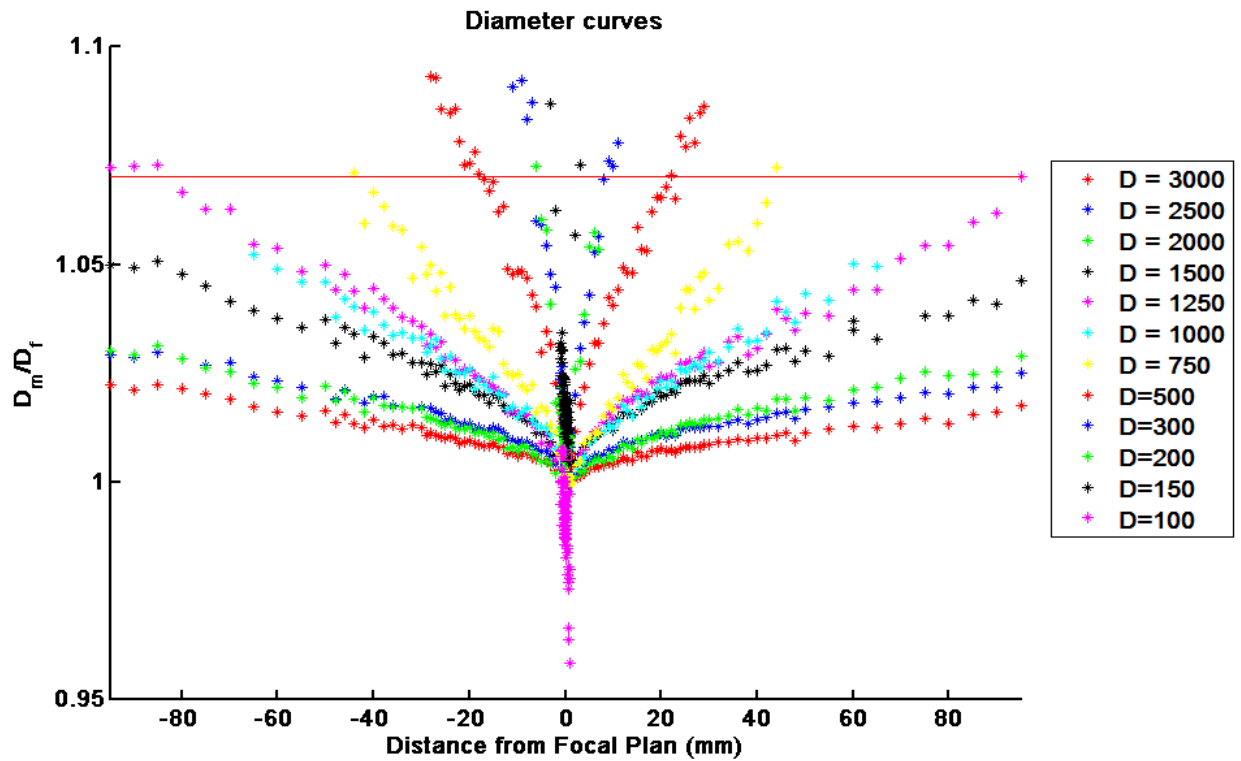


Figure 4.13: Normalized diameter of the images of the dots on the Patterson globe reticle as a function of the distance of the reticle from the focal plane. For all the data points below the horizontal red line (intensity value of 3946), the error in the diameter measurement was less than 7%.

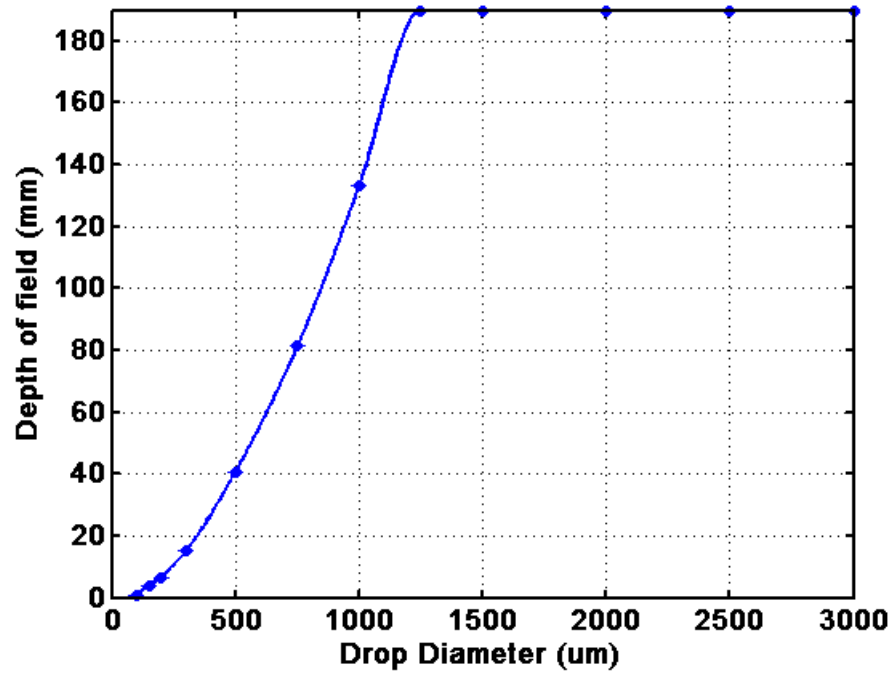


Figure 4.14: Depth of field (DOF) versus drop diameter.

It is observed from Figure 4.12 that range of distance from the focal plane for which the dot intensity values are above the limiting threshold increases with increasing dot diameter. This range is called the depth of field (DOF). A plot of depth of field versus dot (drop) diameter can be seen in Figure 4.5. The measurement volume for each dot size can be calculated by using the depth of field and the field of view for the camera.

$$\text{Measurement Volume} = \text{DOF} \times \text{Field of view} \quad (4.4)$$

4.3 Shadowgraph droplet measurement

A sample shadowgraph image used for drop measurement is shown in Figure 4.16. The black dots correspond to the drops. Such images are extracted from the shadowgraph movie file and processed using the Matlab two-dimensional function fit program. The drops which are above the threshold intensity can be seen with red circles and the ones with blue circles are below the threshold and hence neglected. To extract these images, the movies are visually inspected and only the frames in which there are drops that are going up or across the screen are selected. Drops which are observed moving down in the movie are neglected. This is done to ensure that no drop is measured twice. Based on observation, almost all of the drop images are circular in shape indicating that the drops themselves are spherical in shape. The concentric circles seen in the background are noted as the interference patterns due to the coherent laser light.

In Figure 4.17, the plots for measured intensity of a drop close to the focal plane and the non-linear surface fit can be seen. The value of 4095 corresponds to completely black (drop) while 0 represents white (background). The sides of the plot are very steep and the top is a flat-plateau like form. When the fit and raw data are superimposed, there is marginal disagreement. Such a result indicated that the drop is sharply in focus. In Figure 4.18, a similar plot is shown for a drop with fuzzy edge. The edge of the fit in this case aren't as steep as in Figure 4.17 and the average intensity is also lower. This indicates that the drop is not in focus. Since the drop diameter and intensity are computed using the fit given in equation 4.3, these plots are important reference points and validate the applicability of the fit at varying focal depths and drop diameters.

The measurement volume for each droplet diameter is the field of view of the camera/lens time the depth of field for that droplet diameter. For raw uncorrected measure-

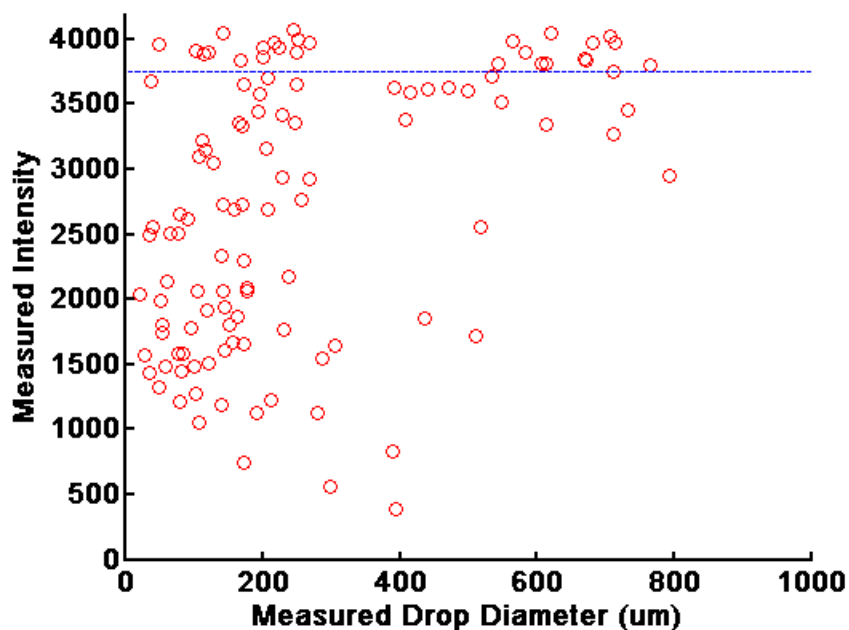


Figure 4.15: Intensity versus Drop Diameter: Data from 1 run with 5 inches of air in the bubble-maker for clean water. Drops which are above the horizontal line indicate intensity >3946 and everything below the line has intensity <3946 .

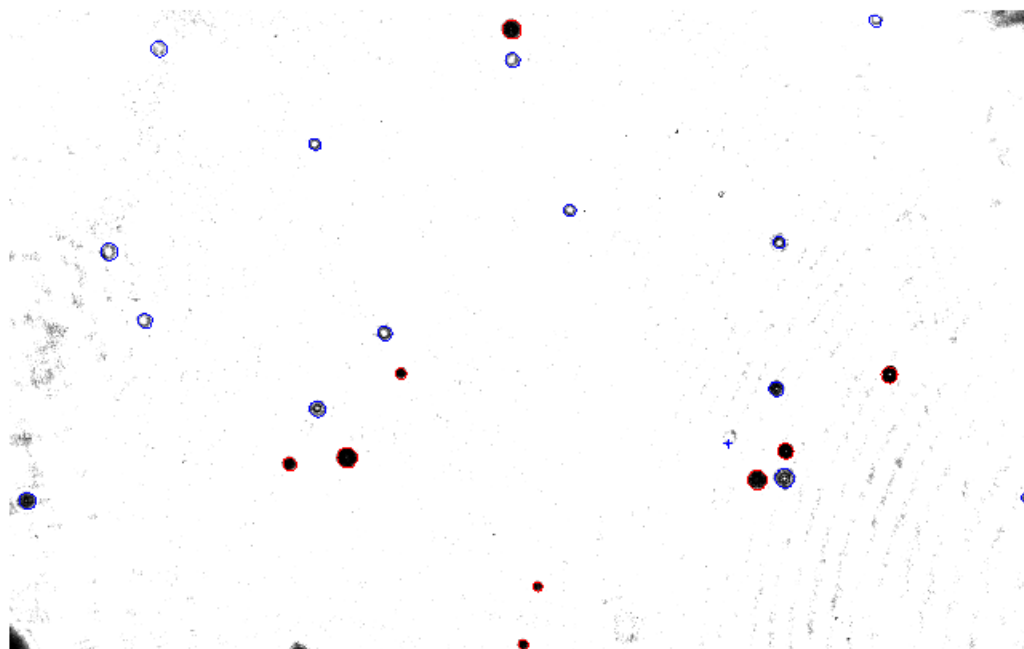


Figure 4.16: Sample image used for drop processing: Useful data is in red circles with drop intensity >3946 and discarded drops are in blue with intensity <3946 .

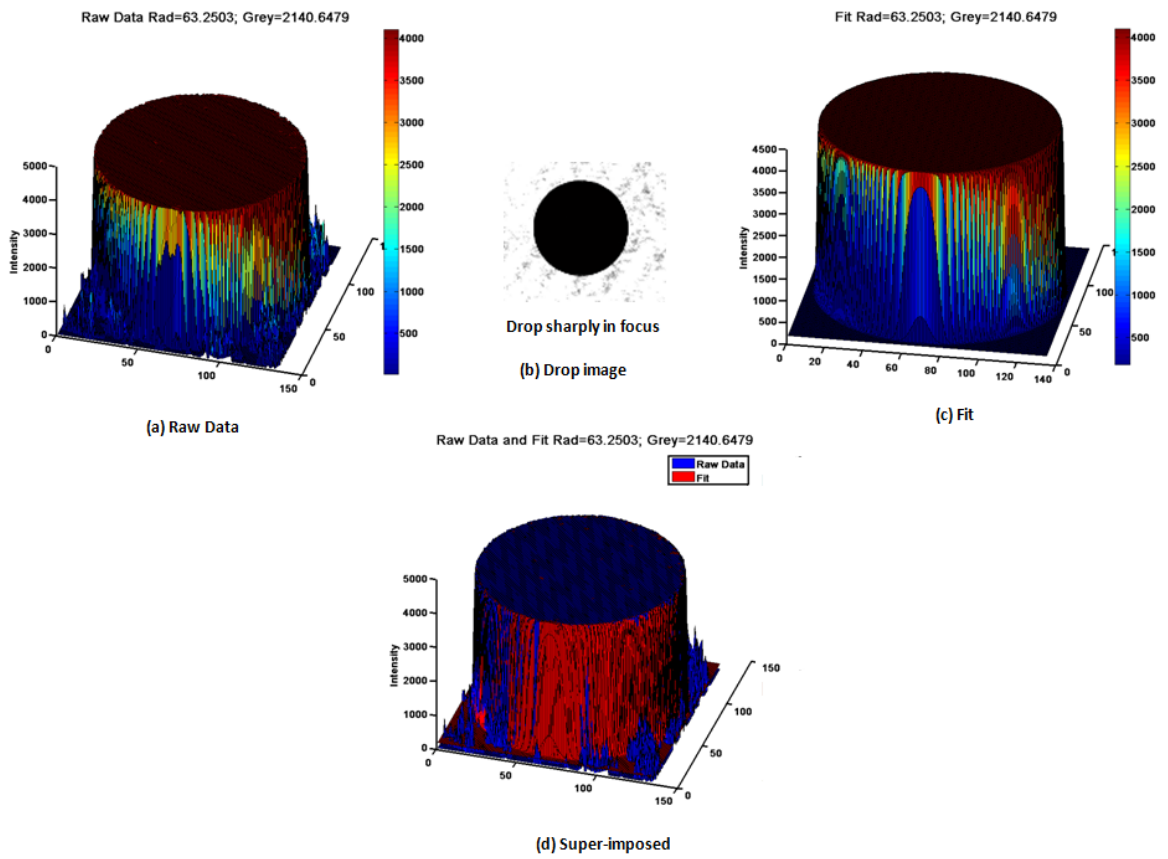


Figure 4.17: Intensity graph of a sample drop positioned close to the focal plane: (a) Raw data from the image, (b) Drop image (c) Fitting function, (d) Data and fit super-imposed.

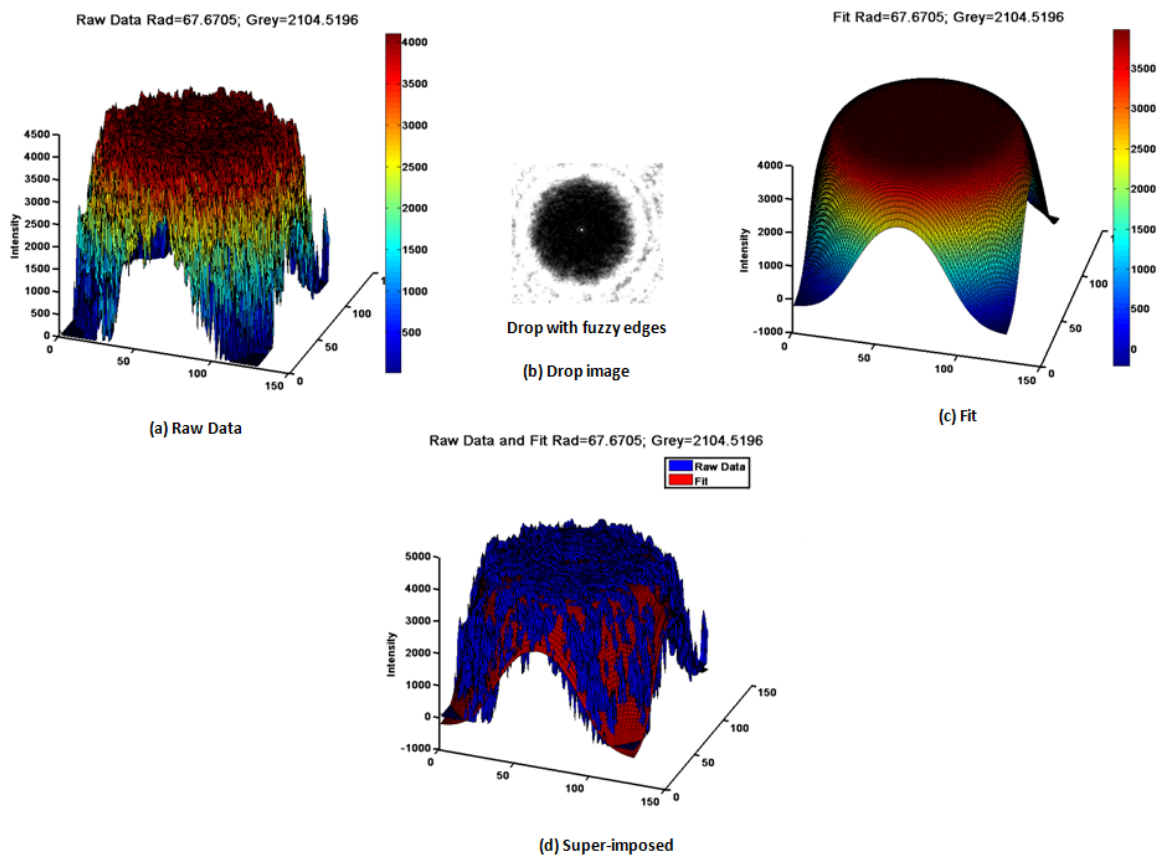


Figure 4.18: Intensity graph of a sample drop away from the focal plane: (a) Raw data from the image, (b) Drop image (c) Fitting function, (d) Data and fit super-imposed.

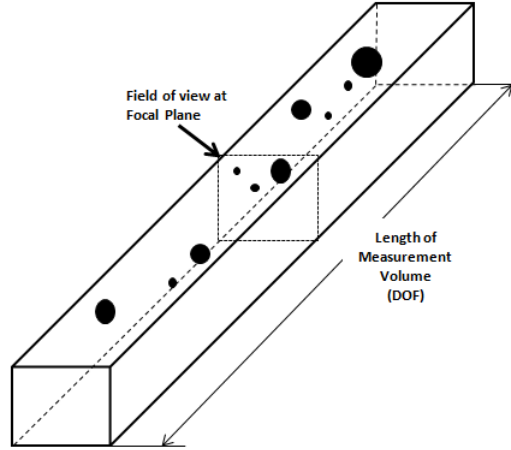


Figure 4.19: Measurement Volume

ments, the measurement volume is given by equation 4.4. This volume varies with the drop diameter as the DOF changes (Figure 4.19). The number of droplets N_i measured for a specific diameter d_i are adjusted by the depth-of-field calibration in order to determine the adjusted number of droplets $N_{adj}(d_i)$ in a common measurement volume:

$$N_{adj}(d_i) = N_i(d_i) \times n_i \quad (4.5)$$

where $n_i = \frac{A_v \times W_t}{A_v \times z_i}$, A_v = Field of view of the camera, W_t = Depth of field for the largest drop = 190mm for this experiment, z_i = Depth of field for droplet d_i .

4.4 Experimental test matrix

In this experiment, the optical shadowgraph technique is employed to measure the drop distribution from bubbles rising and popping at the free surface. Measurements are made for two different water surface conditions, clean water and water with a 0.4% v/v solution of Triton X-100 surfactant. A continuous bubble field is created with the help of the bubble-maker. Five different bubble sizes and bubble production rates are studied for each water condition. The bubble size measurements discussed in section 4.1 are made for the two different water conditions and for 1 to 5 inches of air in increments of 1 inch in the bubble-maker. The five heights of the air in the bubble-maker result in the five different bubble size/ bubble production rate combinations which are used as experimental conditions for the drop measurements. The experimental conditions are summarized in Table 4.3. The different conditions are labeled “Case 1” through “Case 5” with the number always indicating the height of air in inches in the bubble-maker. The Cases will be used in conjunction with the water condition i.e. clean water or surfactant solution to reference the experimental condition while stating the results.

Case	Inches of Air	Bubbles/second(180 needles)	Mean diameter of the bursting bubble (mm)	
			Clean	Surfactant
Case 1	1	4320	2.885	2.369
Case 2	2	5400	2.891	2.706
Case 3	3	5400	2.955	2.879
Case 4	4	7200	3.210	2.676
Case 5	5	7560	3.301 ^a	3.014

Table 4.3: Experimental test matrix indicating the bubbles production rates and bubble sizes for clean water and surfactant solution.

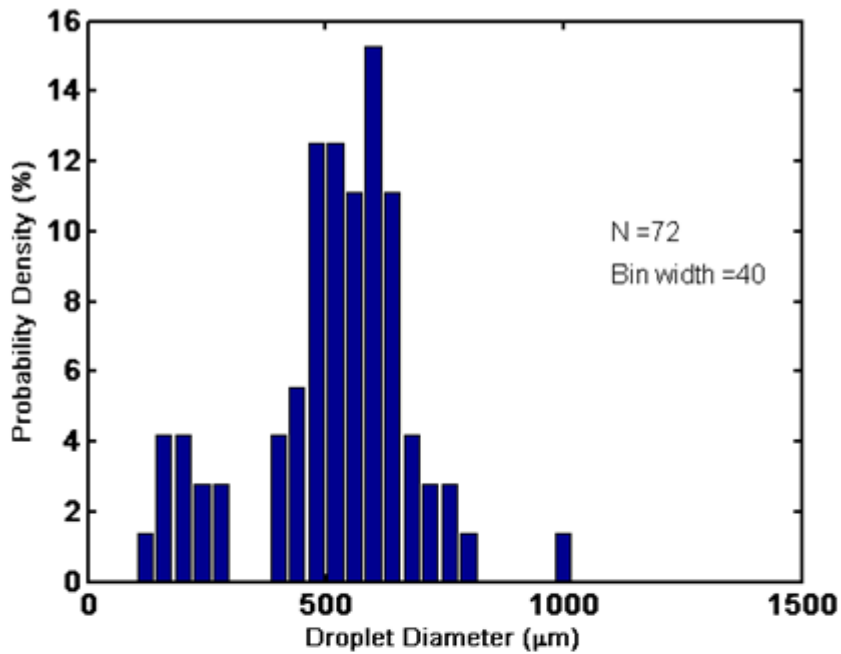
^aEstimation: Refer Appendix [A](#)

Chapter 5

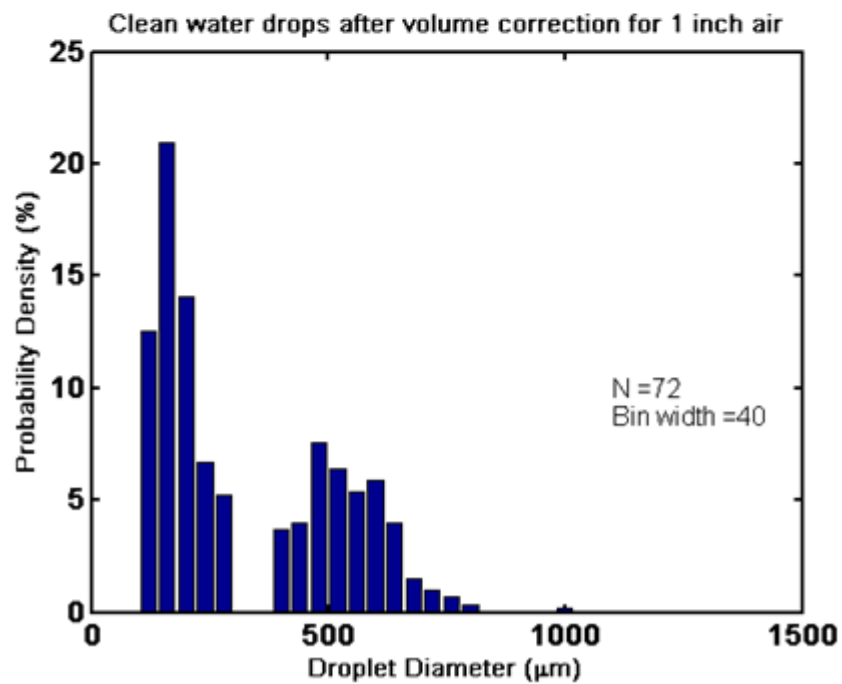
Results

5.1 Drop distributions

The raw and the depth of field calibrated distribution of droplets diameters averaged over nine runs for each bubble production rate for clean water can be seen in Figure 5.1 to Figure 5.5. Figures 5.1(a) to 5.5(a) show the drops directly measured from the images to within 7% error based on the diameter (Figure 4.13) and intensity (Figure 4.12) calibration curves. In these plots, the measurement volume is equal to field of view times the depth of field corresponding to that drop diameter which is found using Figure 4.5. This causes the change in the measurement volume based on the measured drop diameter. To obtain the drop distribution for a common measurement volume for all drop sizes, the data is then corrected using the depth of field calibration given by equation 4.5. This gives the adjusted number of drops in a measurement volume common to all the drop sizes. From the depth of field curve in Figure 4.5, it is inferred that the probability density distribution for the smaller drops will increase in comparison to the larger drops due to this volume correction. For the clean water data represented in Figure 5.1 through Figure 5.5, it can be noticed that for almost all the cases there are two distinct peaks, i.e. bimodal in nature with two sizes dominating. *Spiel* [21] observed similar bimodality for drops measured after the top jet drop measured from single bursting bubbles. For that study, the bubble size ranged from 698 – 2958 μm in diameter and study was conducted in fresh water. In this thesis, the bubble sizes range from 2885 – 3210 μm for clean water. The data shows one

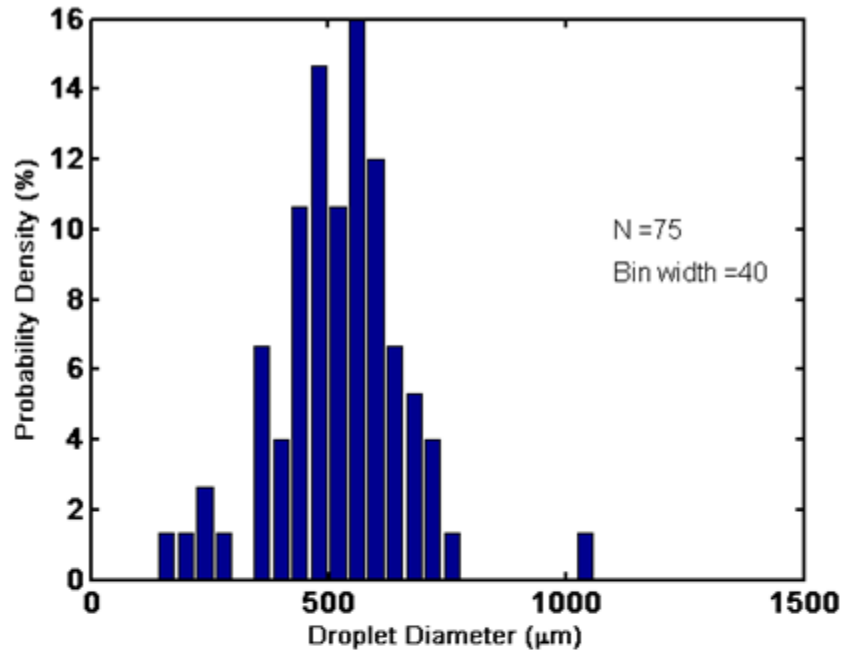


(a)

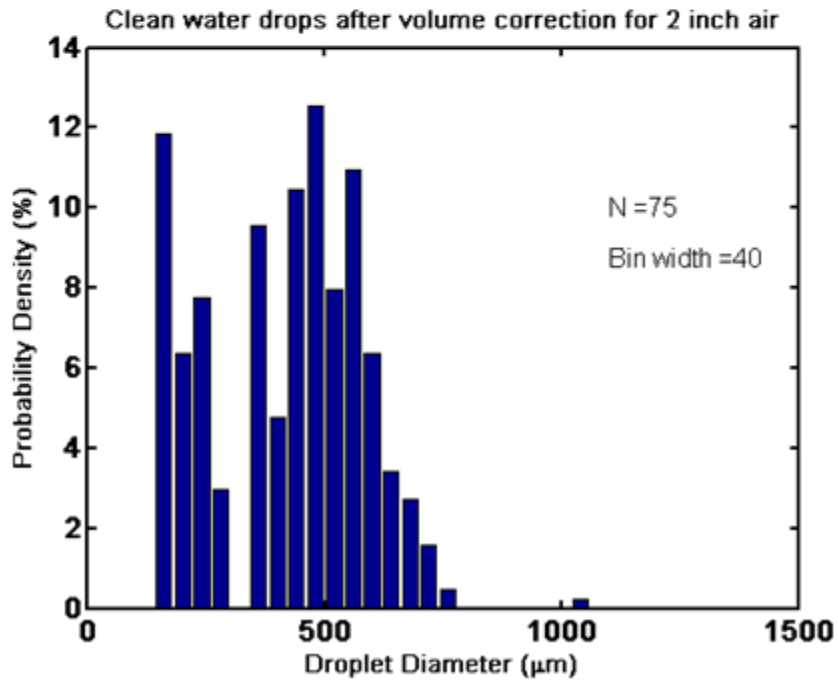


(b)

Figure 5.1: (a) Directly measured and (b) Depth of field corrected drop distribution for clean water Case 1 corresponding to bubble diameter of 2.885 mm. Bimodal peaks observed at 160 μm and 480 μm

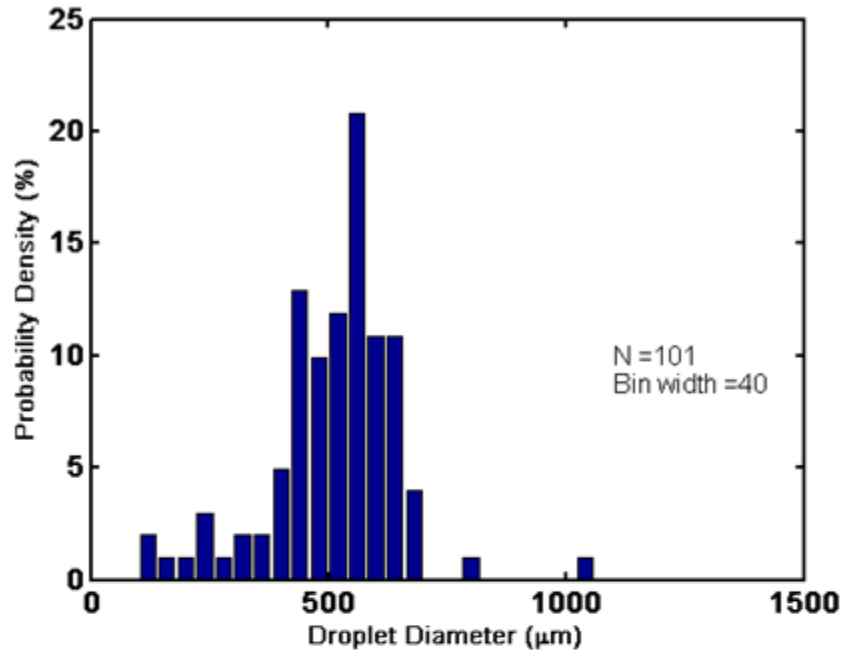


(a)

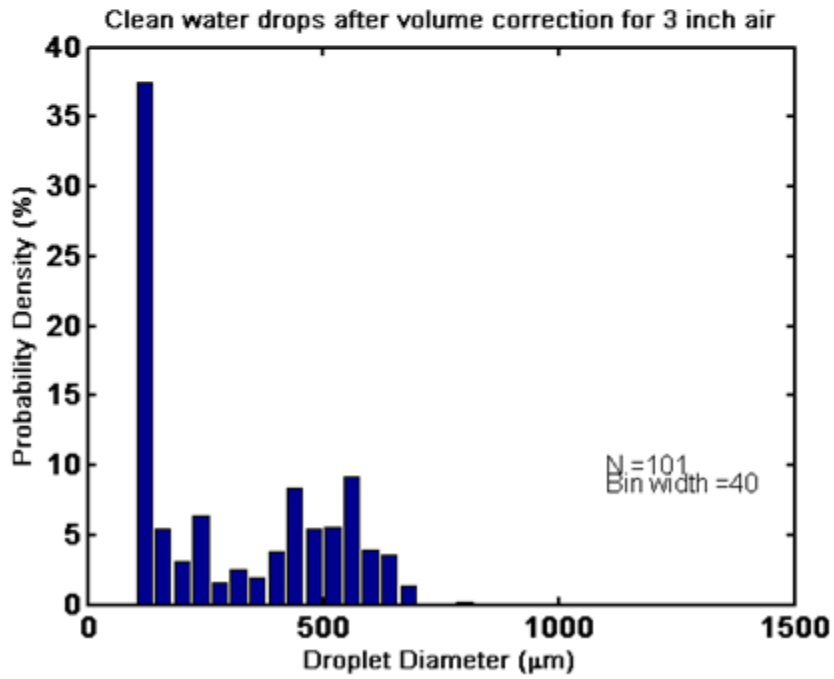


(b)

Figure 5.2: (a) Directly measured and (b) Depth of field corrected drop distribution for clean water Case 2 corresponding to bubble diameter of 2.891 mm. Bimodal peaks observed at 160 μm and 480 μm

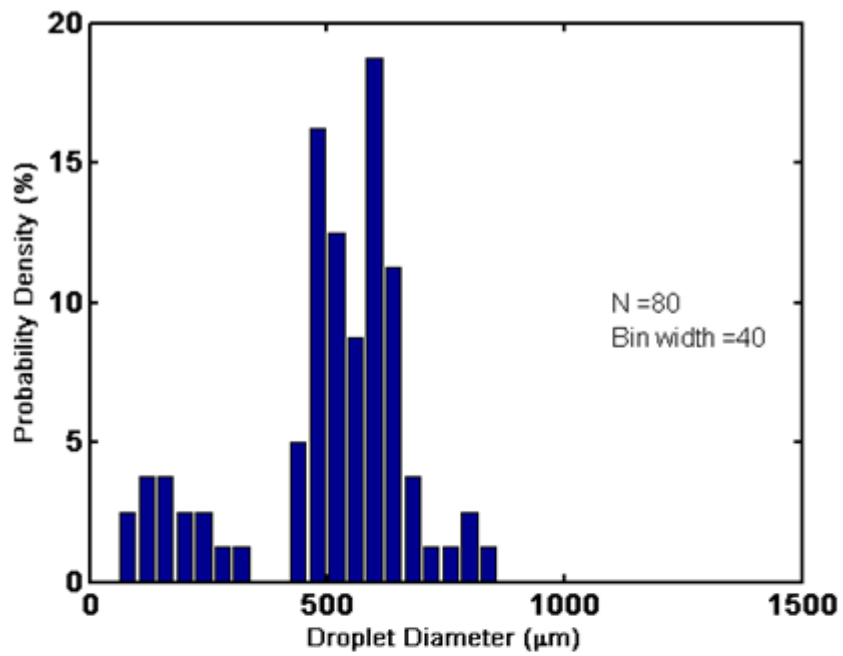


(a)

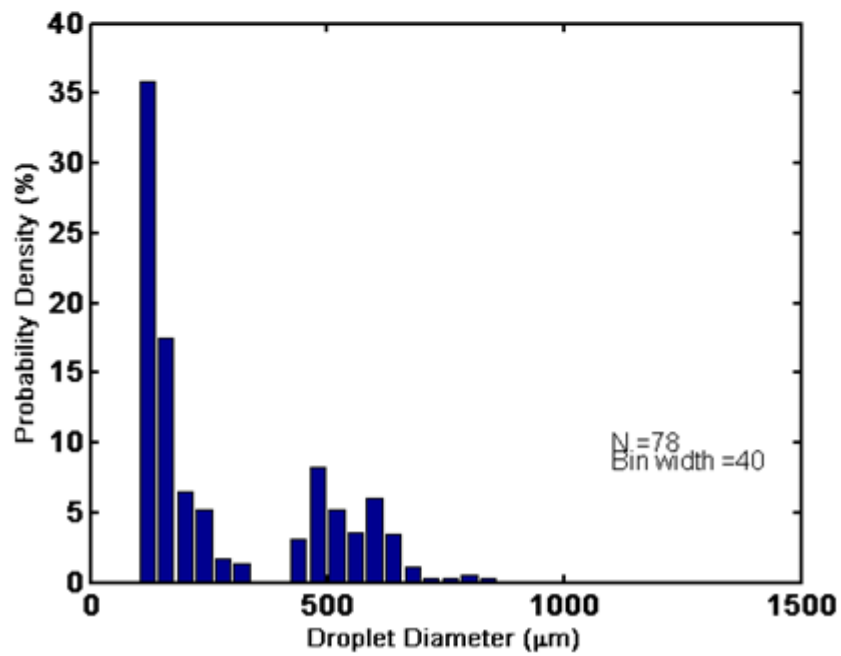


(b)

Figure 5.3: (a) Directly measured and (b) Depth of field corrected drop distribution for clean water Case 3 corresponding to bubble diameter of 2.955 mm. Bimodal peaks observed at 120 μm and 560 μm



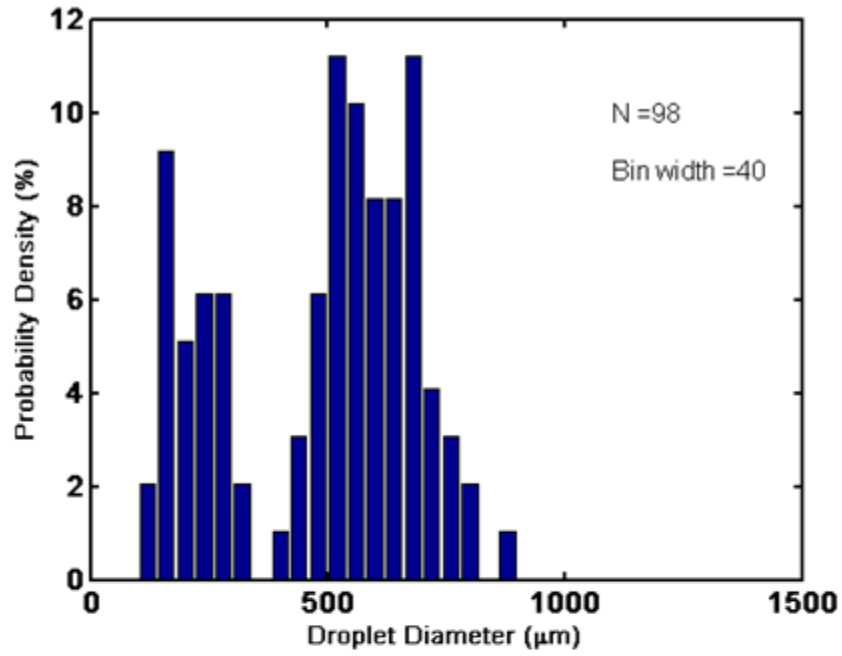
(a)



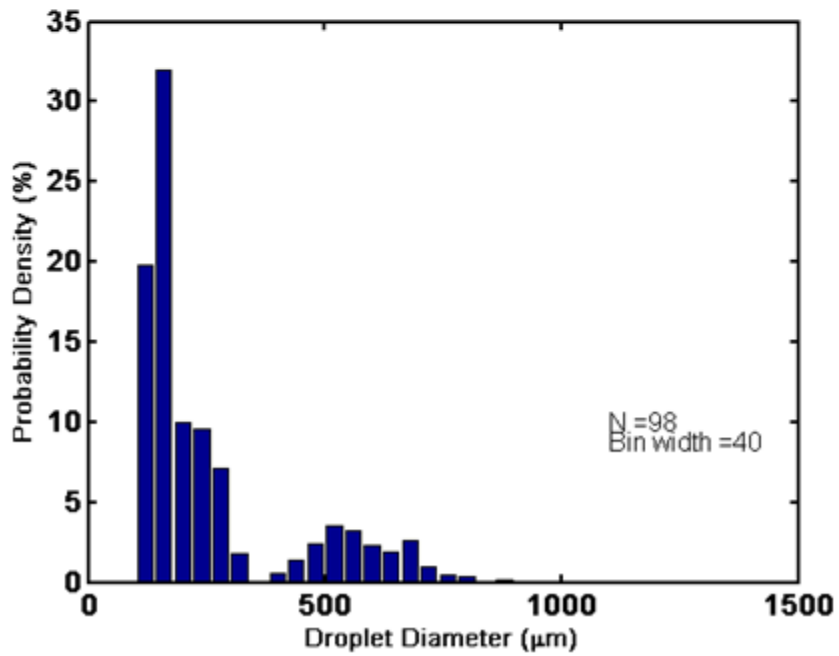
(b)

Figure 5.4: (a) Directly measured and (b) Depth of field corrected drop distribution for clean water and Case 4 corresponding to bubble diameter of 3.210 mm. Bimodal peaks observed at

$120\mu\text{m}$ and $480\mu\text{m}$



(a)



(b)

Figure 5.5: (a) Directly measured and (b) Depth of field corrected drop distribution for clean water Case 5 corresponding to bubble diameter of 3.301 mm. Bimodal peak observed at 120 μm and somewhat diminished peak 520 μm

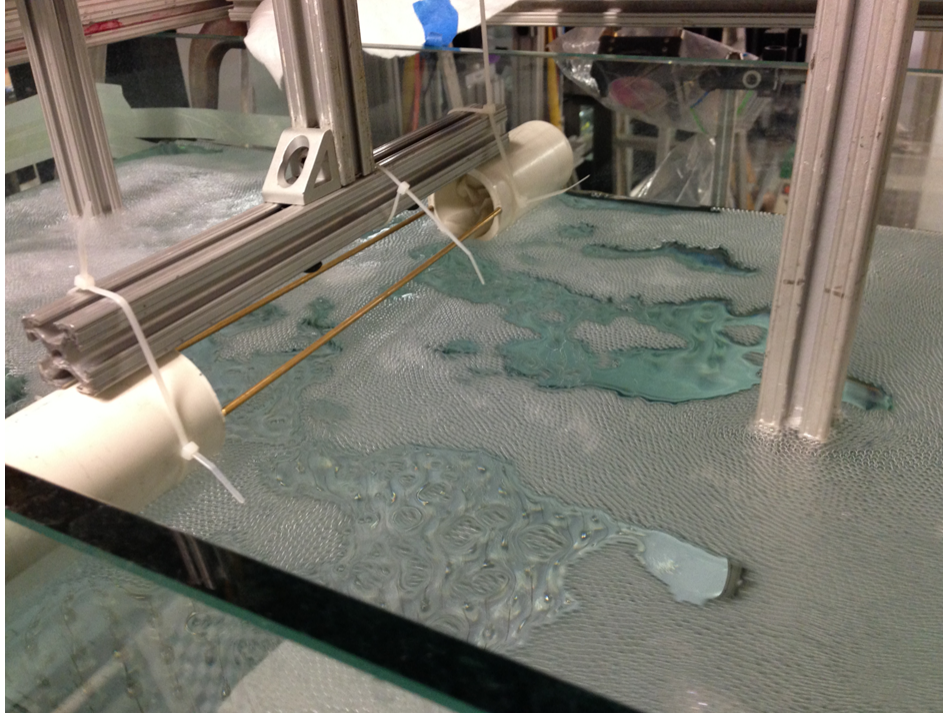


Figure 5.6: Bubble rafts for surfactant condition

constant peak in the $480 - 560 \mu\text{m}$ range for all bubble production rates. The second peak represents a diameter range of $120 - 160 \mu\text{m}$ (Figure 5.1(b) to Figure 5.5(b)). It is clear that the clean water drops are affected by the bubble size and the bubble production rate. Looking at the corrected data in these plots for clean water, it appears that the probability density function for this peak remains at 21% for Case 1¹ and Case 2 and increases to 32% for Case 5. This indicates that there could be potentially a lot more drops in the sub- $100 \mu\text{m}$ range if the bubble diameter increases past the $3000 \mu\text{m}$. This remains yet to be investigated as current study is limited to the $100 \mu\text{m}$ diameter with a known error of less than 7%. The cause of the bimodality maybe embedded in the mode of drop production as to whether the drop is a jet drop or a film drop. Figure 5.12 shows the bimodality of the spectral peaks for a given bubble diameter. The smallest drop observed drop diameter for clean water condition is $81.13 \mu\text{m}$ and the largest is $1308.83 \mu\text{m}$.

¹Refer Table 4.3 for definition of Cases.

The bubble diameter for surfactant solution is in the range of $2369 - 3014 \mu\text{m}$ (Table.4.1). For the surfactant case, many more drops are observed. Figure 5.6 shows accumulation of bubbles at the free surface for the surfactant water condition. The bubbles appear to be more uniform in size accumulating and creating rafts that travel and burst. These accumulating, bursting bubble rafts create the possibility of observing a lot more drops in fewer runs as compared to the clean water condition. The data presented in Figure 5.7 to Figure 5.11 is obtained from five runs for each bubble production rate. Unlike, the clean water, the surfactant solution data doesn't show any apparent distinct bimodality in the raw data. Since the data looks evenly distributed, it seems reasonable to conclude that there is one dominant peak with gradual decrease on either side. Going from Case 1 to Case 2 for surfactant solution, the peak remains constant $240 \mu\text{m}$ size range. According, to *Spiel* [19], no film drops are observed for bubbles less than $2400 \mu\text{m}$ in diameter in seawater. If that is holds true for the surfactant case investigated in this thesis, all the drops observed in Figure 5.7 for 1 inch of air in the bubble-maker may be considered as jet drops. For 2 to 3 inches of air in the bubble-maker, the drop distribution peaks at $120 \mu\text{m}$. In Figure 5.10(a), we observe in the raw data, population of the sub- $100 \mu\text{m}$ drops for Case 3 corresponding to a bubble diameter of 2.879 mm (Tab.4.1). *Spiel's* observations were similar for seawater and data shown in Figure 2.5 indicates a dense population of sub- $100 \mu\text{m}$ film drops corresponding to a comparable bubble diameter of 2.94 mm . However, more investigation is needed to check for similarities if any in drop production between the seawater and surfactant solution. For Case 5, which corresponds to a bubble diameter of 3.014 mm , the distribution in the raw data peaks at $360 - 480 \mu\text{m}$ and drops smaller than $100 \mu\text{m}$ can also be seen in Figure 5.11(a). The raw data for this case looks more like a normal distribution. Figure 5.13 shows the spectral peak drop

diameter versus the bubble diameter. The data suggests that for the investigated bubble sizes and bubble production rates going from Case 1 to Case 5 seems to have little effect on the size of the drops produced for surfactant solution. Perhaps a larger variation in bubble sizes might highlight the surfactant effects more. The smallest observed drop diameter for surfactant condition is $38.26 \mu\text{m}$ which is seen in the case where the bubble production rate corresponds to Case 4. The largest observed drop is $740.71 \mu\text{m}$ in diameter.

In each of the probability density function plots, the number of drops measured (N) in the data set and the bin width used in the histograms is reported. The number of bins is initially estimated using Sturge's formula. After a few trials, a bin width of $40 \mu\text{m}$ is found to represent the data well. It can be noticed that in Figure 5.9(a) $N = 283$ while in Figure 5.9(b) which represents the same data after volume correction has $N = 282$. This is because the sub- $100 \mu\text{m}$ drops are removed from the corrected data data-set as the DOF for that drop diameter has not been calibrated to 7% error. This maybe improved upon in the future.

Figure 5.14 and Figure 5.15 show the the Sauter mean diameters versus the bubble size for the different cases studied. Sauter mean diameter (d_{32}) is defined as the diameter of the drop whose ratio of volume to surface area is same as that of the entire spray. It is given by:

$$d_{32} = \frac{\sum N_i D_i^3}{\sum N_i D_i^2} \quad (5.1)$$

i : Size range considered N_i : Number of drops in the size range i

D_i : Middle diameter in the size range i

From the water conditions studied, it can be inferred that the distribution of drop due to bursting bubbles depends to on the surface tension of the water, bubble size and bubble production rate.

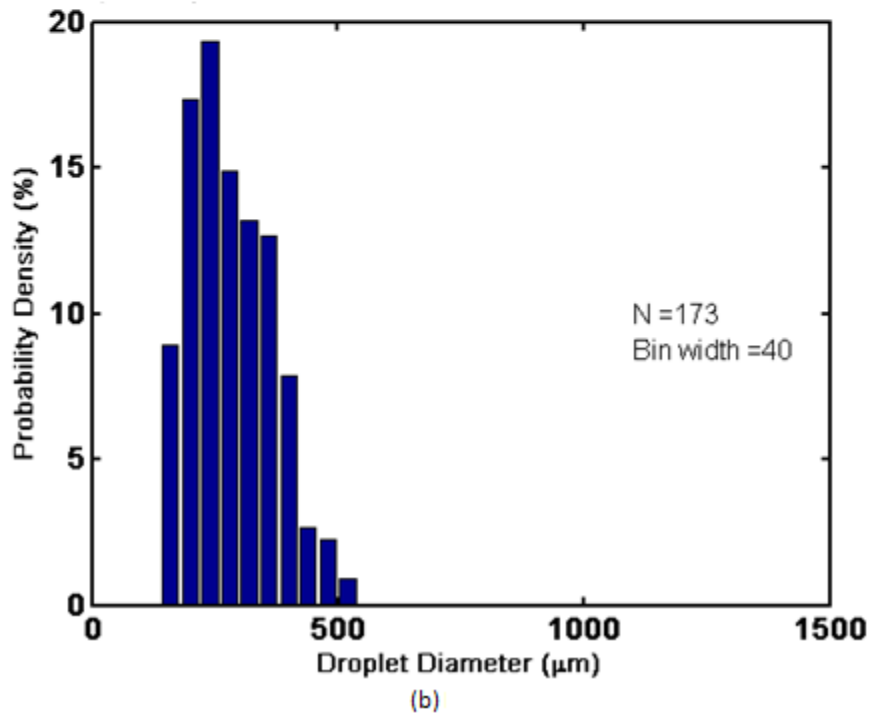
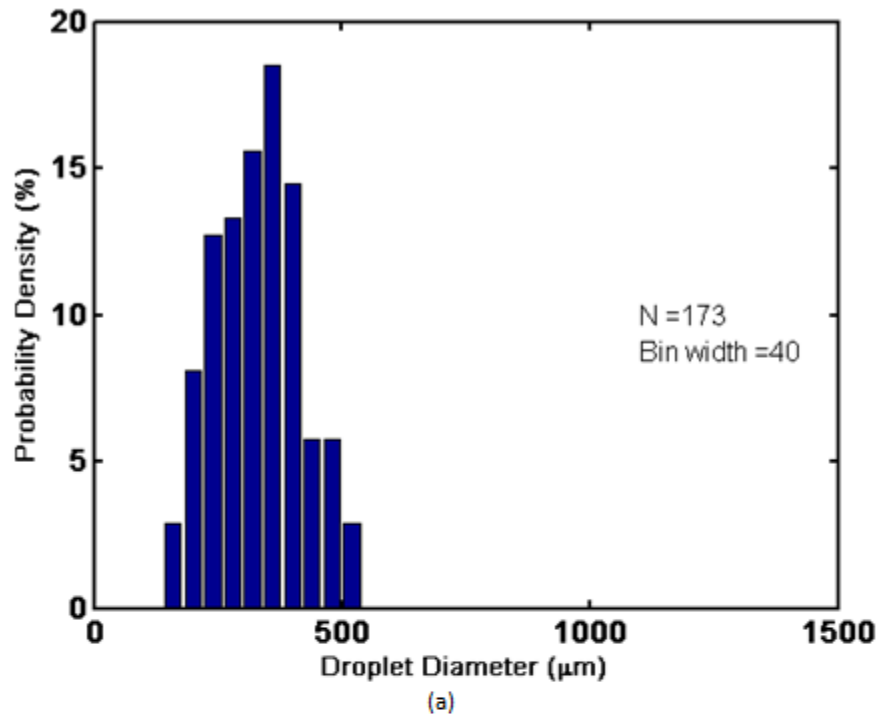


Figure 5.7: (a) Directly measured and (b) Depth of field corrected drop distribution for surfactant solution Case 1 corresponding to bubble diameter of 2.369 mm. Peak observed at

240 μ m

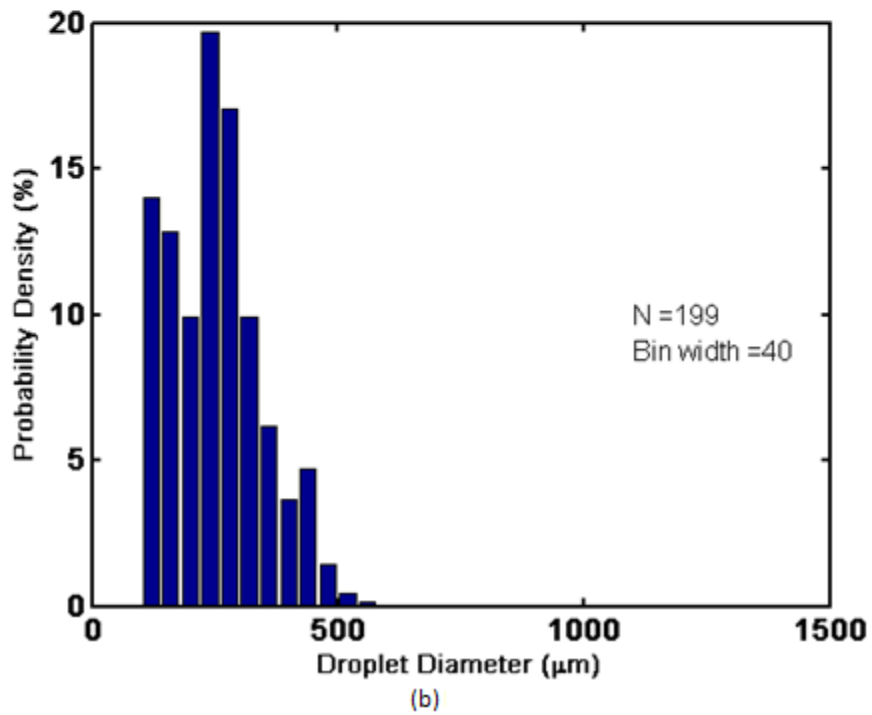
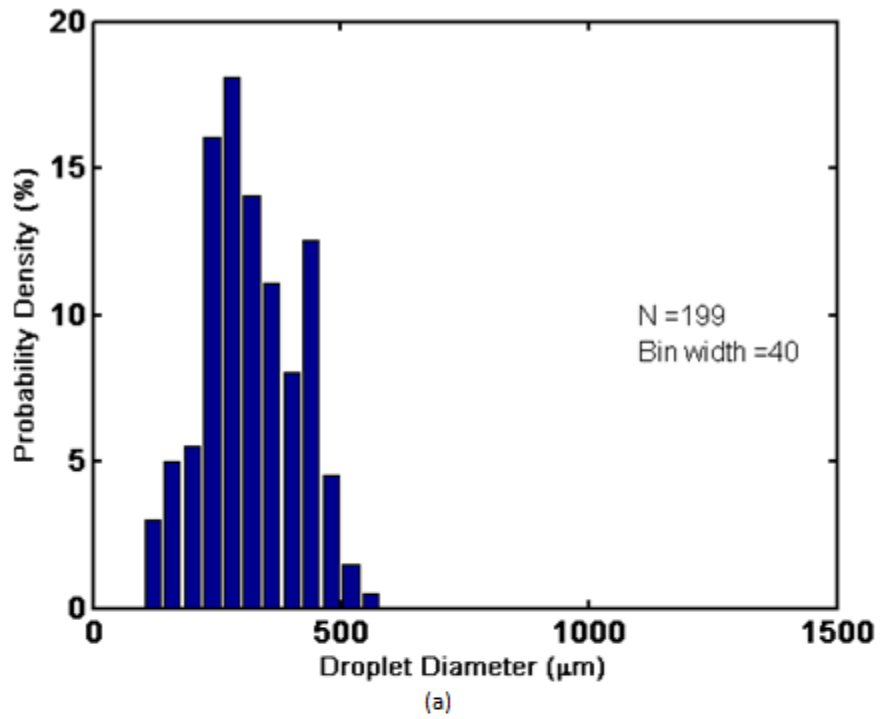


Figure 5.8: (a) Directly measured droplets and (b) Depth of field corrected drop distribution for surfactant solution Case 2 corresponding to bubble diameter of 2.706 mm. Peak observed at

240 μ m

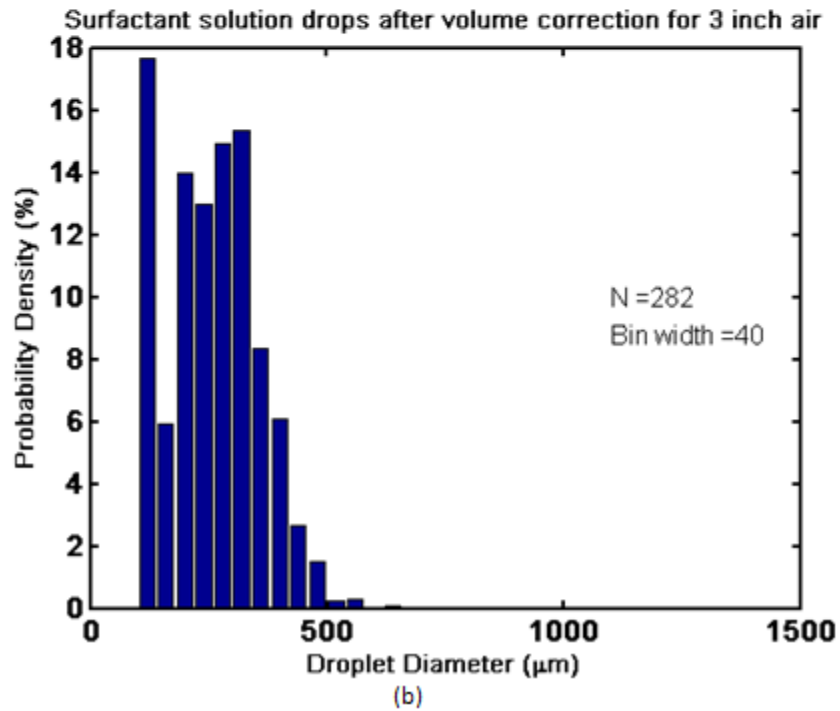
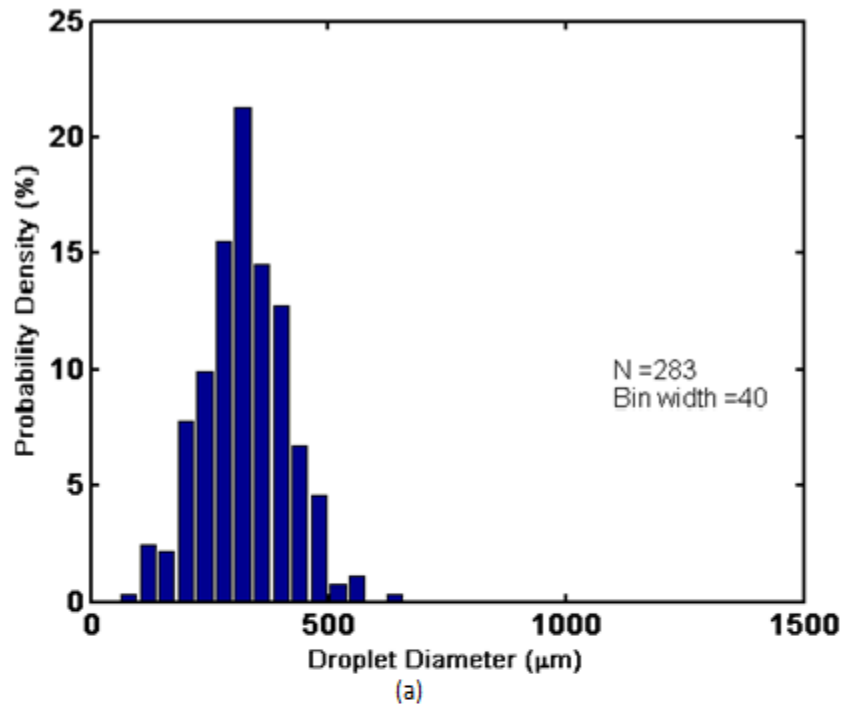
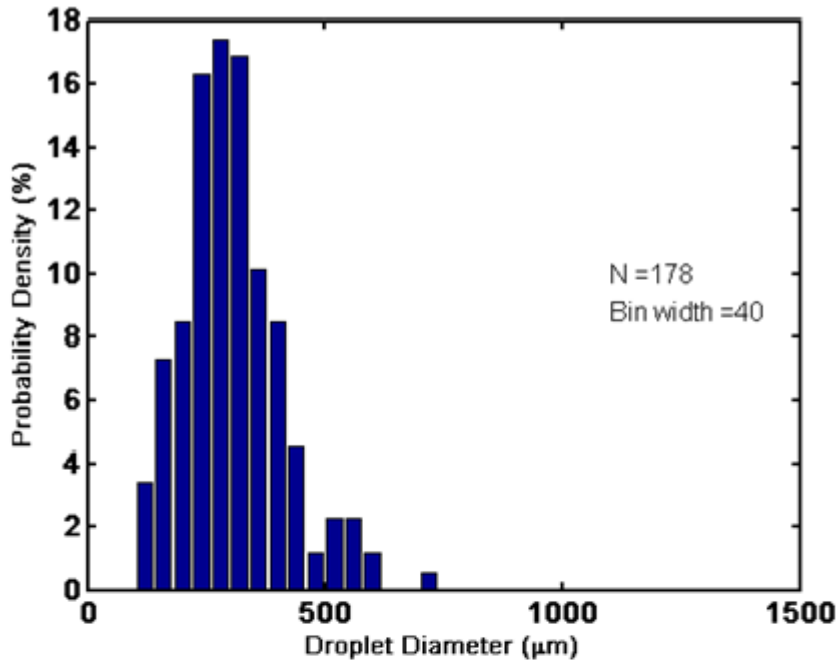
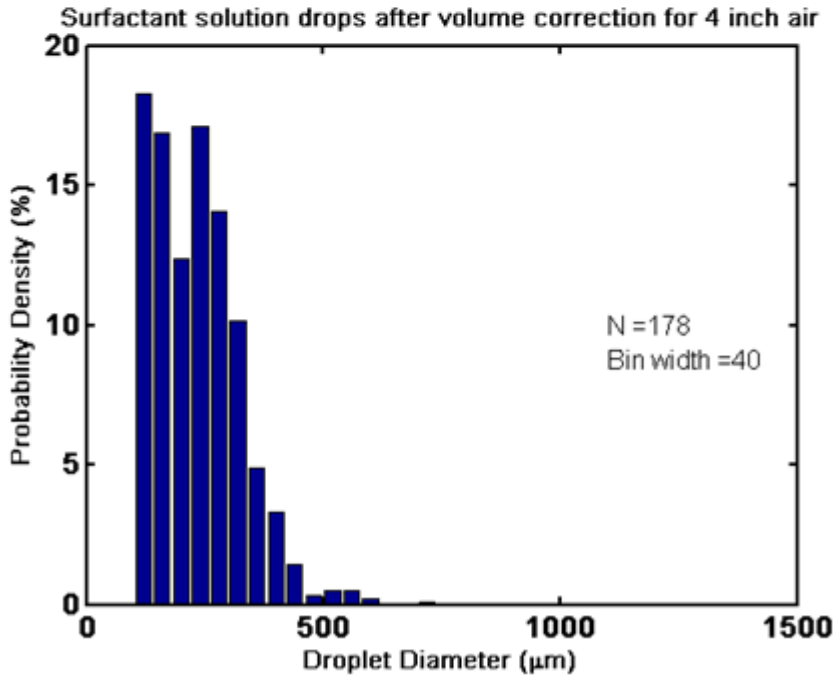


Figure 5.9: (a) Directly measured and (b) Depth of field corrected drop distribution for surfactant solution Case 3 corresponding to bubble diameter of 2.879 mm. Peak observed at

120 μ m



(a)



(b)

Figure 5.10: (a) Directly measured and (b) Depth of field corrected drop distribution for surfactant solution Case 4 corresponding to bubble diameter of 2.676 mm. Peak observed at

120 μm

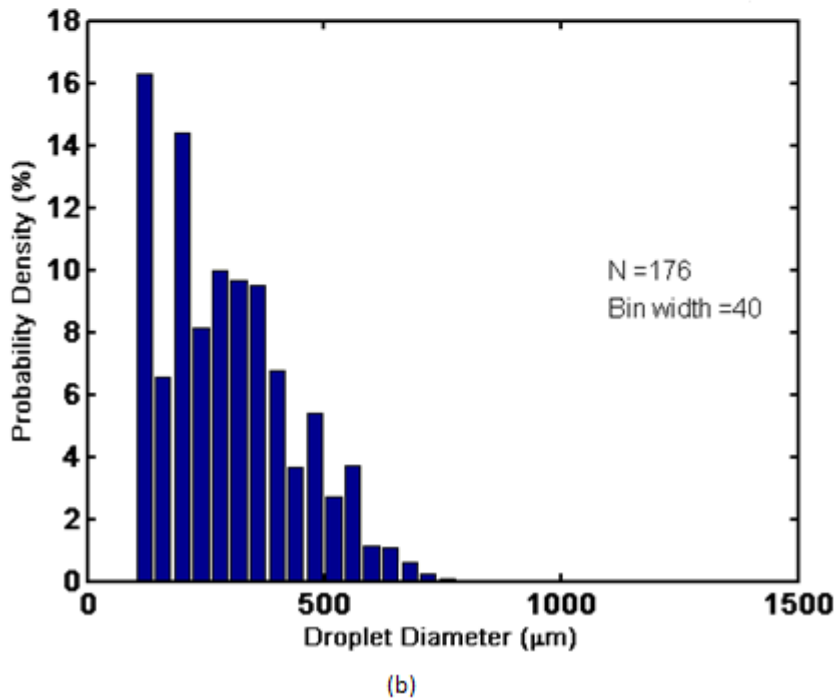
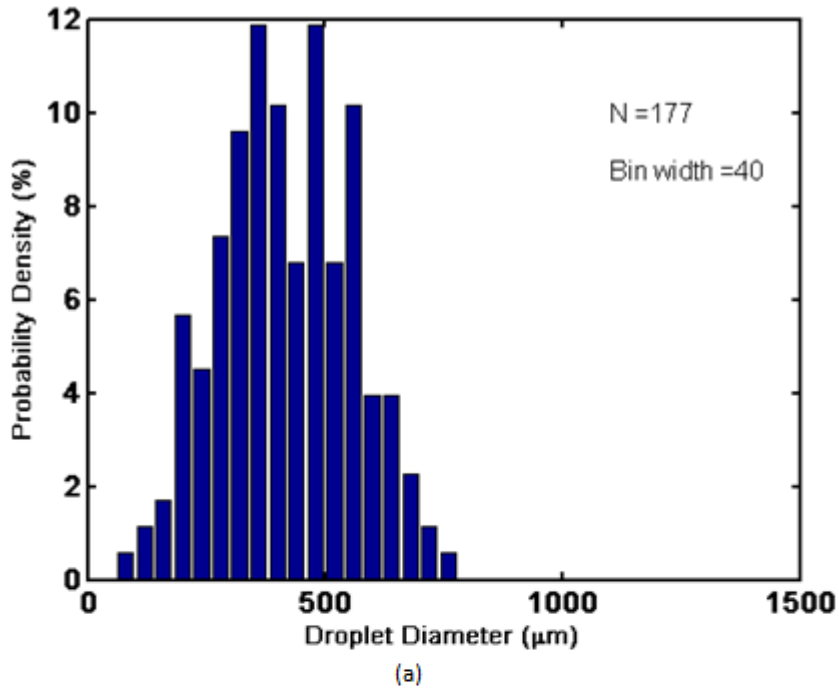


Figure 5.11: (a) Directly measured and (b) Depth of field corrected drop distribution for surfactant solution Case 5 corresponding to bubble diameter of 3.014 mm. Peak observed at

200 μm

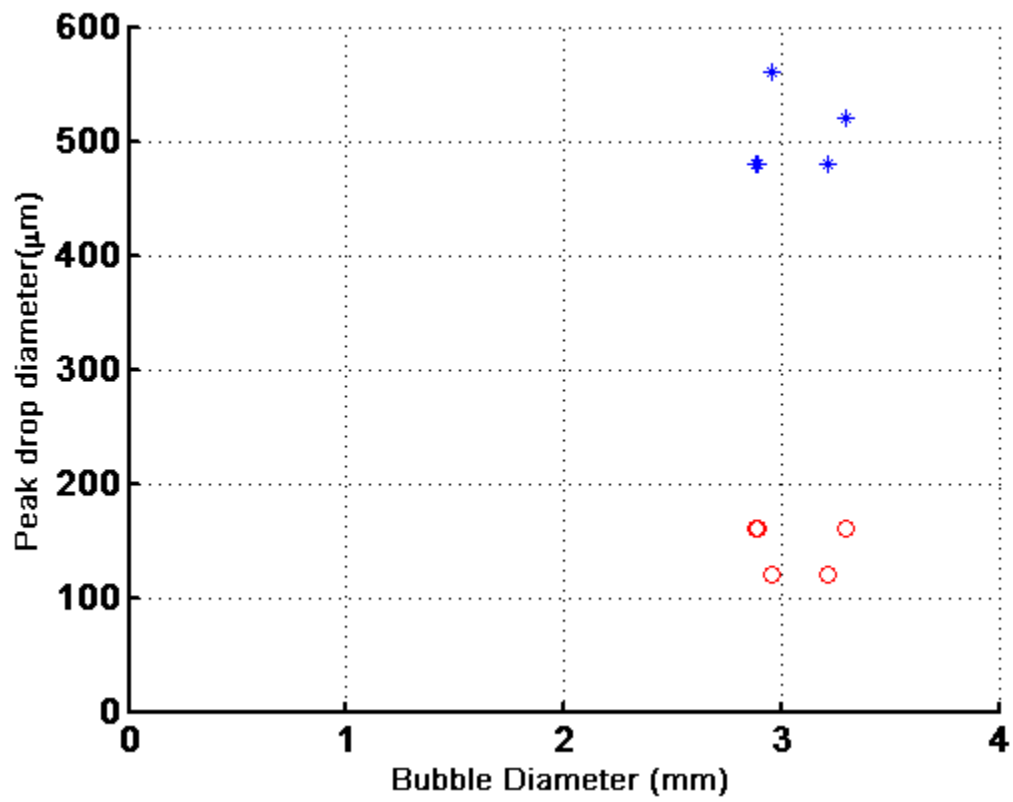


Figure 5.12: Spectral peaks versus bubble diameter for clean water cases: Two different bimodal peaks are represented by asterisks and circles.

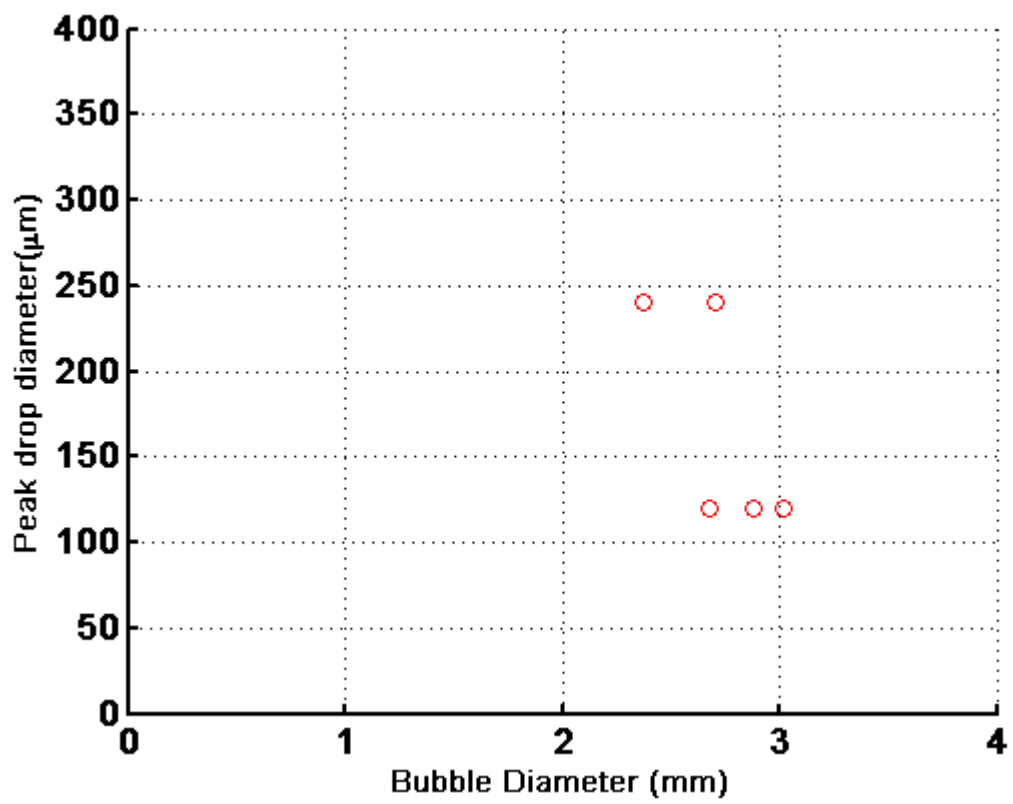


Figure 5.13: Spectral peaks versus bubble diameter for surfactant solution cases

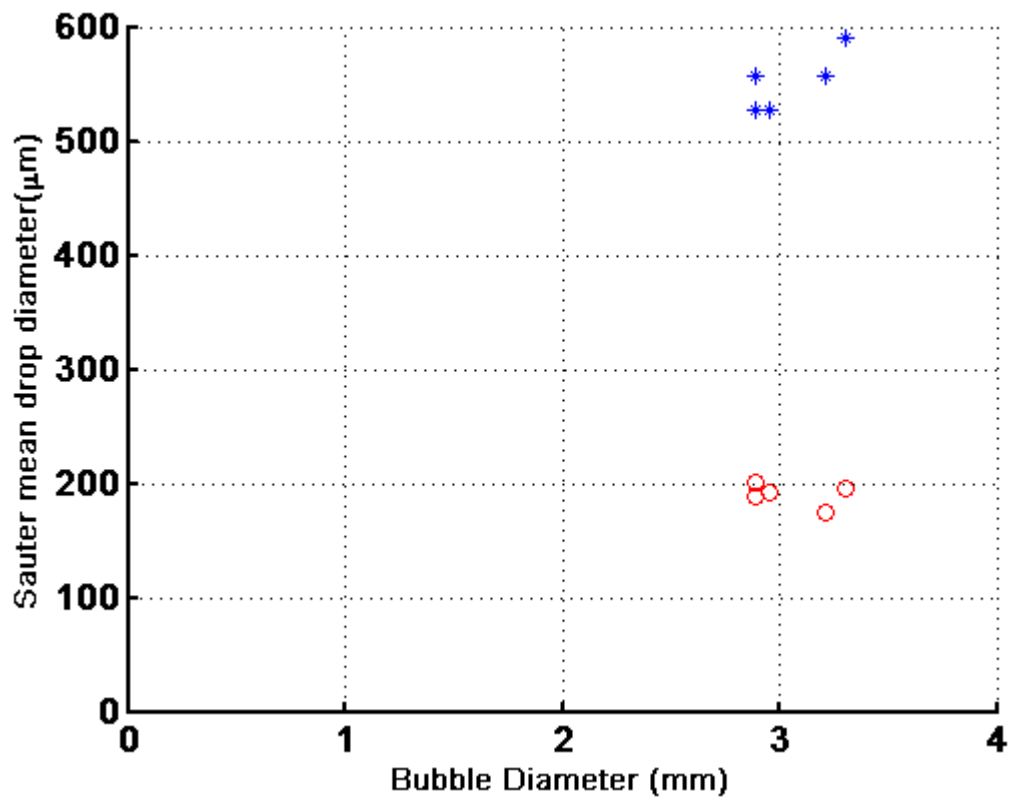


Figure 5.14: Sauter mean drop diameter versus bubble diameter for clean water cases: Two different bimodal Sauter mean drop diameter are represented by asterisks and circles.

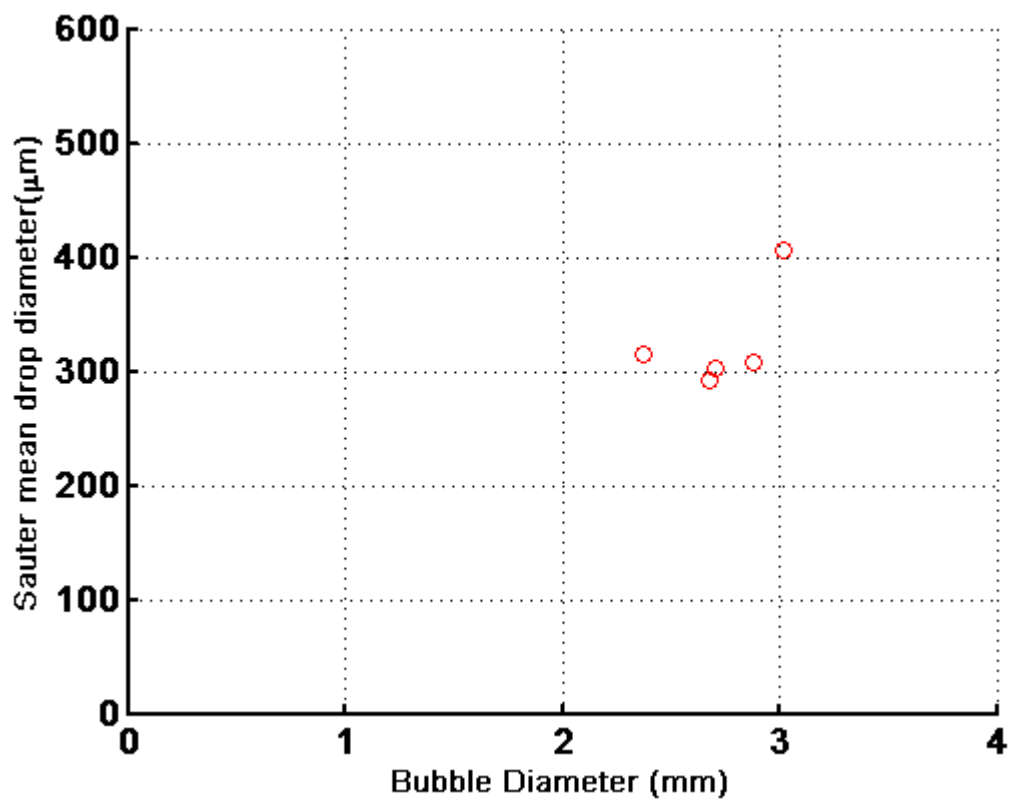


Figure 5.15: Sauter mean drop diameter versus bubble diameter for surfactant solution cases

It must be noted that, peak diameters that are reported in this thesis are the *observable* peaks. If there are peaks due to drops below a 100 μm in diameter, which is strongly suspected then they won't be visible in this data-set. From literature [19], it has been suggested that there is a population of film drops is in the range of 10 μm to 150 μm for our investigated bubble diameter range. In this study for the clean water cases, the bimodality that is observed may stem from the fact that, both jet and film drops are measured together and the peaks possibly represent the two different generation mechanisms. Another reason might be the inherent bimodality reported in the literature for jet drops with spectral peaks at 40 μm and 200 μm [21] from bursting bubbles around 3000 μm in diameter. For the surfactant case in this study, the bimodality is not observed. However, careful assessments must be made before concluding that the surfactant case has no bimodality. It is possible that, bimodal peak for the surfactant case may have been shifted below 100 μm and is not observable in our data-set. It is also possible that the peaks over-lap. To investigate if this is true, a much larger data-set is desirable i.e. more drops. This may help to identify, closely spaced bimodal peaks that may be obscured by the presence of spectral noise created by the present small data set. Perhaps, a segregation between jet and film drops might be useful in confirming a single peak for a given mode of drop generation. This could be possible if the field of view of the cinematic shadowgraph system is moved closer to the free surface of the water to detect the onset of bubble bursting and measure the subsequent film and jet drop production.

Chapter 6

Conclusion and Future work

In this thesis, the effects of surfactants on drop production by bubbles rising to a free surface and bursting was studied experimentally using a cinematic shadowgraph technique. The technique uses a high speed camera and a Nd:YLF laser. A detailed explanation of the experimental setup and the instrument calibration was provided. The technique allowed to measure droplets as small as $100\ \mu\text{m}$ to within 7% error. Drops between $50\ \mu\text{m}$ and $100\ \mu\text{m}$ are also noted but with an error larger than 7%. The experiments were conducted for two water conditions, clean and water laden with a 0.4% v/v solution of Triton X-100 surfactant. Five different bubble diameters and bubble production rates were studied for each water condition. This experiment differs from others because air bubbles are produced continuously with an array of hypodermic needles arranged in a specific orientation allowing bubbles to interact and create random popping events on a non-quiet free surface much like the real world. The bubbles rising to the free surface are oblate spheroids and estimates of the bubble diameter just below the free surface are provided. Raw data for the drop distribution and data calibrated to a fixed measurement volume was provided. Data-set presented comprised of a total of 1436 drops, processed using a custom built MATLAB code which calculates drop diameter using an axisymmetric two-dimensional hyperbolic tangent function fit. It was noticed that the clean water bubbles produced drops in two distinct diameter ranges exhibiting bimodality whereas the surfactant laden water, bubbles produce a more normal sort of drop distribution. For the surfactant water condition, bubble rafts were observed at the free surface. These rafts

add a new dynamic in the drop size produced. In summary, the drop distribution for clean and surfatant water are different, which emphasizes the role surface tension plays in the jet and film drop production from bursting bubbles. The intermingling of bubbles on the non-quiescent free surface plays an important role in the drop distribution observed.

This thesis has brought a few more interesting questions about the bubble bursting and drop production processes. Following areas can be considered for future work on this project:

- The surface tension can be lowered further by increasing the concentration of the Triton X-100 surfactant. This should provide more insight on how the bubble rafts affect the drop production.
- The salinity of the water can be changed to collect some data to enhance understanding about marine aerosol production.
- The size of the needles on the bubble-maker can be changed to create different size bubbles. The drop measurement technique can be applied for bubble measurements also and this should provide more accuracy for bubble size measurements.
- The data collected in this thesis can be used to provide measurements of the horizontal and vertical ejection velocities of the drops. A processing routine needs to be developed.
- With a higher than 7% allowable error, the current measurement technique is capable of measuring drops up to 30 μm in diameter which are 3 pixels in size. Another technique for data processing is discussed in [24], which could help in reducing error for sub-100 μm drops.

- To find the sub-30 μm drops, a Phase Doppler Particle Analyzer (PDPA) may be employed.
- A distinction between jet and film drops can be useful in understanding the overall drop distribution.

Appendix A

Estimation of bubble size for Case 5 with clean water

The data for bubble diameter measurement for clean water Case 5 with 5 inches of air in the bubble-maker was not readable due to a bad sector on the hard drive on which it was stored. After unsuccessful attempts to recover the data, it was decided to estimate the bubble size for this particular case by fitting a second degree polynomial curve to the data of bubble production rate versus bubble diameter for clean water case and then extrapolating the diameter required for the known bubble production rate.

In Figure [A.1](#), we can see the fit to the data for the production rate from a single needle versus bubble diameter. The goodness of fit for the curve is $R^2 = 0.9708$. A bubble diameter of 3.301 mm corresponding to a single needle flow rate of 42 bubbles/second is estimated for the clean water Case 5. The diameter obtained is larger than the comparable Case 5 of the surfactant solution (3.014 mm), which is consistent with the observations for this data-set.

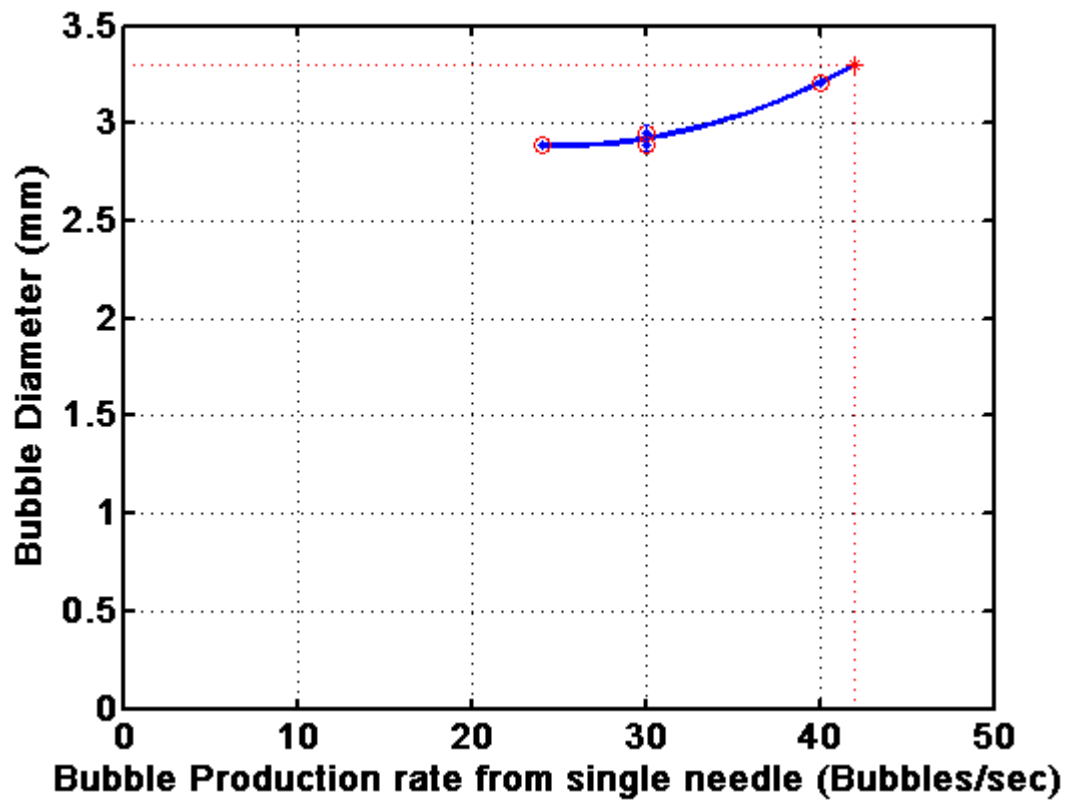


Figure A.1: Bubble production rate versus bubble diameter for clean water Case 5 with 5 inches of air in the bubble-maker. The data points are represented by red circles and the extrapolated value is indicated by red asterisk.

Bibliography

- [1] D. Blanchard. *The electrification of the atmosphere by particles from bubbles in the sea*. PhD thesis, Woods Hole Oceanographic Institution., 1963.
- [2] Duncan C. Blanchard. Surface-active monolayers, bubbles and jet drops. *Tellus*, 42B:200–205, 1990.
- [3] D. C. Blanchard. The size and height to which jet drops are ejected from bursting bubbles in sea water. *J. Geophys. Res.*, 94:10,999–11,002, 1989.
- [4] L. D. Blanchard, D. C. & Sysdek. Film drop production as a function of bubble size. *J. Geophys. Res.*, 93 (C4):3649–3654, 1988.
- [5] Duncan C. Blanchard and Lawrence D. Syzdek. Water-to-air transfer and enrichment of bacteria in drops from bursting bubbles. *Appl. Environ. Microbiol.*, 43(5):1001–1005, 1982.
- [6] Duncan C. Blanchard and Lawrence D. Syzdek. Seven problems in bubble and jet drop research. *Limnol. Oceanogr*, 23,(3):389–400, 1978.
- [7] D. C. Blanchard and A. H. Woodcock. Bubble formation and modification in the sea and its meteorological significance. *Tellus, A quarterly Journal of Geophysics*, 9(2), 1957.
- [8] Scott R Burger and Duncan C. Blanchard. The persistence of air bubbles at a seawater surface. *J. Geophys. Res.*, 88:7724–7726, 1983.
- [9] J. M. Boulton-Stone A.N. Emery Dey, D and J.R. Blake. Experimental comparisons with a numerical model of surfactant effects on the burst of a single bubble. *Chemical Engineering Science*, 52:2769–2783, 1997.
- [10] Stéphane Popinet Christophe Josserand Duchemin, L and Stéphane Zaleski. Jet formation in bubbles bursting at a free surface. *Phys. Fluids*, 14(9):3000, 2002.
- [11] W. C. Jacobs. Preliminary reports on the study of atmospheric chlorides. *Mon. Weath. Rev.*, 65:147–151, 1937.
- [12] Arons A. B Blanchard D. C. Woodcock A. H. Kientzler, C. F. Photographic investigation of the projection of droplets by bubbles bursting at a water surface. *Tellus*, 6:1–7, 1954.
- [13] Dombrowski N. & Newitt D. M. Knelman, F. H. Mechanism of the bursting of bubbles. *Nature*, 173:261, 1954.
- [14] E. Lhuissier, H. and Villermaux. Bursting bubble aerosols. *J. Fluid Mech.*, 696:5–44, 2011.

- [15] Xinan Liu. *An experimental investigation of effects of surfactants on spilling breakers*. PhD thesis, University of Maryland, College Park, 2002.
- [16] G. Resch, F. & Afeti. Film drop distribution from bubbles bursting in seawater. *J. Geophys. Res.*, 96 (C6):10681–10688, 1991.
- [17] Francois Resch and George Afeti. Submicron film drop production by bubbles in seawater. *J. Geophys. Res.*, 97:3679–3683, 1992.
- [18] Darrozes J.S Aféti G.M. Resch, F.J. Marine liquid aerosol production from bursting of air bubbles. *J. Geophys. Res.*, 91:1019–1029, 1986.
- [19] D. E. Spiel. On the births of film drops from bubbles bursting on seawater surfaces. *Journal of Geophysical Research*, 103:24,907–24,918, 1998.
- [20] Donald E. Spiel. A hypothesis concerning the peak in film drop production as a function of bubble size. *J. Geophys. Res.*, 102:1153–1161, 1997.
- [21] D. E. Spiel. The sizes of jet drops produced by air bubbles bursting on sea- and fresh-water surfaces. *Tellus*, 46B:325–338, 1994.
- [22] M. Struthwolf and D. C. Blanchard. The residence time of air bubbles 400m diameter at the surface of distilled water and seawater. *Tellus*, 36B:294–299, 1984.
- [23] Mohammadreza Tavakolinejad. *Air Bubble Entrainment by Breaking Bow Waves Simulated by a 2D+T Technique*. PhD thesis, University of Maryland, College Park, 2010.
- [24] Dan (Sophie) Wang. Laboratory measurements of spray droplets generated by breaking water waves. Master’s thesis, University of Maryland, College Park, 2012.